

AFAL-TR-88-038

AD:



Final Report
for the period
August 1985 to
March 1988

RCS/Piezoelectric Distributed Actuator Study

August 1988

Authors:
T. Bailey
A. Gruzen
P. Madden

The Charles Stark Draper Laboratory, Inc.
555 Technology Square
Cambridge, MA 02139

AD-A201 276

CSDL-R-2076
F04611-85-K-0050

Approved for Public Release

Distribution is unlimited. The AFAL Technical Services Office has reviewed this report, and it is releasable to the National Technical Information Service, where it will be available to the general public, including foreign nationals.

S DTIC
ELECTE **D**
DEC 06 1988
CE

Prepared for the:

**Air Force
Astronautics
Laboratory**

Air Force Space Technology Center
Space Division, Air Force Systems Command
Edwards Air Force Base,
California 93523-5000

NOTICE

When U.S. Government drawings, specifications, or other data are used for any purpose other than a definitely related Government procurement operation, the fact that the Government may have formulated, furnished, or in any way supplied the said drawings, specifications, or other data, is not to be regarded by implication or otherwise, or in any way licensing the holder or any other person or corporation, or conveying any rights or permission to manufacture, use, or sell any patented invention that may be related thereto.

FOREWORD

This final report was submitted by The Charles Stark Draper Laboratory, Cambridge, MA on completion of contract F04611-85-K-0050 with the Air Force Astronautics Laboratory (AFAL), Edwards Air Force Base, CA. AFAL Project Manager was Lt Tim Strange.

This report has been reviewed and is approved for release and distribution in accordance with the distribution statement on the cover and on the DD Form 1473.


TIMOTHY J. STRANGE, III, ILT, USAF
Project Manager


L. KEVIN SLIMAK
Chief, Interdisciplinary Space
Technology Branch

FOR THE COMMANDER

DAVID J. OLKOWSKI, Major, USAF
Deputy Director
Aerospace Vehicle Systems Division

REPORT DOCUMENTATION PAGE

1a REPORT SECURITY CLASSIFICATION UNCLASSIFIED		1b RESTRICTIVE MARKINGS	
2a SECURITY CLASSIFICATION AUTHORITY		3 DISTRIBUTION/AVAILABILITY OF REPORT Approved for public release; distribution is unlimited.	
2b DECLASSIFICATION/DOWNGRADING SCHEDULE			
4 PERFORMING ORGANIZATION REPORT NUMBER(S) CSDL-R-2076		5 MONITORING ORGANIZATION REPORT NUMBER(S) AFAL-TR-88-038	
6a NAME OF PERFORMING ORGANIZATION The Charles Stark Draper Laboratory, Inc.	6b OFFICE SYMBOL (If applicable) 51993	7a NAME OF MONITORING ORGANIZATION Air Force Astronautics Laboratory	
6c ADDRESS (City, State, and ZIP Code) 555 Technology Square Cambridge, MA 02139		7b ADDRESS (City, State, and ZIP Code) AFAL/VSSS Edwards AFB, CA 93523-5000	
8a NAME OF FUNDING/SPONSORING ORGANIZATION	8b OFFICE SYMBOL (If applicable)	9. PROCUREMENT INSTRUMENT IDENTIFICATION NUMBER F04611-85-K-0050	
8c ADDRESS (City, State, and ZIP Code)		10. SOURCE OF FUNDING NUMBERS	
		PROGRAM ELEMENT NO. 61101F	PROJECT NO. 2864
		TASK NO. 00	WORK UNIT ACCESSION NO. AK
11 TITLE (Include Security Classification) RCS/Piezoelectric Distributed Actuator Study (U)			
12 PERSONAL AUTHOR(S) Thomas Bailey, Alexander Gruzen, Paul Madden			
13a TYPE OF REPORT Final	13b TIME COVERED FROM Aug. 85 to Mar 88	14. DATE OF REPORT (Year, Month, Day) 88/8	15. PAGE COUNT 114
16 SUPPLEMENTARY NOTATION			
17. COSATI CODES		18 SUBJECT TERMS (Continue on reverse if necessary and identify by block number)	
FIELD	GROUP	SUB-GROUP	
22	02		Piezoelectric distributed actuators
22	01		Flexible structure vibration control
			Low-authority actuators
19 ABSTRACT (Continue on reverse if necessary and identify by block number) The objective of the program was to develop the technology of piezoelectric distributed actuators, and to test the effectiveness and performance of the actuators when used to augment the damping of a simulated large flexible space structure. The CSDL/AFAL experimental test facility located at CSDL, Inc. was used to test and demonstrate the technology.			
20 DISTRIBUTION/AVAILABILITY OF ABSTRACT <input checked="" type="checkbox"/> UNCLASSIFIED/UNLIMITED <input type="checkbox"/> SAME AS RPT <input type="checkbox"/> DTIC USERS		21 ABSTRACT SECURITY CLASSIFICATION UNCLASSIFIED	
22a NAME OF RESPONSIBLE INDIVIDUAL Timothy J. Strange, 1Lt, USAF		22b TELEPHONE (Include Area Code) (805) 275-5147	22c OFFICE SYMBOL VSSS

TABLE OF CONTENTS

Section	Page	
1	Introduction and Summary	1
1.1	Background	1
1.1.1	The Large Space Structure (LSS) Problem	1
1.1.2	Motivation for the Piezoelectric Distributed Actuator Study	1
1.2	Organization of the Report	2
1.2.1	Report Overview	2
1.3	Summary of the Results	4
1.3.1	Scaled Experiments and Theory	4
1.3.2	Full-Scale Experiment Verification Study	7
1.4	Conclusions	9
1.4.1	Value of Small-scale Tests	9
1.4.2	Performance of the PVF ₂ Actuators	9
1.4.3	General Observations about Low Authority Actuators	10
2	Distributed Active Damper Design using PVF₂	11
2.1	Damping of Distributed Space Structures	11
2.2	Lyapunov Damper Development	12
2.3	Experimental Verification of Lyapunov Control	14
2.3.1	Test Structures	14
2.3.2	Scaled Steel Cantilever Beam Results	16
2.3.3	AFAL Experiment Cantilever Beam Results	16
2.3.4	Higher Mode Results	19
2.4	Discussion of Lyapunov Control Effectiveness	22
3	Active Constrained Layer Damper Design	27
3.1	Constrained Layer Dampers	27
3.2	Modelling of an Active Constrained Layer Damper	28
3.3	Energy Dissipation with an Active Constrained Layer Damper	33

4	Examination of Active Constrained Layer Damper Effectiveness	39
4.1	Experimental Evaluation of an Active Constrained Layer Damper	39
4.1.1	Material	39
4.1.2	Feedback Control Laws tested	44
4.1.3	Experimental Procedure	44
4.1.4	Experimental Results	45
4.2	Shear Strain in the Viscoelastic Layer	48
5	Derivation of the Control Law for the PVF₂ Film Actuators	55
5.1	Introduction	55
5.2	Hamilton's Principle	55
5.3	Direct Method	64
5.4	Lyapunov Stability Criteria	67
5.4.1	Extension of Analysis to Include All Beams	68
5.5	Constraints Associated with the Use of Angular Accelerometers	72
6	Application of the PVF₂-Film Actuators to the Full-Scale Experiment	73
6.1	Introduction	73
6.2	Background	73
6.3	General Procedure	74
6.3.1	Bonding of the PVF ₂ Film	74
6.3.2	Selection of Adhesive	75
6.3.3	Development and Testing of Application Techniques	76
6.4	Proof Testing of Actuators	77
7	Full-Scale Distributed Parameter Actuator Testing and Results	79
7.1	Summary	79
7.2	Testing methods	79
7.3	Evaluation of Excitation Sources	81
7.4	Test Configuration	82
7.4.1	High Voltage EMI and Safety Concerns	83
7.5	Experimental Results and Analysis	85
8	Summary and Conclusions	91
8.1	Summary of the Results	91
8.1.1	Scaled Experiments and Theory	91
8.1.1.1	Lyapunov Damper	91
8.1.1.2	Active Constrained Layer Damper	93
8.1.2	Full-Scale Experiment Verification Study	94
8.2	Conclusions	96
8.2.1	Value of Small-scale Tests	96

8.2.2	Performance of the PVF ₂ Actuators	96
8.2.3	General Observations Concerning Low Authority Actuators	97
8.3	Recommendations	98
A	Modal Model of the AFAL Structure.	103
B	MicroVAX II Control Computer Configuration	105



Accession For	
NTIS CRA&I	<input checked="" type="checkbox"/>
DTIC TAB	<input type="checkbox"/>
Unannounced	<input type="checkbox"/>
Justification	
By	
Distribution /	
Availability Codes	
Dist	Avail and/or Special
A-1	

LIST OF FIGURES

Figure		Page
1-1	The AFAL experiment structure at the Charles Stark Draper Laboratory.	3
2-1	Lyapunov damper configuration.	12
2-2	Lyapunov damper on a cantilevered beam with mass and rotary inertia at the tip.	13
2-3	Damping results of lyapunov control on first mode of steel beam.	17
2-4	Experimental and simulated decay envelopes for the 6 inch test structure.	18
2-5	Sensor configuration used in aluminum beam tests.	19
2-6	Damping results of lyapunov control on the first mode of the aluminum structure.	20
2-7	Experimental and simulated decay envelopes for the aluminum test structure.	21
2-8	Damping results of lyapunov control on second mode of aluminum beam.	23
2-9	Damping results of lyapunov control on third mode of aluminum beam.	24
3-1	Free layer and constrained layer dampers.	28
3-2	Beam section with constrained layer damper.	29
3-3	Beam element in bending.	30
3-4	Free body diagram of an element of a damped sandwich beam.	31
3-5	Free body diagram of constraining layer of constrained layer damper.	32
3-6	Cantilevered beam with active constrained layer damper.	34
3-7	Hysteresis loop of a viscoelastic material.	34
4-1	Active constrained layer damper test configuration.	40
4-2	Reduced frequency plot of modulus and loss factor for Scotchdamp SJ015X, Type 112.	42

4-3	Schematic of typical active constrained layer damper test article. . .	43
4-4	Real part of transfer function between beam excitation voltage and tip acceleration.	45
4-5	Instrumentation used in constrained layer damper tests.	46
4-6	Typical transfer function between beam excitation voltage and tip acceleration.	47
4-7	Shear stress distribution in the viscoelastic layer of an active constrained layer damper with constraining layer free at both ends.	52
4-8	Shear stress distribution in the viscoelastic layer of an active constrained layer damper with constraining layer clamped at one end.	53
5-1	Cantilever and hub.	56
5-2	Deflection of differential beam element.	59
5-3	Force balance on differential element at point q.	64
5-4	Summing moments about z-axis of hub.	66
5-5	Sign convention of angular rates.	71
7-1	Schematic of the experimental facility configuration used for the PVF ₂ actuator tests.	83
7-2	Transfer function magnitudes using 0.150 (lb-ft) ² excitation.	87
7-3	Transfer function magnitudes using 0.018 (lb-ft) ² excitation.	88
7-4	Transfer function magnitudes using 0.004 (lb-ft) ² excitation.	89
A-1	AFAL structure mode shapes.	104
B-1	MicroVAX II computer system configuration.	106

LIST OF TABLES

Table		Page
2-1	Beams used in Lyapunov damper tests.	15
2-2	PVF ₂ film properties.	15
2-3	Nondimensional parameters.	16
3-1	Final design values of passive constrained layer damper using PVF ₂ as the constraining layer.	35
3-2	Passive constrained layer damper design using a steel constraining layer.	36
4-1	Constrained layer dampers tested on steel structure.	41
4-2	Test article properties used in constrained layer damper tests.	41
4-3	Constrained layer damper test results, uncontrolled.	48
4-4	Constrained layer damper test results, po- sition feedback, 350 V p-p.	49
4-5	Constrained layer damper test results, ve- locity feedback, 350 V p-p.	49
4-6	Constrained layer damper test results, switching control, 350 V p-p.	49
4-7	Constrained layer damper test results, ve- locity feedback, 500 V p-p.	50
4-8	Constrained layer damper test results, switching control, 500 V p-p.	50
4-9	Constrained layer damper test results, po- sition feedback, 700 V p-p.	50
4-10	Simulation parameters used in shear stress analysis for pinned- pinned beam.	51
7-1	PVF ₂ distributed actuator damping results.	86
A-1	Vibrational mode frequencies with PMAs locked.	103

Section 1

Introduction and Summary

1.1 Background

The RCS/Piezoelectric Distributed Actuator project was initiated by the U.S. Air Force Astronautics Laboratory (AFAL) in 1985 to develop the technology of piezoelectric distributed actuators and to demonstrate the use of this technology for structural damping augmentation. The demonstration utilizes both small-scale experiment specimens and the full-scale experimental test facility which was developed to test actuator concepts and control laws for the integrated control of simulated large space structures.

1.1.1 The Large Space Structure (LSS) Problem

Large space structures encompass systems which range in size from tens of meters to several hundred meters. These lightweight, flexible structures are often constructed of aluminum or composite materials which have low inherent natural damping. The low damping and high flexibility make the structures susceptible to environmental disturbances. In some cases, passive damping mechanisms may be sufficient to satisfy vibration suppression requirements. However, in other situations the specifications on pointing accuracy, or other criteria may be sufficiently stringent to require either additional stiffness or damping, or both. Active control will be necessary to satisfy these requirements. These systems are of particular interest to control system engineers when the structural vibration modal frequencies are close to, or overlap, the desired control system bandwidth.

1.1.2 Motivation for the Piezoelectric Distributed Actuator Study

The research reported here concerns, in particular, the AFAL experiment located at the Charles Stark Draper Laboratory Inc. [1]. This structure was designed to display closely spaced, lightly damped modes, which are characteristic of large space structures.

It consists of a cylindrical hub with four perpendicular appendages extending radially outward. (see Figure 1-1) The entire structure is mounted on an air bearing table to allow free rotation about the hub axis. Nitrogen gas thrusters are mounted on two of the arms. These are used to initiate and control slew maneuvers of the structure. Simulation results from the predecessor program [2] demonstrated that significant vibration control improvement could be obtained when a linear actuation device was used in combination with the RCS thrusters. In this operating mode, the thrusters are used primarily for slew control, and the linear actuator is used primarily for vibration control and/or for fine pointing and tracking.

A promising candidate among several possible actuation devices is the distributed piezoelectric-polymer film actuator. Preliminary research into the use of this actuator to augment the damping of a scaled AFAL experiment arm was performed by Bailey and Hubbard [3] under joint CSDL/MIT sponsorship. This effort demonstrated a forty-fold increase in damping for low amplitude vibration levels.

The present study was undertaken to further develop the technology of distributed-parameter actuators in general and PVF₂ film devices in particular. Bonding techniques, modelling and controls analysis and synthesis methods, and novel damper configurations were among the topics to be explored. Experiments and analysis were to be performed on scaled models of the AFAL structure, culminating in the application of a PVF₂ active damper to the full-scale structure.

1.2 Organization of the Report

The report documents the technical accomplishments of the completed twenty-eight-month experimental verification program. The results of the first fourteen months of the program were previously published as an interim report by CSDL, Inc. This report of the completed program incorporates the interim report as Sections 2 through 4. The remainder of the report (Sections 5 through 8) constitutes work performed in the latter half of the program and includes results from the actual tests performed on the full-scale AFAL experiment structure.

A parallel study addressed the related area of space environmental effects on PVF₂ film. A separate report [4] documents the results of this work which was performed during an early phase of the program.

1.2.1 Report Overview

Section 2 presents a review of the damper design developed by Bailey which uses PVF₂ as the actuator and a non-linear switching control algorithm. An experimental verification of this controller for cantilevered beams is also presented. The results are

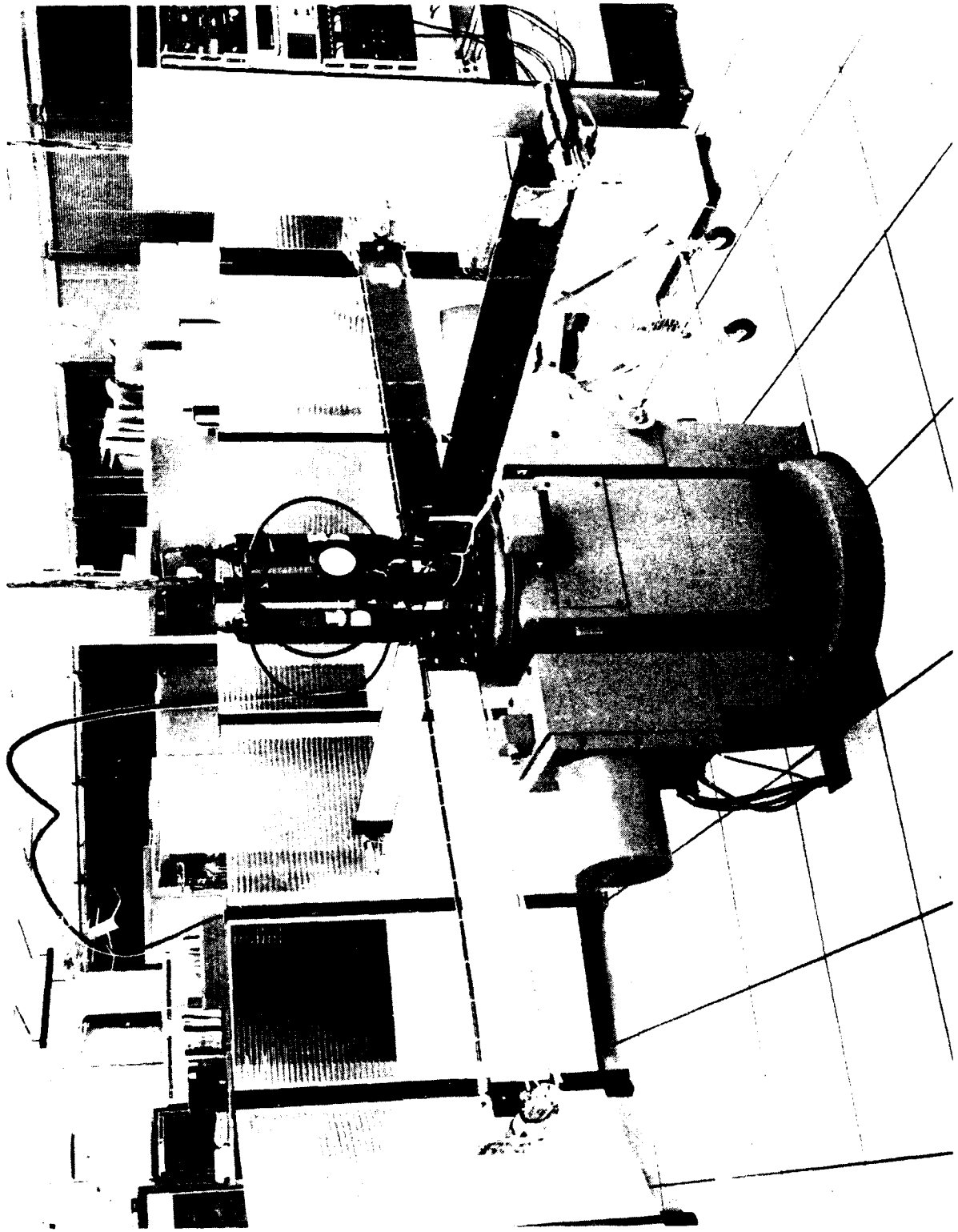


Figure 1-1. The AFAL experiment structure at the Charles Stark Draper Laboratory.

from damping tests on the first cantilever mode of a $0.152 \text{ m} \times 0.0127 \text{ m} \times 3.81 \times 10^{-4} \text{ m}$ (6 inch x 0.50 inch x 0.015 inch) steel beam and the first three cantilever modes of a $1.22 \text{ m} \times 0.152 \text{ m} \times 3.18 \times 10^{-3} \text{ m}$ (48 inch x 6 inch x 0.1250 inch) aluminum beam.

Section 3 presents the modelling and design of an active constrained layer damper which uses PVF₂ film as the constraining layer. This design is presented as a means of extending the range of displacement amplitudes which can be effectively controlled by the damper presented in Section 2. Active boundary work terms as well as active dissipation terms are identified and discussed.

Section 4 presents experimental work done using the active constrained layer damper. Tests were run to evaluate the damper effectiveness, and to compare the effects of several different feedback control laws. The results of a computer analysis of an active constrained layer damper applied to a pinned-pinned beam is also presented.

Section 5 presents the modelling and design of a PVF₂ damper for the full-scale AFAL structure. The PVF₂ control algorithm was derived using Lyapunov's direct method which results in a nonlinear switching control algorithm.

Section 6 describes the techniques developed to bond the PVF₂ film to the arms of the full-scale structure and to insure reliable bonding of the high voltage connector to the outer surface of the PVF₂ film.

Section 7 presents the experimental work performed for the full-scale PVF₂ actuator tests. Two testing methods are discussed, and two sources of excitation to the experimental structure are compared. Bandlimited random-excitation transfer function identification tests were performed using several levels of excitation to evaluate the damper effectiveness at different amplitudes of vibration.

Section 8 summarizes the results of the entire program and discusses the conclusions.

1.3 Summary of the Results

1.3.1 Scaled Experiments and Theory

An active vibration damper which uses a distributed piezoelectric actuator bonded directly to a structure, and 'bang-bang' feedback control (Lyapunov control) to damp transverse vibrations was experimentally tested on two different beams. One was a steel cantilever beam with a 6.7 gram tip mass. This was a dynamically scaled model of one arm of the AFAL structure. The second was an aluminum cantilever beam with a 2.04 kg tip mass; this was actually one of the arms of the full-scale AFAL structure.

Free vibration tests of the first mode of the steel beam were conducted by displacing the tip 2 cm, and releasing it. A beam without active control had a settling time of over 2 minutes. Free decay tests using the Lyapunov control algorithm and a control

amplitude of 500 volts decreased the settling time to 8 seconds. Similar first mode tests were performed on the aluminum beam. The initial condition for these tests was a tip displacement of 16.7 cm. Without active control the beam vibrations had a decay time of over 400 seconds. Using Lyapunov control with a control amplitude of 400 volts reduced the settling time to 126 seconds.

The active Lyapunov damping demonstrated in this study is nonlinear. If it were applied to a structure which had no internal damping, the tip displacement would decay linearly in time. This indicates a changing system loss factor. Using moderate feedback voltages, the effective loss factor of the closed loop system increased dramatically as the vibration level decreased. The passive loss factor of the steel beam was $\eta = 0.002$ for small amplitude tip displacements. Using the Lyapunov damper with an amplitude of 100 volts increased the loss factor to $\eta_{100} = 0.046$ at a tip displacement of 0.5 mm. Active damping with a 500 volt control amplitude increased the loss factor to $\eta_{500} = 0.375$ at the same displacement amplitude.

The passive loss factor at small tip displacements of the aluminum beam was $\eta = 0.0019$. Lyapunov control with an amplitude of 100 volts increased the system loss factor to $\eta_{100} = 0.030$ at a tip displacement amplitude of 1.7 cm. Active damping with a control amplitude of 400 volts increased the loss factor to $\eta_{400} = 0.080$.

The experimental results from the small-scale and full-scale tests were compared to nondimensional simulation results. Overall the experimental results match those predicted by the simulation. For large amplitude vibrations, unmodelled damping (such as air drag) caused higher damping than predicted by the simulation, especially for the full-scale beam. For small amplitude vibrations, the damping observed in the experimental tests approached the values predicted by the simulation.

Even though the small beam was dynamically scaled from the larger beam, the damping results could not be directly scaled. This was because the PVF₂ damper could not be dynamically scaled exactly because of experimental constraints (e.g., the PVF₂ film was not available in the appropriate thickness, and the large control voltages needed could not be generated easily). Nevertheless, the good correlation achieved between the experimental and simulation results validated the scaling parameters chosen, and allowed scaling laws to be used to predict the performance of other PVF₂ damper/beam combinations.

The Lyapunov damper was also demonstrated to be very effective on the second and third bending modes of the aluminum beam. The initial conditions for these tests were established by using the film actuator to excite the beam at the desired modal frequency. The Lyapunov control algorithm used on the first mode tests was also used for these tests. For the second mode of the aluminum beam, the initial condition was an angular acceleration at the tip of 56.5 rad s^{-2} . The Lyapunov control decreased the settling time from a free decay of 41 seconds to a controlled settling time of 7.4 seconds using a control amplitude of 400 volts. The initial condition for the third mode tests was an

angular acceleration of 127 rad s^{-2} at the tip. For the third mode the settling time was reduced from 20.5 seconds to 3.8 seconds using a control amplitude of 400 volts.

A constrained layer damper which uses the PVF₂ actuator as an active constraining layer was modelled and experimentally tested on a dynamically scaled model of an AFAL experiment arm. The general system consisting of a base structure, viscoelastic layer, and active constraining layer was modelled resulting in a sixth order partial differential equation governing the transverse motions of the beam. The specific case of an active constrained layer damper applied to a cantilevered beam with tip mass and rotary inertia was addressed.

This model revealed that there are two ways the active constraining layer affects the beam. The first is by contributing to the shear strain in the viscoelastic material (VEM) layer. As a result, it is possible to actively modulate the amount of energy dissipated. Since the amount of energy dissipated by the VEM is proportional to the strain, this mechanism is expected to be most effective for large amplitudes.

In addition to internal dissipation, the active control appears as work at the system boundary. With the constraining layer fixed to the tip mass and left free at the root, the active portion of the stress in the constraining layer appears as a boundary moment which can do work on the system. This result is similar to that found by Bailey [3] and is the basis of the Lyapunov control algorithm. In the limit, as the VEM becomes perfectly rigid and the loss modulus goes to zero, the model of the active constrained layer damper and the Lyapunov controller are identical. If the VEM has finite storage and loss moduli, the system will be affected by both the active dissipation and the boundary work.

The active constrained layer damper was tested experimentally with three different feedback control laws: (i) a proportional control law which fed back tip displacement to maximize the shear and shear rate across the VEM (within the constraints of a linear control law); (ii) a Lyapunov-based switching control law which fed back tip velocity to maximize the boundary work; and (iii) a proportional control law which fed back tip velocity as a linear version of the Lyapunov-based switching control law. The results of these tests show that dampers with thicker viscoelastic layers and stiffer (i.e. thicker) constraining layers add the most damping. A damper consisting of a 2.54×10^{-5} m thick VEM layer and a 110×10^{-6} m thick PVF₂ constraining layer consistently added the most damping to the structure for all the control laws. The experiments using the switching control law demonstrated the largest increase in damping for all damper configurations. The proportional control using position feedback was consistently the least effective control law. These results demonstrate that the maximum increase in damping due to active means for a damper using an active PVF₂ constraining layer and a viscoelastic damping layer is achieved by doing work on the system boundary and not by augmenting the shear losses in the viscoelastic layer.

An analysis of the stresses induced in the viscoelastic layer of both an active and

passive constrained layer damper showed that a passive design which used a steel constraining layer greatly outperformed the damper with the active PVF₂ constraining layer. This was because of the significant difference in the stiffness of the two constraining layers.

1.3.2 Full-Scale Experiment Verification Study

The analysis and control algorithm development was extended to focus on the full-scale experiment. A detailed model of the full-scale AFAL test structure was developed followed by the derivation of control laws for the PVF₂ film actuators. The actuators damp out flexural motion of the cantilevers measured relative to a coordinate frame fixed to the hub.

The key result of the analysis was that the film actuator exerts independent control in the governing equation for the flexural motion of the cantilever to which it is bonded. Although coupling of beam motion occurs through the hub, this coupling is a result only of inertia forces produced by beam and hub motion. These forces can be produced by a given set of initial conditions, external disturbances, or the motion of a beam induced by control action of the film. The stress field induced by the film is contained within the elastic continuum of that beam; it is not transmitted through the hub. For this reason, four identical but independent control laws were derived, one for each beam. The control laws require information only about the motion of the beam each is controlling. Essentially, the algorithm senses whether the net curvature of the beam is increasing or decreasing by differencing the angular rate of the free end and the fixed end, then the control law applies maximum voltage to the film such that the motion is opposed.

A key issue in technology development for the PVF₂ actuators concerns the method of attachment of the film actuator to the structure it is intended to control. This operation turned out to be much more difficult for components of the full-scale structure than for the small test specimens. A number of adhesives and different bonding techniques were tested before a satisfactory result was achieved. The successful procedure is summarized next.

The PVF₂ film actuators were bonded to each of the four AFAL test structure cantilever arms using Armstrong C-7 adhesive. This adhesive was chosen because of its relatively long pot life and good spreading qualities. The film was aligned before spreading a thin uniform layer of adhesive on the beam. Starting at one end of the beam, the film was pressed into place removing as much trapped air as possible. After the adhesive cured, the excess film was trimmed, and the exposed metalized surface of the film was spray painted with a layer of silver paint for improved conductivity.

The development effort produced several incidental findings including the following: The PVF₂ film (when used as an actuator) should be metalized on only one side if the

structure to which it is to be attached can provide the ground electrode. The surface of the film without metalization can be bonded directly to the surface of the cantilever thereby maximizing the bond strength. Also, metalization on only one side ensures that the PVF₂ actuators will all have the same polarity, i.e., a positive voltage applied to all films will cause all films to either contract or expand. While consistency in polarity is not an essential requirement for the application of the control law, it is a matter of convenience. Finally, it is noted that short circuits can develop between the two metalized faces of the film when it is cut. Generally, these shorts are removed with the first application of voltage.

A PVF₂ damper with four elements (one on each arm) was demonstrated on the full-scale AFAL structure using a Lyapunov-based control algorithm characterized by a nonlinear switching control law. Low-level, bandlimited random noise was input to the air-bearing table torque motor to excite the structure to perform transfer function identification tests. The loss factor achieved for each test was determined from the transfer function measurements. The active damping increased with decreasing vibration amplitude as a consequence of the nonlinear control.

Tests to identify transfer functions were performed using a range of excitation levels to determine the amplitude dependency of the loss factor. For the highest level of excitation, the loss factor for the first anti-symmetric flexible mode was increased from $\eta = 0.0056$ to $\eta = 0.0101$ using a voltage limit of ± 500 volts. The loss factor for the second anti-symmetric flexible mode increased from $\eta = 0.0179$ to $\eta = 0.0236$. With the same voltage limit but for the lowest level of excitation, the loss factor for the first mode was increased from $\eta = 0.0087$ to $\eta = 0.0176$ and the second mode loss factor increased from $\eta = 0.0916$ to $\eta = 0.1245$. The PVF₂ damper should be equally effective for both modes because the deformed shape of the beams for each mode was similar. However, the second anti-symmetric mode was excited the most by the torque motor and hence was damped by higher control forces from the PVF₂ actuators.

For the lowest level of excitation, the PVF₂ actuators added significant damping to the AFAL structure. The active damping added to the second anti-symmetric mode was large (an increase in η of 0.0329) but the corresponding reduction in resonant amplitude was small because of the large passive damping ($\eta = 0.0916$) associated with this mode at low vibration levels. The large passive damping was primarily due to nonlinear forces (friction and/or stiction) in the air-bearing table. The damping added to the first anti-symmetric mode was smaller (an increase in η of 0.0089) but resulted in a larger decrease in vibration amplitude because the baseline damping was very small ($\eta = 0.0087$).

1.4 Conclusions

This study has generally advanced technology development for PVF₂ film actuators and, in particular, their use for active structural vibration damping. The concept of using the piezoelectric characteristics of PVF₂ film to impart a distributed strain field to a structure to effect active control is relatively new. Early research indicated significant promise for this application but development was almost nonexistent. This situation warranted the investigation reported herein. During the investigation, it became apparent that many of the results were generally applicable to low-authority actuators, and not just PVF₂ film actuators.

Specific conclusions from the study are given in Section 8 and summarized below.

1.4.1 Value of Small-scale Tests

The PVF₂ actuators were developed initially using scaled models of an arm of the AFAL structure, progressing to a single full-scale arm of the structure, and finally to the entire structure. The small-scale tests were much faster and less costly to perform than full-scale tests. This approach allowed the researchers to perform many more tests and to gain experience with the PVF₂ film. As a result, many of the basic techniques needed to assemble PVF₂ actuators and to provide high voltage command signals were developed early in the program.

Additional benefits of the small-scale testing included the ease of actuator assembly, and valid scaling of results to the full-scale experiment. Novel damper configurations could easily be fabricated and tested using the small-scale models. Because the smaller test specimens were dynamically scaled from the AFAL structure, the modelling and analysis performed for the small structures could be legitimately scaled to the larger structures. For example, a full-scale version of the PVF₂ constrained layer damper was not implemented because the scaled-model results indicated that the tests would not be worthwhile.

1.4.2 Performance of the PVF₂ Actuators

Tests of several active vibration damper configurations which used PVF₂ film as a distributed-parameter actuator were very positive. A simple PVF₂ actuator with a nonlinear control law provided a factor of forty or more increase in damping for low-level vibrations, increasing as the vibration amplitude decreased. The relative increase in damping from the PVF₂ actuator was very large because the passive damping of the structure was very small ($\eta = 0.002$).

Tests of an alternative damper configuration which used the PVF₂ film as the con-

straining layer of a constrained layer damper were less successful. Experiments showed that most of the energy dissipation was performed by the boundary control effects of the damper (similar to the simple damper configuration). The viscoelastic layer did not contribute significant damping because the PVF₂ film was not stiff enough to act as a good constraining layer. It is conjectured that a constrained layer damper which uses a much stiffer constraining layer (perhaps steel foil) and with PVF₂ film embedded in the viscoelastic layer may produce a large passive damping which could be modulated with the PVF₂ film.

The four segment active damper applied to the full-scale AFAL structure provided active damping increases similar to those achieved in the small-scale tests. The PVF₂ actuators were extremely low authority actuators, providing on the order of 8×10^{-3} lb-ft of bending moment at a control voltage of 500 volts (less than the disturbance friction in the air-bearing table), yet were able to provide a significant increase in damping for low amplitude vibrations. When two modes were controlled simultaneously, the mode with the highest amplitude received the most active damping due to the nonlinear switching control law.

1.4.3 General Observations about Low Authority Actuators

The experiments demonstrated that low authority actuators (including the PVF₂ film) are not well-suited to remove the energy imparted by large transient disturbances (e.g., slewing or docking maneuvers) in a short time period. The actuators are inherently limited in the amount of energy they can remove during each cycle of vibration. Hence many cycles may be needed to damp such vibrations.

The steady-state effectiveness of low authority actuators for vibration control depends on the relative amounts of disturbance (or excitation) energy input to the system, the energy dissipated by means of passive damping, and the energy dissipated by active damping. If a large disturbance is present, the energy removed from the structure by a low authority actuator will be negligible. Similarly, if the energy removed by passive damping is large, the added damping from a low authority actuator will again be negligible. The passive damping energy can be large if either the system loss factor is large or the vibration amplitude is large. Therefore, low authority actuators will perform best when used in systems that have low disturbance forces and small loss factors. Possible uses for low authority actuators include damping of flexible appendages of spacecraft with long-term fine pointing requirements and, more generally, low-level disturbance rejection in very lightly damped structures.

Section 2

Distributed Active Damper Design using PVF₂

2.1 Damping of Distributed Space Structures

Engineering analysis has addressed the problem of increasing the damping in distributed structures using two different approaches. They are by increasing the inherent damping of the members in the structure via some passive means, or by doing negative work on the system using active actuators.

Passive designs are appealing because of their simplicity. A passive damper dissipates energy via experiencing thermodynamically irreversible deformation and is completely self contained. Passive damping can be designed into a structure by using high loss materials, or local damping elements. Use of free layer and constrained layer damping has been avoided because of the weight penalty it represents and bandwidth limitations. As a result, attempts have been made to damp certain target modes by employing local shear dampers around select members or joints. This local approach, however, has been shown to yield unpredictable results, and has the other unfavorable effect of redistributing energy out of certain modes and into others [5].

There are many difficulties in using discrete actuators to control distributed structures. Since the system to be controlled is of infinite order only a finite subset of modes can be controlled using discrete actuators. The plant model is usually separated into principle modes which are to be damped, and residual modes which will not be damped [6] [7]. The number of modes chosen to represent the system as well as the location of sensors and actuators is often difficult to reconcile [8] [9]. Historically, active dampers used in this context have been based on the use of discrete sensors/actuators and have used colocated velocity sensor and force actuator pairs. Using this approach the amount of damping per individual mode has been unpredictable and certain modes may experience limited damping, independent of the damping coefficient designed into the control system [10]. Another difficulty in the analysis and design of control systems for distributed systems is that the feedback loop tends to couple the initially uncoupled open loop modes. There exists the possibility of the controller exciting modes which are

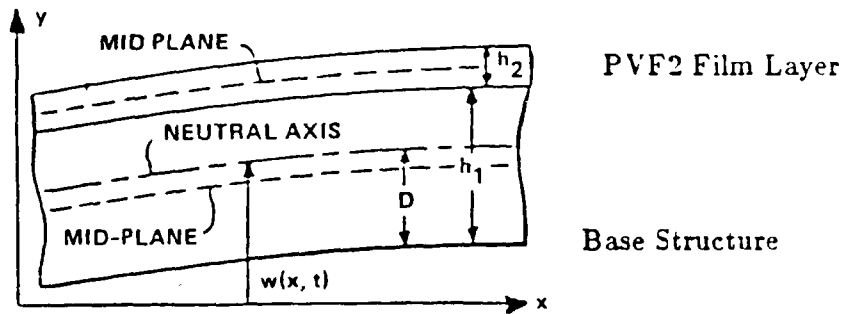


Figure 2-1. Lyapunov damper configuration.

left out of the dynamic model. This is called control spillover and can drive the unmodelled dynamics unstable. There is also the companion effect which is called observation spillover, sensors detecting modes which have been left out of the model, causing the compensator to react to these unmodelled dynamics. These two effects have been the subject of current research [11].

A vibration damper has been designed [3] which uses PVF₂ as a distributed actuator to achieve control over all transverse vibration modes of beams without truncation of the plant model. In what follows, the effectiveness of this method on a cantilever beam is experimentally verified and documented. In addition, a constrained layer damper which uses PVF₂ as an active constraining layer is developed. The modelling and effectiveness of this damper are also discussed.

2.2 Lyapunov Damper Development

Figure 2-1 shows the configuration of the Lyapunov damper developed. It is a single layer of PVF₂ bonded to one side of a beam. The effect of this configuration is to produce a voltage dependent bending moment which is distributed along the beam. In this study, a cantilever beam with mass and rotary inertia at the tip will be discussed (cf. Figure 2-2). The film and beam properties in this study are uniform along the beam length.

The equations of motion for the system shown in Figure 2-2 are:

$$E_1 I_1 \frac{\partial^4 w}{\partial x^4} + \rho b h_1 \frac{\partial^2 w}{\partial t^2} = 0 \quad (2-1)$$

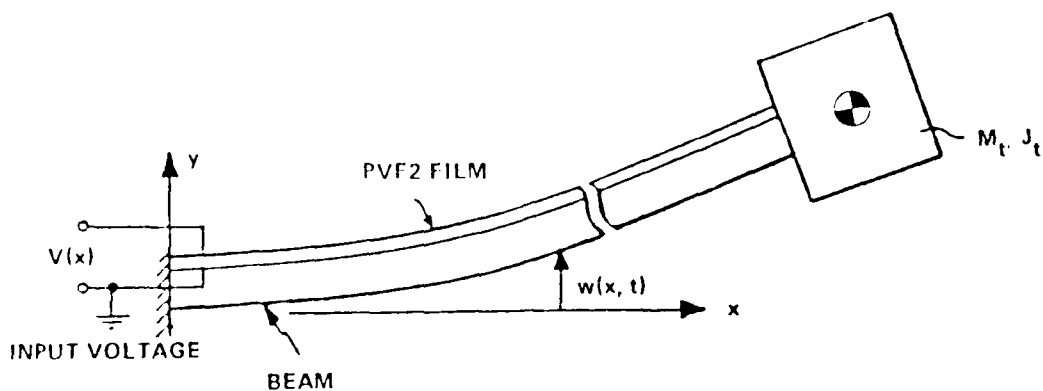


Figure 2-2. Lyapunov damper on a cantilevered beam with mass and rotary inertia at the tip.

with boundary conditions:

$$w = 0 \Big|_{x=0} \quad (2-2)$$

$$\frac{\partial w}{\partial x} = 0 \Big|_{x=0} \quad (2-3)$$

$$E_1 I_1 \frac{\partial^2 w}{\partial x^2} = -I_t \frac{\partial^3 w}{\partial t^2 \partial x} + \alpha v(t) \Big|_{x=L} \quad (2-4)$$

$$E_1 I_1 \frac{\partial^3 w}{\partial x^3} = M_t \frac{\partial^2 w}{\partial t^2} \Big|_{x=L} \quad (2-5)$$

With the film and beam properties spatially uniform, the integrated effect of the distributed moment manifests itself as a discrete moment located at the tip of the beam. It should be noted that for this configuration of spatially uniform voltage distribution, the control variable only appears in one boundary condition.

A feedback control law was derived using Lyapunov's Second Method since it can easily handle bounded inputs and can be extended to distributed parameter systems. The control law has been derived for a beam with no internal damping. In this study we will consider only the class of weak solutions of Equation (2-1), given boundary conditions in (2-2) and (2-3), which obey the conditions outlined by Kalmann and Bartram in [12].

A suitable Lyapunov-functional for the above model is,

$$F = \frac{1}{2} \int_0^L \left(\frac{\partial^2 w}{\partial x^2} \right)^2 + \left(\frac{\partial w}{\partial t} \right)^2 dx \quad (2-6)$$

where the first term in Equation (2-6) is a measure of the strain energy in the structure and the second term is a measure of its kinetic energy. With this choice of F , conditions which are at least sufficient for stability can be derived. [13][14].

A control law is found which will control all modes of vibration using only angular velocity at the tip of the beam as the feedback variable. The resulting control algorithm is given as;

$$v(t) = -\text{Sgn} \left(\frac{\partial^2 w}{\partial t \partial x} \Big|_{x=L} \right) \cdot V_c \quad (2-7)$$

where V_c is the bounded control voltage. For a decaying periodic input, this controller commands a constant amplitude square wave, or "bang-bang" control output.

The simulation written for this system assumes that the control will not significantly change the mode of vibration. It does not include the effects of air damping, however it does augment the model by adding passive damping in the form of a passive loss factor η which accounts for any internal structural damping which may be present. The first mode of vibration and the Lyapunov control law were chosen to demonstrate the simulation. The tip displacement represents the modal displacement. This simulation algorithm essentially gives the decay envelope of the vibration since the displacement amplitudes are determined every half cycle.

2.3 Experimental Verification of Lyapunov Control

2.3.1 Test Structures

The effectiveness of the switching control algorithm has been experimentally tested on two different structures. The first is a 0.152 m x 0.0127 m x 3.81x10⁻⁴ m steel beam, which is a dynamically scaled bench top version of one of the arms on the AFAL experiment. The second test was on one of the AFAL experiment arms. This was a 1.22 m x 0.152 m x 3.18x10⁻³ m aluminum beam. Both beams were configured as cantilevers with a mass and rotary inertia at the tip. Details on the dynamic scaling of the steel beam may be found in reference [3]. The dimensions and physical properties of the aluminum beam and the dynamically scaled steel model are given in Table 2-1. To obtain a clear understanding of how the damper performed, it was tested on structures vibrating in a single mode. The first bending mode was chosen because it was easiest to isolate and visually identify.

The physical properties of the PVF₂ film appear in Table 2-2 [15].

The passive damping of the laminated beam was determined using the logarithmic decrement method. For large tip amplitudes (on the order of 2.0 cm), the passive loss

Table 2-1. Beams used in Lyapunov damper tests.

	Aluminum	Steel
Modulus, E , (Nm^{-2})	76×10^9	210×10^9
Length, L , (m)	1.22	0.152
Thickness, h , (mm)	3.18	0.381
Width, b , (cm)	15.2	1.27
Tip Mass, M_t , (kg)	2.04	6.73×10^{-3}
Tip Inertia, J_t , (kgm^2)	1.1×10^{-2}	5.0×10^{-7}
Density, ρ , (kgm^{-3})	2840	7800

Table 2-2. PVF₂ film properties.

Modulus, E , (Nm^{-2})	2.0×10^9
Static Piezoelectric constant, d_{31} , (mV^{-1})	22×10^{-12}
Thickness, h_3 , (m)	23×10^{-6}
Density, ρ , (kgm^{-3})	1300

Table 2-3. Nondimensional parameters.

Dimensionless Length	$X = \frac{x}{L}$
Dimensionless Displacement	$W = \frac{w}{L}$
Dimensionless Control Voltage	$V_1 = \frac{\alpha v L}{E_3 I_3}$
Dimensionless Time	$T = t \cdot \sqrt{\frac{EI}{\rho b h_3^3 L^4}}$

factor was determined to be $\eta = 0.003$. * For small amplitudes (1 mm), the passive loss factor was less than 0.002. The larger loss factor at large tip displacements may be the result of operating beyond the linear range of the material or air drag. Application of the film to the beam did not significantly alter the passive damping in the structure, which was ignored in the derivation of the mode shapes and frequencies.

2.3.2 Scaled Steel Cantilever Beam Results

Figure 2-3 shows oscilloscope traces of tests for various control voltages. The figure gives a global perspective of the effectiveness of the active damper as the control voltage amplitude, V_c of Eq. (2-7), was varied from 0 volts to 500 volts. It is easily seen that the settling time is decreased dramatically from a free decay time of over 2 minutes to a damped settling time of 8 seconds.

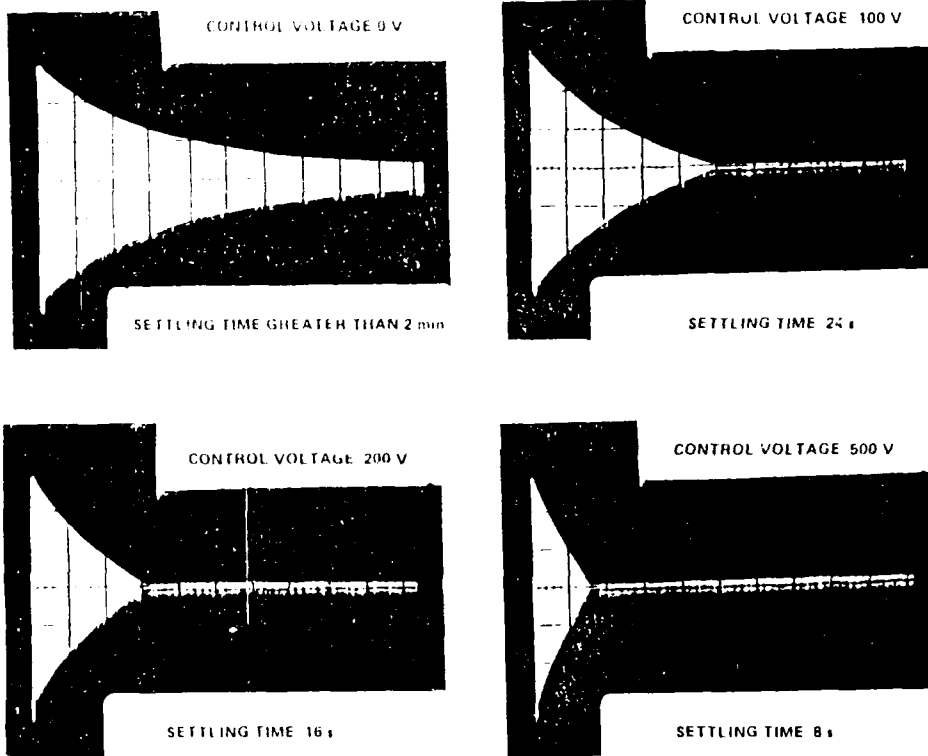
To facilitate comparison with simulations, the beam properties were nondimensionalized using the relationships given in Table 2-3. Figure 2-4 is a plot of both simulation and experimental results showing the decay envelopes for several control voltages. A more detailed discussion of these results is deferred to Section 2.4.

2.3.3 AFAL Experiment Cantilever Beam Results

The Lyapunov damper was also tested on a AFAL experiment arm. Because of the small angular displacement at the tip and the very low frequency of the first mode (less than 1 Hz.), an angular accelerometer was unable to measure accurately the first mode. Therefore for the active damper tests the tip mass of the beam was fitted with both an angular and linear accelerometer. The linear accelerometer was limited to sensing only the first mode by low pass filtering the output. The outputs of both sensors were

* For linear structures, $\eta = 2 \cdot \zeta$

TIP DISPLACEMENT DECAY ENVELOPES FOR BENCH SCALE BEAM



8-111-10-21

ALL DECAY ENVELOPES ARE FOR A 20 cm INITIAL DISPLACEMENT

Figure 2-3. Damping results of lyapunov control on first mode of steel beam.

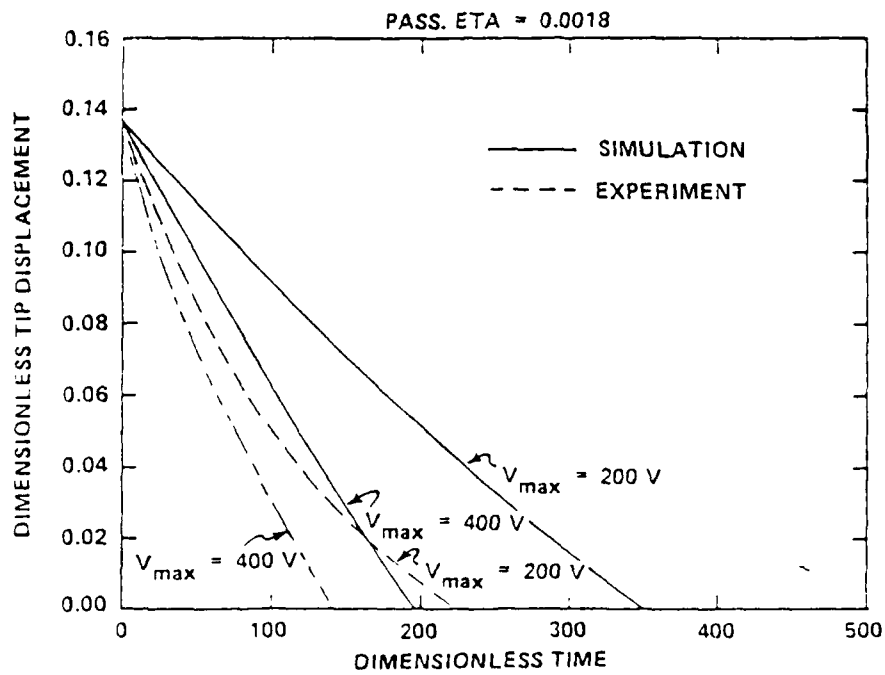
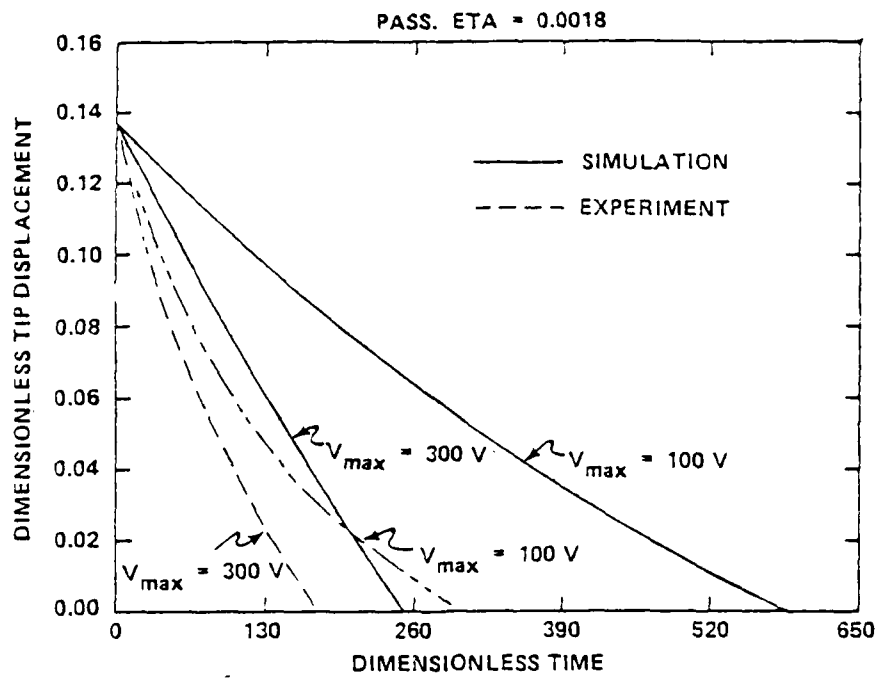


Figure 2-4. Experimental and simulated decay envelopes for the 6 inch test structure.

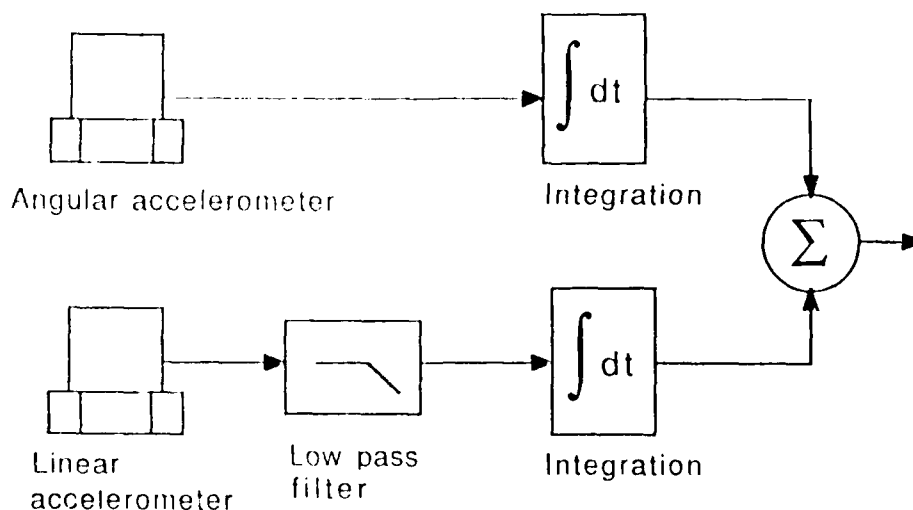


Figure 2-5. Sensor configuration used in aluminum beam tests.

then integrated and summed to produce the control input. Figure 2-5 shows this sensor configuration schematically.

First mode tests using the aluminum beam were made by displacing the beam tip 16.7 cm and releasing it. Figure 2-6 shows time plots of tip displacements for various control voltages. Once again the effect of the control is quite pronounced with the settling time being decreased from over 409 seconds to a damped settling time of 126 seconds. To facilitate comparison with simulations, the beam properties were also nondimensionalized using the relationships given in Table 2-3. Figure 2-7 is a plot of both simulation and experimental results showing the decay envelopes for several control voltages.

2.3.4 Higher Mode Results

The Lyapunov controller was also successfully applied to the second and third bending modes of the aluminum beam. For these higher mode tests the PVF₂ was used to establish the initial condition of acceleration. The film was used to drive the beam by using the Lyapunov control algorithm with positive (destabilizing) feedback, rather than negative feedback. In this configuration the control would sense the modes which had been excited and drive them rather than damp them. Isolated modes were excited by giving the beam a displacement disturbance near a known local maximum of the mode of interest. The control would then preferentially drive this mode. This is a consequence of using the Lyapunov controller. It detects and damps the mode with the largest angular velocity at the tip. With the controller acting in a positive feedback loop it continually excited the mode with the largest angular velocity. After a time, all the

TEST RESULTS FROM FULL-SCALE PASSIVE ARM OF
RPL-EXP PVF₂ ACTIVE DAMPING (FIRST MODE)

INITIAL CONDITIONS: 16.7 cm TIP DISPLACEMENT

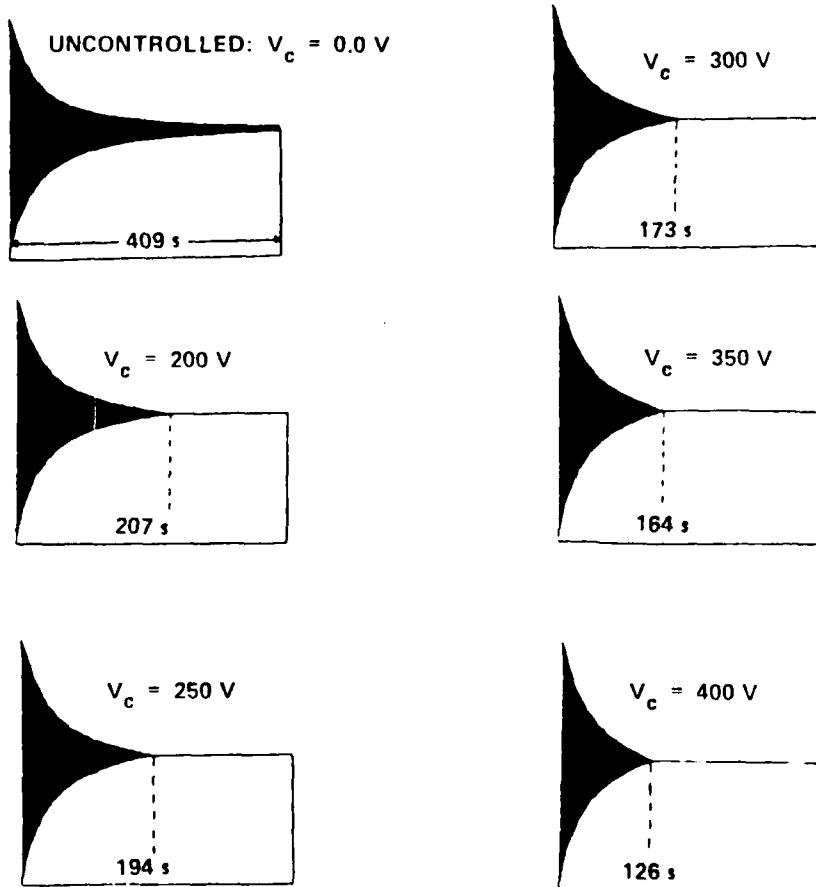


Figure 2-6. Damping results of lyapunov control on the first mode of the aluminum structure.

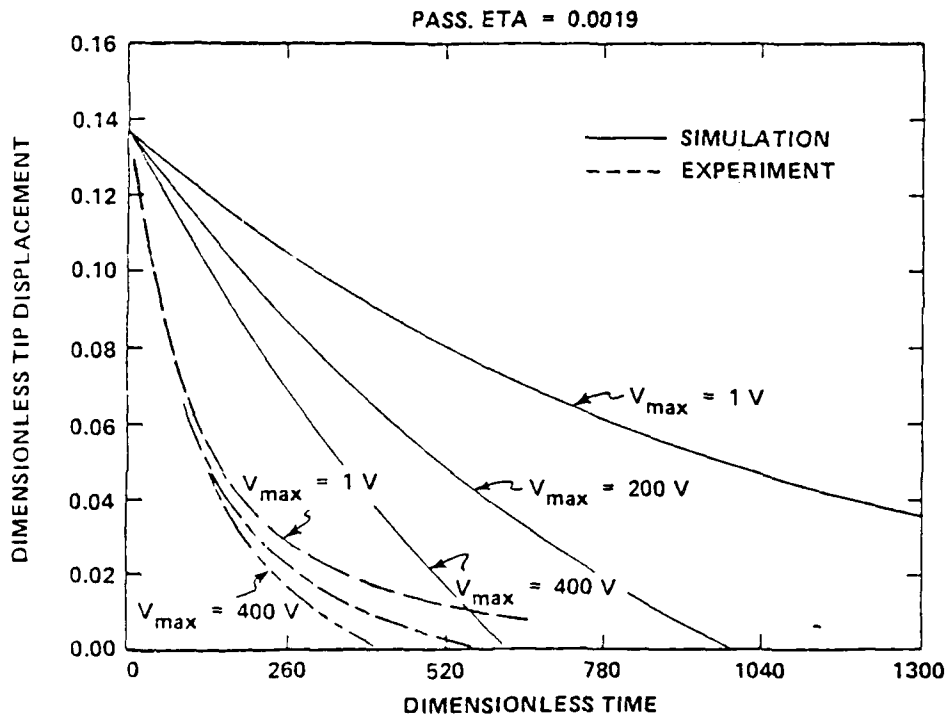
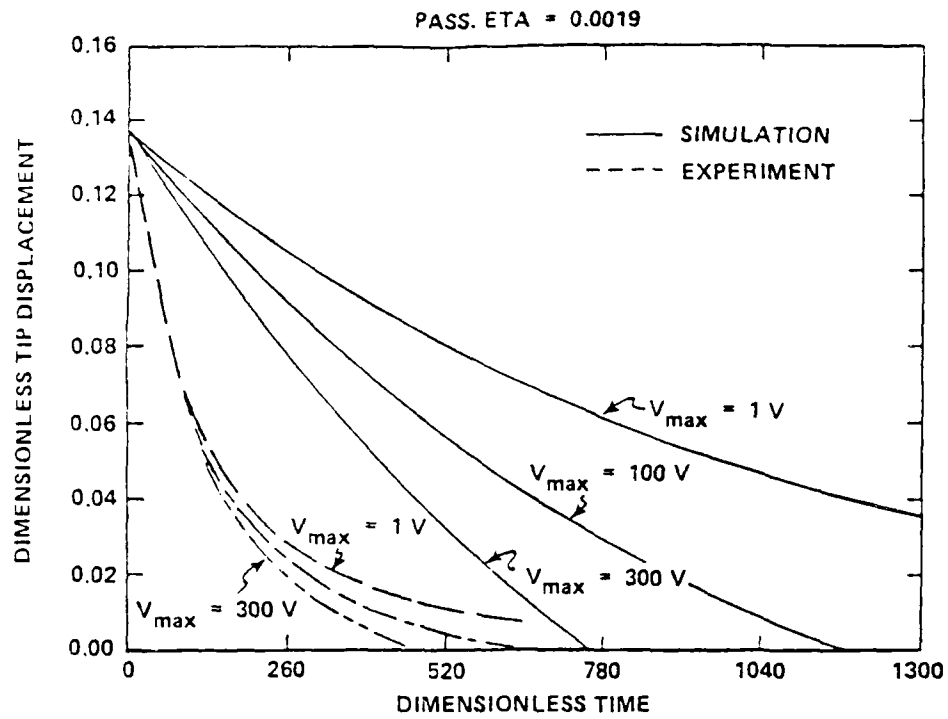


Figure 2-7. Experimental and simulated decay envelopes for the aluminum test structure.

vibrational energy in modes not being driven was dissipated due to natural damping, and the system would be left vibrating in a single higher mode. This technique guaranteed that the system would be excited in a natural mode.

Tests were run by establishing an initial condition, and then enabling the active damping. Passive damping for the second mode was found from modal analysis to be $\eta = 0.0048$. The initial condition for all second mode tests was a peak angular acceleration at the tip of 56 rad s^{-2} . The effect of the Lyapunov damper was to reduce the settling time from over 40 seconds to 7.4 seconds using a control amplitude of 400 volts. The results of the second mode tests appear in Figure 2-8.

Passive damping in the third mode was found to be $\eta = 0.0037$. The initial condition for all third mode tests was a peak angular acceleration at the tip of 127 rad s^{-2} . For this mode, active damping decreased the settling time from 20 seconds to 3.8 seconds using a control amplitude of 400 volts. The results of the third mode tests are presented in Figure 2-9. No simulation was performed for the higher modes.

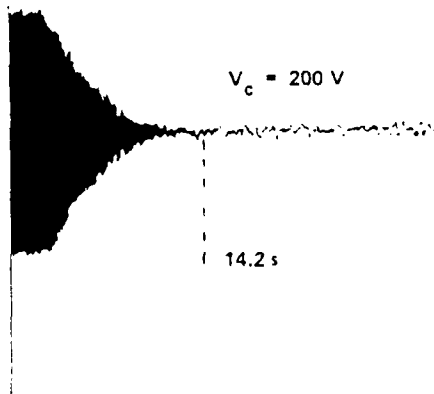
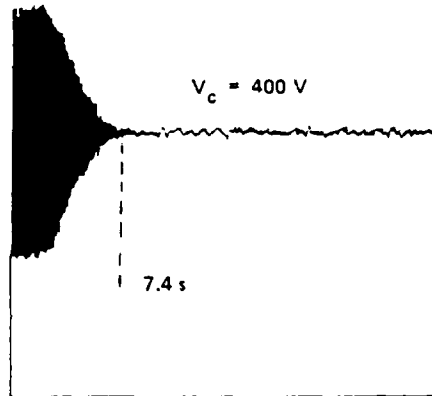
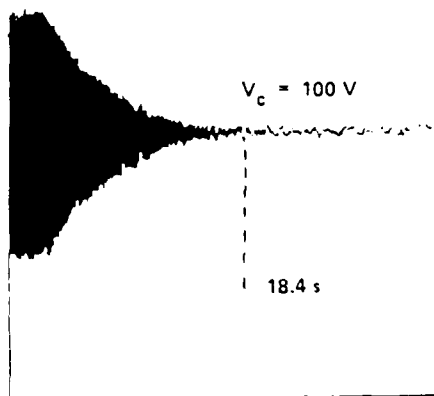
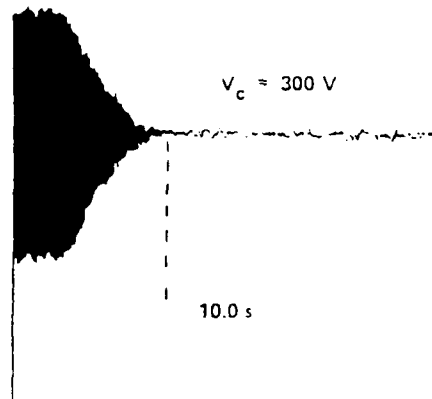
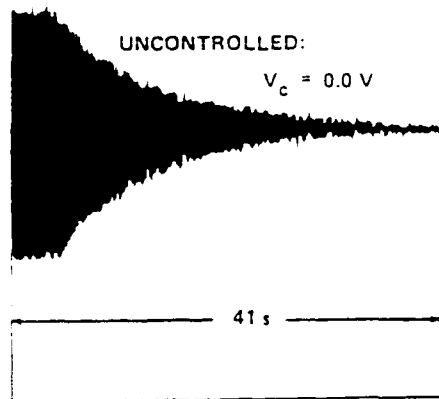
2.4 Discussion of Lyapunov Control Effectiveness

The Lyapunov controller has been demonstrated to be effective on two different scale structures. The resulting damping of this nonlinear control algorithm is amplitude dependent. Consider the response of a beam with no internal damping. The application of the Lyapunov damper would cause the vibration amplitude to decay linearly in time. The resulting linear decay envelope indicates a changing effective loss factor, which increases as the vibration levels decrease. The active damping is most effective for smaller vibration levels because a nonlinear control law such as this one dissipates an increasing percentage of the system energy as the vibration amplitude decreases. Even though the amount of energy dissipated per cycle is decreasing, the amount of energy in the system is decreasing faster.

The initial slope of all experimental decay envelopes are steeper than their corresponding predictions. This result is expected and is due to the presence of additional, unmodelled loss mechanisms being present in the physical structure. These added losses could be the result of air drag, structural nonlinearities, and/or losses occurring in the mounting fixture. As the tip amplitude decreases, however, the effects of these other damping mechanisms become negligible and the energy dissipation is primarily due to the active damping. The final slope of the decay envelope is predicted by the simulation to be:

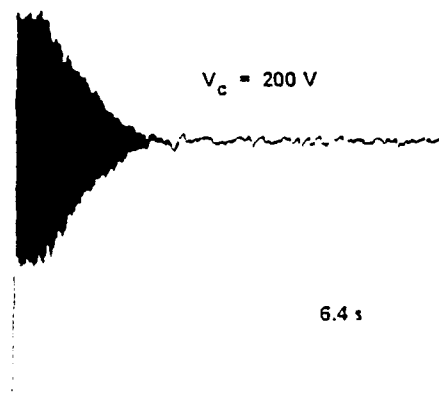
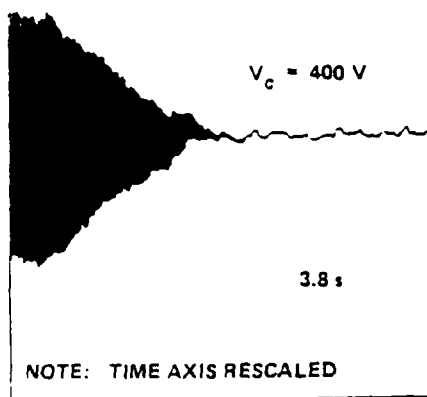
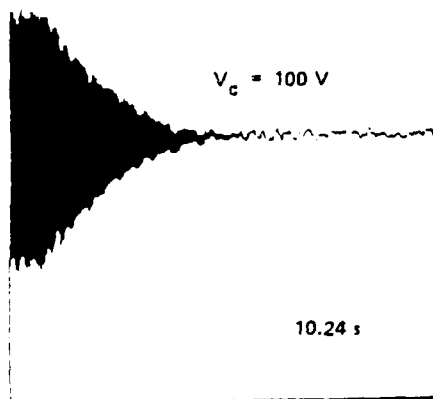
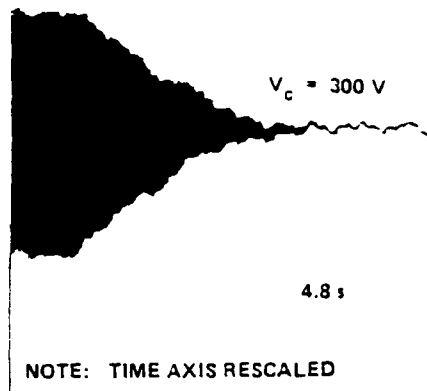
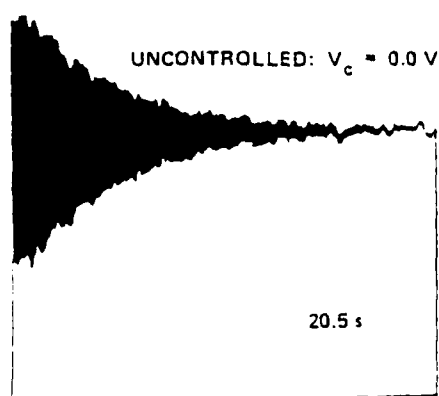
$$\frac{\Delta d_t}{|\Delta t|} = \frac{V_c \cdot f}{g \cdot \theta} \quad (2 \quad 8)$$

where f is a modal constant relating dimensionless strain energy to dimensionless tip displacement, and g is a modal constant relating angular tip displacement to linear tip



NOTE: INITIAL CONDITION FOR ALL TEST:
 56.5 radians/s^2
 PASSIVE LOSS FACTOR = 0.003

Figure 2-8. Damping results of lyapunov control on second mode of aluminum beam.



INITIAL CONDITIONS FOR ALL TEST:
 127 radians/s^2

Figure 2-9. Damping results of lyapunov control on third mode of aluminum beam.

displacement. These parameters are defined by Bailey [3] and are dependent on the beam geometry, material, and boundary conditions. θ is the half period of vibration. A comparison of decay envelopes between simulation and the steel beam experiments show the final slopes to be identical, with the final settling time shifted due to the initial effects of added damping at large displacements. At lower control voltages and large amplitudes, passive damping is the dominant dissipation mechanism, while the active damping supplied by the PVF₂ is dominant at small amplitudes of vibration. At the higher control voltages active damping begins to dominate the overall response of the beam. This is evident by the gradual flattening out of the decay envelopes as the displacement amplitude decreases.

The loss factor of the controlled structure was determined experimentally when the tip displacement amplitude was 0.5 mm. With a control voltage amplitude of 100 volts, the loss factor was $\eta_{100} = 0.046$. The loss factor when using 200 and 500 volt control amplitudes was $\eta_{200} = 0.087$, and $\eta_{500} = 0.375$ respectively.

A comparison was also made between the predictions of the simulation and the experimental results of the full scale beam (applied to the first bending mode). Figure 2-7 is a plot of tip displacement vs. time for the full scale beam whose dimensions were given in Table 2-1. The results are almost identical to those obtained for the dynamically scaled beam. The effect of unmodelled damping, however, is much more evident, and persists over a much broader range of tip displacements. At small tip displacements where the active damping is expected to dominate, the slopes of the decay envelopes converge to the same value as expected. There is, however, a slight difference between the final slopes as predicted by Eq. (2-8) and the experimental results. This difference is believed to be due to parameter uncertainties associated with aluminum beam.

The passive loss factor of the aluminum beam for small tip displacements was $\eta = 0.0019$. Lyapunov control with an amplitude of 100 volts increased the system loss factor to $\eta_{100} = 0.030$ at a tip displacement amplitude of 1.7 cm. Active damping using a control amplitude of 400 volts increased the loss factor to $\eta_{400} = 0.080$ at the same vibration amplitude.

These experimental results support the analysis and simulation and indicate that an active damper with this type of control law may provide a method of keeping resonant vibrations from building up due to the extremely high levels of damping that can be achieved for low level vibrations. Similarly, the use of the PVF₂ film to excite the beam gives a clear understanding of just how this low authority actuator can be used effectively. As an actuator operating in a regime which is damping controlled, this actuator is able to cause quite large responses.

Section 3

Active Constrained Layer Damper Design

3.1 Constrained Layer Dampers

The performance of the Lyapunov damper previously discussed has been shown to be most effective at low amplitude vibration levels. A design is sought which will be effective at larger levels. An active damper would need powerful actuators to be effective on large amplitude vibrations. This is because of the large amount of potential energy present. Possible damper designs which would be effective on a wider range of vibration levels could incorporate very powerful actuators for large amplitudes and the Lyapunov control for low levels, but this is at the cost of increased complexity. An alternate design philosophy is to increase the passive damping of the structure. The level of passive damping has been shown to be the primary dissipation mechanism for large amplitude vibrations. Therefore the simplest design would call for increased passive damping to control the large amplitude vibrations, which would be augmented by the active damper at low vibration levels.

The primary methods of increasing the passive damping in a distributed structure are free layer and constrained layer viscoelastic damping. Both methods rely on the strain of a viscoelastic material (VEM) to dissipate energy (cf. Figure 3-1). In a free layer damper the dilatation strain is of the same order as the shear strain [16]. If the viscoelastic layer is covered with a stiff constraining layer, it experiences much greater shear and relatively small dilatation. Since most of the energy is dissipated by shear in the damping layer, using a constraining layer is very effective [17]. A simple way of incorporating the active properties of PVF_2 into a constrained layer design would be to substitute a layer of PVF_2 into the design as the constraining layer.

The prospect of an active constraining layer is attractive because it allows the shear in the viscoelastic layer to be modulated actively, thereby increasing the damping effectiveness over a broader operating range. With a passive constrained layer damper, the shear, and therefore the rate of energy dissipation from the structure, tends toward zero as the vibration amplitude decreases. Also, passive constrained layer dampers are

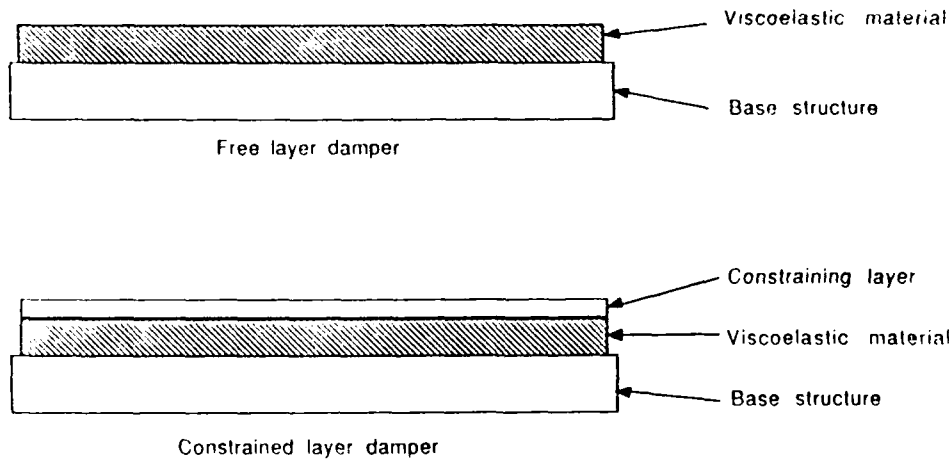


Figure 3-1. Free layer and constrained layer dampers.

designed for a single target mode. With an active constraining layer it would be possible to have a finite dissipation rate at low amplitudes. There also exists the possibility of combining the large amplitude performance of a constrained layer damper with the low amplitude performance of the PVF₂ laminate controller in one design.

This section discusses the modelling of an active constrained layer damper which uses PVF₂ as the constraining layer.

3.2 Modelling of an Active Constrained Layer Damper

The modelling of an active constrained layer damper is presented. The result is a sixth order partial differential equation governing the transverse bending motion of a damped, finite length beam. In addition, a cantilevered beam with a mass and rotational inertia located at the tip will be discussed.

The geometry of the system being modelled is shown in Figure 3-2. Subscripts 1, 2, and 3 refer to the constraining layer, viscoelastic layer and beam layer respectively. The model is based on the following assumptions:

- (1) The constraining and viscoelastic layers have no bending stiffness.
- (2) The viscoelastic layer can only transmit shear.
- (3) All dissipation losses occur within the VEM.
- (4) There exists a uniform state of shear in the VEM.

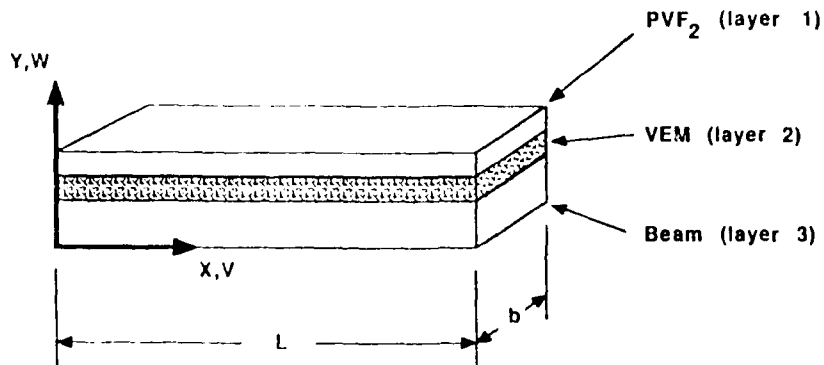


Figure 3-2. Beam section with constrained layer damper.

- (5) Uniform normal stress throughout the thickness of the constraining layer.
- (6) Rotational inertia of the beam is ignored. (i.e. Bernoulli-Euler beam theory)
- (7) The beam and film properties are spatially uniform.

The procedure will be:

- (1) Derive the strain field within the VEM.
- (2) Satisfy equilibrium and compatibility.
- (3) Introduce boundary conditions.

Consider an element of a beam in bending (cf. Figure 3-3). The displacement of a point on the surface of the beam can be decomposed into two terms. One associated with the displacement due to the slope of the beam and the second term due to the strain of the neutral axis itself. Let Δ_3 be the displacement of a point on the top surface of the element in bending. Then Δ_3 is given by Eq. (3-1).

$$\Delta_3(x) = \int_0^x \frac{\sigma_3}{E_3} d\eta + \frac{\partial w}{\partial x} \cdot \frac{h_3}{2} \quad (3-1)$$

The displacement field of the constraining layer, Δ_1 is also composed of two terms. One is the rigid body translation of the constraining layer relative to the base structure and will be designated δ_0 . A second term is due to the strain of the constraining layer.

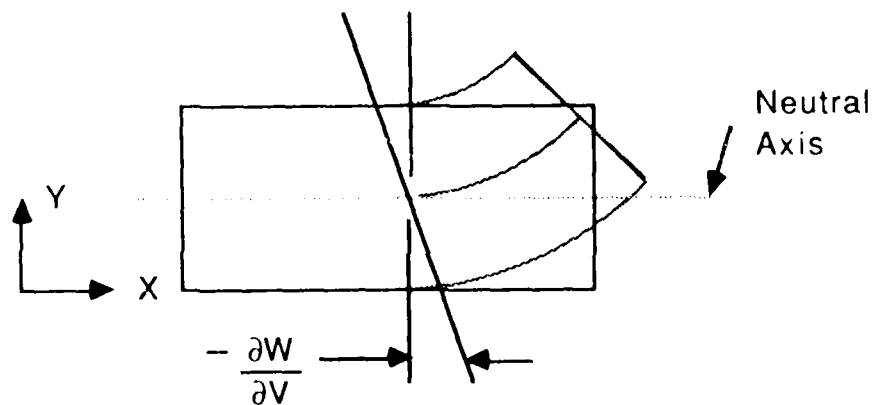


Figure 3-3. Beam element in bending.

The strain in the constraining layer is caused by the mechanically induced stress, σ_1 , and as a result of its piezoelectric properties, $\frac{d_{31}}{h_1}v$. (Eq. (3-2))

$$\Delta_1(x) = \delta_0 + \int_0^x \left(\frac{\sigma_1}{E_1} + \frac{d_{31}}{h_1}v \right) d\eta \quad (3-2)$$

The displacement field within the viscoelastic material, Δ_2 , is the linear interpolation between layers 1 and 2, and is given by Eq. (3-3).

$$\Delta_2(x) = \Delta_3(x) \left(\frac{h_3 + h_2 - y}{h_2} \right) + \Delta_1(x) \left(\frac{y - h_3}{h_2} \right) \quad (3-3)$$

The shear strain in the VEM is found by differentiating the displacement field and is given by Eq. (3-4). The resulting shear stress in the VEM is given by Eq. (3-5).

$$\gamma_2(x) = \frac{\partial \Delta_2(x)}{\partial y} \quad (3-4)$$

$$\tau_2(x) = g_2 \gamma_2(x) \quad (3-5)$$

The free body diagram in Figure 3-4 shows the stresses on a differential element of the composite beam. The force balance equations in the x and y directions are given

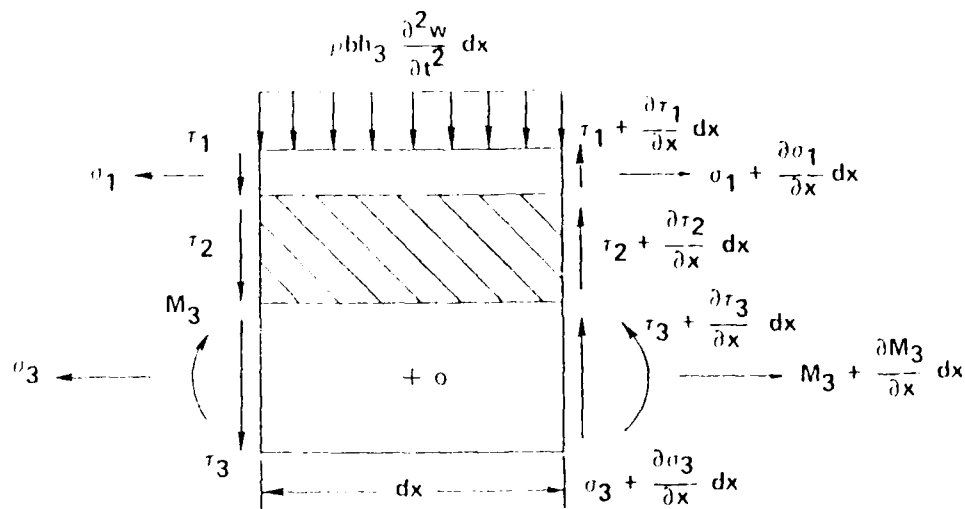


Figure 3-4. Free body diagram of an element of a damped sandwich beam.

by Eq. (3-6), and Eq. (3-7). Moment equilibrium of the element about point O is given by Eq. (3-8).

$$h_1 \frac{\partial \sigma_1}{\partial x} - h_3 \frac{\partial \sigma_3}{\partial x} = 0 \quad (3-6)$$

$$\rho h_3 \frac{\partial^2 w}{\partial t^2} - h_1 \frac{\partial \tau_1}{\partial x} + h_2 \frac{\partial \tau_2}{\partial x} + h_3 \frac{\partial \tau_3}{\partial x} = 0 \quad (3-7)$$

$$\tau_1 h_1 - \tau_2 h_2 - \tau_3 h_3 - \frac{1}{b} \frac{\partial M_3}{\partial x} - h_1 \beta \frac{\partial \sigma_1}{\partial x} = 0 \quad (3-8)$$

Combining these equations and the moment-curvature relationship of a beam in bending (Eq. (3-9)) yields;

$$M_3 = E_3 I_3 \frac{\partial^2 w}{\partial x^2} \quad (3-9)$$

$$\frac{\partial^4 w}{\partial x^4} + \frac{\partial^2 w}{\partial t^2} = \frac{\partial^2 \sigma_1}{\partial x^2} \quad (3-10)$$

Finally, a relationship between the stress in the constraining layer and the beam deflection is needed to complete the model. Force equilibrium on the differential element of the constraining layer shown in Figure 3-5 yields Eq. (3-11).

$$\tau_2 = h_1 \frac{\partial \sigma_1}{\partial x} \quad (3-11)$$

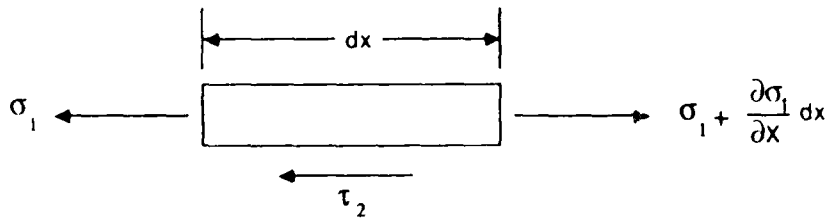


Figure 3-5. Free body diagram of constraining layer of constrained layer damper.

Combining this expression with Eqs. (3-3), (3-4), and (3-5) and differentiating yields:

$$\frac{\partial^2 \sigma_1}{\partial x^2} = \frac{g_2}{h_1 h_2} \left[h_3 \frac{\partial^2 w}{\partial x^2} + \sigma_1 \left(\frac{1}{E_1} + \frac{h_1}{h_3 E_3} \right) + \frac{d_{31} v}{h_1} \right] \quad (3-12)$$

To facilitate analysis, the following expressions are used for nondimensionalization.

$$W = \frac{w}{L} \quad (3-13)$$

$$X = \frac{x}{L} \quad (3-14)$$

$$V = \frac{v d_{31}}{h_1} \quad (3-15)$$

$$G = \frac{g_2 L^2}{h_1 h_2} \left(\frac{1}{E_1} + \frac{h_1}{h_3 E_3} \right) \quad (3-16)$$

$$\sigma = \frac{\sigma_1 L b h_1 \beta}{E_3 I_3} \quad (3-17)$$

$$A = \frac{L b h_1 \beta E_1 E_3 h_3}{E_3 I_3 (h_3 E_3 + h_1 E_1)} \quad (3-18)$$

$$B = \frac{h_3}{2L} \quad (3-19)$$

$$T = t \sqrt{\frac{E_3 I_3}{\rho b h_3 L^4}} \quad (3-20)$$

$$\tau = \frac{\tau_2 L^2 b \beta}{E_3 I_3} \quad (3-21)$$

$$J = \frac{J_t}{\rho b h_3 L^3} \quad (3-22)$$

$$M = \frac{M_t}{\rho b h_3 L} \quad (3-23)$$

$$r = \frac{\beta}{L} \quad (3-24)$$

The final set of equations is then

$$\frac{\partial^4 W}{\partial X^4} + \frac{\partial^2 W}{\partial T^2} - \frac{\partial^2 \sigma}{\partial X^2} \quad (3-25)$$

$$\frac{\partial^2 \sigma}{\partial X^2} - G\sigma - GAB \frac{\partial^2 W}{\partial X^2} + GAV \quad (3-26)$$

Combining Eqs. (3-25) and (3-26) yields the sixth order partial differential equation:

$$\frac{\partial^6 W}{\partial X^6} - G(1 + AB) \frac{\partial^4 W}{\partial X^4} + \frac{\partial^4 W}{\partial X^2 \partial T^2} - G \frac{\partial^2 W}{\partial T^2} - AG \frac{\partial^2 V}{\partial X^2} = 0 \quad (3-27)$$

The governing differential equation is of sixth order, therefore six boundary conditions need to be specified. Four of these are the usual boundary conditions associated with beam end conditions. The beam boundary conditions which will be used here are those used in the earlier study, a cantilevered beam with tip mass and rotational inertia. They are given by Eqs. (2-2) to (2-5). The two additional boundary conditions are imposed on the VEM and constraining layer. A short listing of some candidate boundary conditions are discussed by Mead [18]. The boundary conditions chosen in this application are relatively simple. The first is specifying zero tensile stress in the constraining layer at the root end of the beam. This corresponds to a free end of the constraining layer. The second is specifying zero shear stress in the VEM at the tip. These boundary conditions are given by Eqs. (3-28) and (3-29) respectively.

$$\left. \frac{\partial^4 W}{\partial X^4} + \frac{\partial^2 W}{\partial t^2} - GAB \frac{\partial^2 W}{\partial X^2} - GAV = 0 \right|_{X=0} \quad (3-28)$$

$$\left. \frac{\partial^5 W}{\partial X^5} + \frac{\partial^3 W}{\partial X \partial t^2} - GAB \frac{\partial^3 W}{\partial X^3} - GA \frac{\partial V}{\partial X} = 0 \right|_{X=L} \quad (3-29)$$

Figure 3-6 shows schematically a beam with these boundary conditions.

3.3 Energy Dissipation with an Active Constrained Layer Damper

The energy removed from the structure will be due to two effects, dissipation within the shear layer, and active work done on the boundary. The internal dissipation can be further resolved into a passive component, which is present in all constrained layer dampers, and an active component which is due to the piezoelectrical properties of the constraining layer. These three distinct energy pathways, passive dissipation, active dissipation, and boundary work, will be discussed separately.

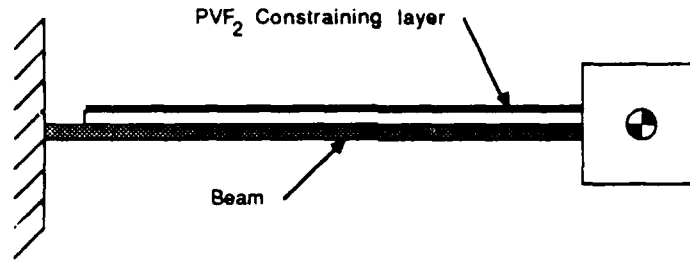


Figure 3-6. Cantilevered beam with active constrained layer damper.

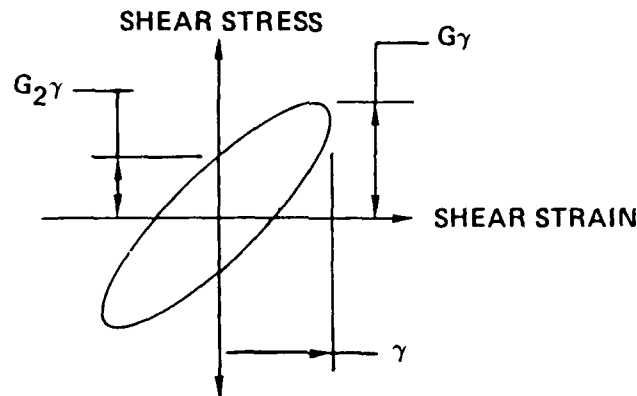


Figure 3-7. Hysteresis loop of a viscoelastic material.

Energy dissipation within a viscoelastic material is a result of the stress and strain histories having components in quadrature with one another, and is equal to the area of the hysteresis loop of the material's stress-strain diagram. (cf. Figure 3-7) In the analysis that follows, forced, sinusoidal steady state vibrations are considered. This assumption allows the use of a complex shear modulus to evaluate internal losses. The modulus is of the form

$$G = (G_1 + j \cdot G_2) \quad (3 - 30)$$

where G_1 and G_2 are the storage and loss moduli of the viscoelastic material respectively.

The loss factor of a system with a passive constrained layer damper can be found using the approximate relationship [19]:

$$\eta = 12\phi\eta_2 \frac{\frac{E_1 h_1}{E_3 h_3} \left(\frac{\beta}{h_3}\right)^2}{1 + 2\phi + \phi^2(1 + \eta_2^2)} \quad (3 - 31)$$

Table 3-1. Final design values of passive constrained layer damper using PVF₂ as the constraining layer.

Constraining Layer	PVF ₂
Thickness (m)	2.5x10 ⁻⁵
VEM Modulus (Nm ⁻²)	1.58x10 ⁴
VEM Loss Factor	1.2
VEM Thickness (m)	3.01x10 ⁻³
System Loss Factor	0.098
h ₂ /h ₃	7.9

$$\phi = \frac{\eta_2}{2\pi f E_1 h_1 h_2} \left(\frac{E_3 I_3}{\rho b h_3} \right)^{\frac{1}{2}} \quad (3 - 32)$$

Where ϕ is defined as the nondimensional shear parameter, and η_2 is the loss factor of the viscoelastic layer. The system loss factor is defined as the ratio of the energy dissipated per cycle to the peak strain energy in the structure during that cycle. For effective passive constrained layer designs, the shear parameter should be near unity [19]. For this reason passive constrained layer dampers can usually only be optimized for a single mode.

A passive constrained layer damper which used PVF₂ as the constraining layer was designed to damp the first mode of the 0.152 m steel beam previously discussed (cf. Table 2-1). With this design, there were only two design variables which could be varied. They were the VEM shear modulus, and the VEM thickness. Given that there is a practical lower limit on the shear modulus of real materials, the design required a very thick shear layer to arrive at a low shear parameter. To minimize the shear layer thickness and therefore the damper weight, a low shear modulus material was sought. An available material was found in the literature [20], and a damper was designed based on its use. The thickness of the shear layer was determined by setting the shear parameter to unity. The final design values for this damper appear in Table 3-1. The system loss factor for this design was $\eta = 0.098$. Although this is quite good, the design is a poor one. In order to achieve the desired shear parameter, the VEM thickness had to be increased until it was on the order of 8 beam thicknesses! The necessity of such a thick damping layer was a direct result of the low constraining layer stiffness. By comparison, using a steel constraining and the same VEM would yield a design with a

Table 3-2. Passive constrained layer damper design using a steel constraining layer.

Constraining Layer	Steel
Thickness (m)	2.5×10^{-5}
VEM Modulus (Nm^{-2})	1.58×10^4
VEM Loss Factor	1.2
VEM Thickness (m)	5.95×10^{-5}
System Loss Factor	0.087
h_2/h_3	0.16

similar loss factor, but a much thinner VEM layer. (cf. Table 3-2)

Alternatively, increasing the thickness of the PVF₂ by a factor of three or four would produce reasonable designs.

The active effects of the damper are a result of piezoelectrically induced stresses. Since the system is linear, the stresses can be resolved into their active and passive components. The actively induced normal stress in the constraining layer can be found by solving Eq. (3-26) with the modal displacement of the beam set to zero. That is solving:

$$\frac{\partial^2 \sigma}{\partial X^2} - G\sigma = GAV \quad (3-33)$$

Using boundary conditions (3-28) and (3-29), this gives:

$$\sigma_V(X, T) = VA \left[\cosh(\sqrt{|G|}X) - 1 - \tanh(\sqrt{|G|}) \cdot \sinh(\sqrt{|G|}X) \right] \quad (3-34)$$

From Eq. (3-11), the active shear stress is found to be:

$$\tau_V(X, T) = VA\sqrt{|G|} \left[\sinh(\sqrt{|G|}X) - \tanh(\sqrt{|G|}) \cosh(\sqrt{|G|}X) \right] \quad (3-35)$$

or more compactly:

$$\tau_V(X, T) = VA\sqrt{|G|} \cdot f(X) \quad (3-36)$$

The shear stress in the VEM which is due entirely to beam deflections will be denoted as $\tau_W(X, T)$. Thus the total shear stress in the VEM is given by Eq. (3-37).

$$\tau(X, T) = \tau_V(X, T) + \tau_W(X, T) \quad (3-37)$$

The amount of energy actively dissipated per cycle of vibration will now be derived. It must be emphasized that although no control has been explicitly stated, the above analysis implicitly assumes that the shear stress is harmonic and in phase with the vibration. The work done on the viscoelastic layer is given by Eq. (3-38).

$$\frac{du}{dV_{ol}} = \int_{t_1}^{t_2} \tau \dot{\gamma} dt \quad (3-38)$$

Assume harmonic motion with $\tau(t) = \tau_0 \cos(\omega t)$ and a material with a complex shear compliance $C = C_1 + jC_2$. Then the work done on the material is given by Eq. (3-39).

$$\frac{du}{dV_{ol}} = -\omega \int_{t_1}^{t_2} \tau_0^2 C_1 \cos(\omega t) \sin(\omega t) dt - \omega \int_{t_1}^{t_2} \tau_0^2 C_2 \cos^2(\omega t) dt \quad (3-39)$$

Let the limits of integration be one period of oscillation (i.e. 0 to $2\pi/\omega$) to find the energy storage and dissipation per cycle. The first term of Eq. (3-39) is zero, and represents the elastic, recoverable work done during the cycle. The second term is given by:

$$\frac{du_{dis}}{dV_{ol}} = -\tau_0^2 C_2 \pi \quad (3-40)$$

This is the energy dissipated per cycle. Rewritten in terms of shear modulus parameters it becomes:

$$\frac{du_{dis}}{dV_{ol}} = \frac{\tau_0^2 g_2 \pi}{|g|^2} \quad (3-41)$$

The energy is nondimensionalized using Eq. (3-42).

$$U = \frac{ul}{E_3 l_3} \quad (3-42)$$

The total energy dissipated is found by integrating over the volume of the shear layer. Substituting appropriate nondimensional parameters this becomes:

$$U = \frac{\pi G_2}{rA|G|^2} \int_0^1 \tau^2 dX \quad (3-43)$$

Making use of Eqs. (3-35) and (3-37) yields:

$$U = \frac{\pi G_2}{rA|G|^2} \int_0^1 \left[\tau_w + VA\sqrt{|G|}f(X) \right]^2 dX \quad (3-44)$$

Equation (3-44) shows that the amount of energy dissipated per cycle can be modulated actively.

In addition to internal dissipation, the active stresses appear in the boundary conditions. With the constraining layer fixed to the tip mass and left free at the root, the

boundary conditions (2-4), (3-28) and (3-29) contain active terms. Eq. (2-4) shows the normal stress in the constraining layer acts as a discrete moment at the beam tip. Since the tip may experience angular displacements, this moment can do work on the system. The active component of this boundary condition is found by evaluating Eq. (3-34) at $X = 1$.

$$\sigma(1, V) = VA \left(\frac{\cosh^2(\sqrt{|G|}) - \sinh^2(\sqrt{|G|})}{\cosh(\sqrt{|G|})} - 1 \right) \quad (3 - 45)$$

Making use of the identity:

$$\cosh^2(u) - \sinh^2(u) = 1 \quad (3 - 46)$$

yields:

$$\sigma(1, V) = VA \left(\frac{1}{\cosh(\sqrt{|G|})} - 1 \right) \quad (3 - 47)$$

The work done per cycle at this boundary is:

$$U(T) = V(T)A \left(\frac{1}{\cosh(\sqrt{|G|})} - 1 \right) \cdot \frac{\partial W(1, T)}{\partial X} \quad (3 - 48)$$

This result is similar to those found by Bailey.

Boundary conditions given by Eqs. (3-28) and (3-29) are both stress boundary conditions. Equation (3-28) requires the tensile stress in the constraining layer to be zero at the beam root. Equation (3-29) constrains the shear stress in the core to be zero at the tip. Since in each case the total stress is zero, there can be no resultant strain. Therefore neither boundary condition can do work on the system.

Section 4

Examination of Active Constrained Layer Damper Effectiveness

4.1 Experimental Evaluation of an Active Constrained Layer Damper

4.1.1 Material

The active constrained layer damper design was experimentally evaluated using $0.152 \text{ m} \times 3.81 \times 10^{-4} \text{ m} \times 0.0127 \text{ m}$ (6.0 inch \times 0.015 inch \times 0.5 inch) cantilever beams. Test articles were made of steel shim stock and fitted with a lead tip mass of 3.0 grams. The beam tip was also fitted with an Entran 0.5 gram piezoresistive linear accelerometer which was used as the sensor for the feedback control laws (cf. Figure 4-1).

Various constrained layer damper designs were tested. Viscoelastic layer thicknesses of $1.27 \times 10^{-4} \text{ m}$ and $2.54 \times 10^{-4} \text{ m}$ were tested in conjunction with PVF₂ constraining layers of $52 \times 10^{-6} \text{ m}$ and $110 \times 10^{-6} \text{ m}$. A total of 4 different ACLAD designs were tested, each with a different VEM/constraining layer configuration. In addition, 2 active dampers which did not incorporate a viscoelastic layer were also tested to evaluate damping of the PVF₂ layer alone. Finally a passive constrained layer damper which used a $2.54 \times 10^{-5} \text{ m}$ aluminum constraining layer and a $2.54 \times 10^{-4} \text{ m}$ viscoelastic layer was tested (cf. Table 4-1). The constrained layer dampers were constructed using a viscoelastic material which is commercially available from the 3M Company under the trade name 'Scotchdamp' damping tape, identification SJ2015X, Type 112. It is essentially a thick, double sided adhesive tape. The shear modulus and loss factor of these materials is temperature and frequency dependent. The final specifications of the test beams appear in Table 4-2. The properties for the shear modulus and loss factor of the viscoelastic layer used in calculations were taken for an ambient temperature of 75°F, and a frequency of 6 hz. A reduced frequency plot of its loss factor and shear modulus appears in Figure 4-2.

PVF₂ film will strain when an electric field is presented across its thickness. To facilitate this, a very thin coating of nickel and aluminum is deposited on the free

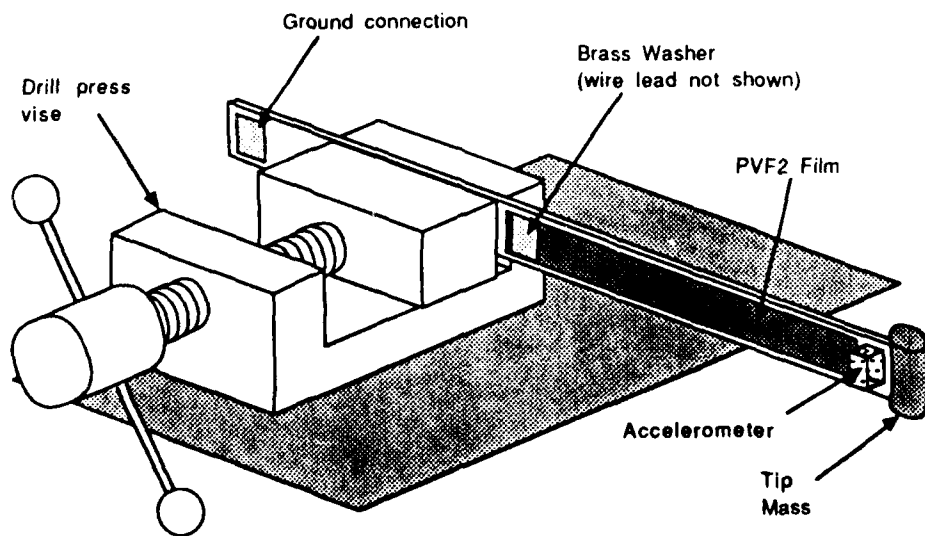


Figure 4-1. Active constrained layer damper test configuration.

Table 4-1. Constrained layer dampers tested on steel structure.

Constraining layer		VEM layer
Material	Thickness	Thickness
PVF ₂	52x10 ⁻⁶ m	1.27x10 ⁻⁴ m
PVF ₂	52x10 ⁻⁶ m	2.54x10 ⁻⁴ m
PVF ₂	52x10 ⁻⁶ m	none
PVF ₂	110x10 ⁻⁶ m	1.27x10 ⁻⁴ m
PVF ₂	110x10 ⁻⁶ m	2.54x10 ⁻⁴ m
PVF ₂	110x10 ⁻⁶ m	none
Aluminum	2.54x10 ⁻⁵ m	2.54x10 ⁻⁴ m

Table 4-2. Test article properties used in constrained layer damper tests.

Material	Steel
Length (m)	0.152
Width (m)	1.27x10 ⁻²
Thickness (m)	3.81x10 ⁻⁴
Tip mass (kg)	0.0035
Tip rotary inertia (kgm ²)	4.93x10 ⁻⁷
Modulus (Nm ⁻²)	210x10 ⁹
Density (kgm ⁻³)	7800
Shear modulus (Nm ⁻²)	2.1x10 ⁵
Loss tangent (η)	0.6

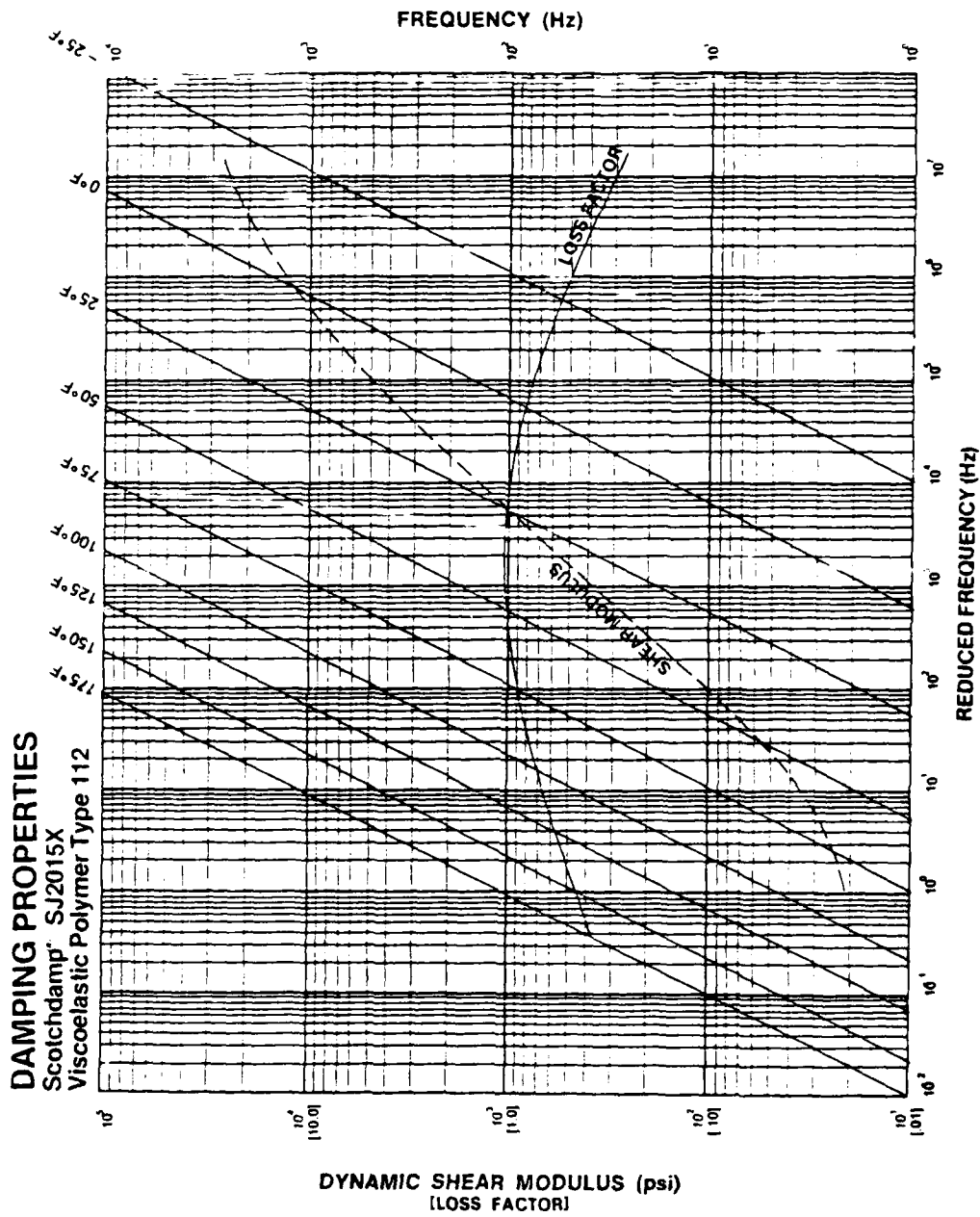


Figure 4-2. Reduced frequency plot of modulus and loss factor for Scotchdamp SJ015X, Type 112.

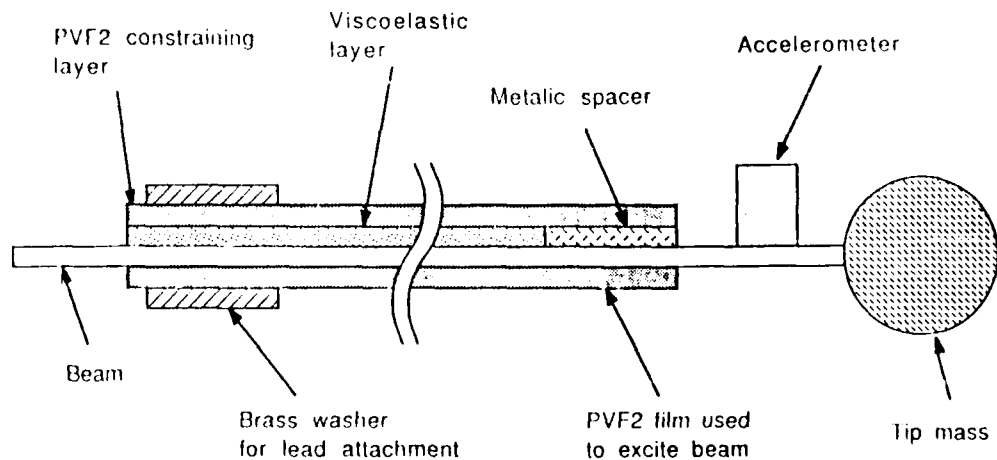


Figure 4-3. Schematic of typical active constrained layer damper test article.

surfaces by the manufacturer. A voltage presented across the faces is distributed by this conductor and results in a distributed electric field along the length of the film. A lead was attached to the free surface of the film by soldering a wire to a 0.01 m square brass washer, which was then adhered directly to the constraining layer using a conductive ink, Amicon C-931-40. Previous tests which did not use a viscoelastic layer used the beam structure as the second conductor. Since the PVF₂ is sensitive to an electric field and not a voltage, this method was sufficient. With the addition of the viscoelastic layer it was no longer efficient to use the beam as the second conductor. Such an increase in the conductor spacing would greatly reduce the electric field developed for a given voltage. For this reason it was desirable to distribute the voltage with the metalized coating directly. Figure 4-3 shows the final configuration schematically. It should be noted that the voltage to the side of the film which is not directly accessible is transmitted to the surface via the beam and a metallic spacer. This spacer was necessary to avoid sharp bends in the PVF₂ which can cause the metal plating to develop cracks.

4.1.2 Feedback Control Laws tested

Three different feedback control laws were tested on the ACLAD design. Two of these used the tip velocity of the beam as the controlling input. The control laws were proportional control, and the switching control developed by Bailey. They rely on the storage modulus of the viscoelastic layer to transmit stresses developed in the PVF₂ layer to the main structure. The presence of a loss modulus (viscous terms) is not directly exploited in this type of control law and it is assumed that its effects will be realized as increased passive damping.

The third control law was proportional control using position feedback. By implementing this algorithm, the amount of shear across the viscoelastic layer could be actively increased by straining the film out of phase with tip displacement. As a result, this control yields the greatest average strain rate across the shear layer. This control law maximizes the contribution of the loss modulus of the viscoelastic material to the damping of the beam, because the viscous forces are proportional to strain rate.

All of the control algorithms were realized using a Labtech 70 microcomputer running at a sampling frequency of 1000 hz.

4.1.3 Experimental Procedure

The dampers were tested by measuring the forced response to continuous sinusoidal excitation. The input to the system was supplied by a second piece of 52×10^{-6} m PVF₂ film laminated to the side of the beams without the damper. As discussed by Bailey and Burke [21], this configuration of the PVF₂ bonded directly to the structure develops a uniform bending moment within the structure. This bending moment distribution is the same as the distribution which would result from a discrete bending moment at the tip of the beam.

The first modal frequency of the test structures was approximately 6.5 hz. The structures were excited by a swept sine from 4.0 hz to 10.0 hz using a sweep rate of 0.05 hz/second. The voltage to the driving film was kept constant over this frequency range at 500 V p-p. A Zonic 6088 structural analyzer was used to measure the transfer function between the applied moment to the beam (via the driving film) and the tip acceleration. The analysis bandwidth was 4.0 hz to 9.0 hz. The damping was calculated using Eqs. (4-1) through (4-3) [22] where ω_a and ω_b are the peak frequencies in the real part of the transfer function (cf. Figure 4-4).

$$Q = \frac{\left(\frac{\omega_a}{\omega_b}\right)^2 + 1}{\left(\frac{\omega_a}{\omega_b}\right)^2 - 1} \quad (4-1)$$

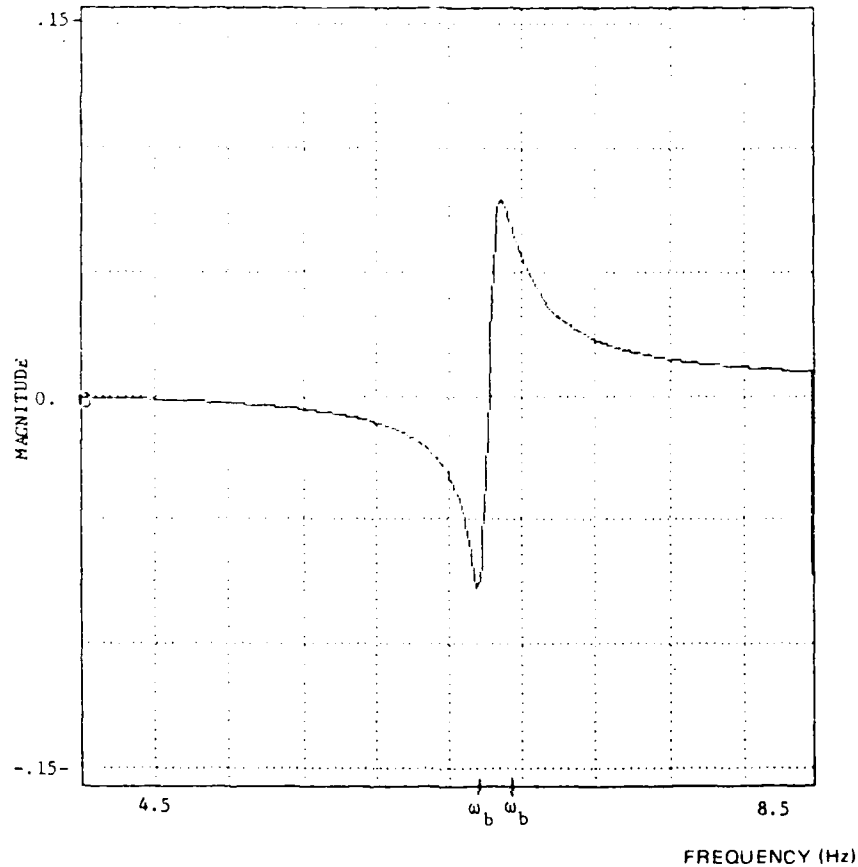


Figure 4-4. Real part of transfer function between beam excitation voltage and tip acceleration.

$$Q = \frac{1}{2\zeta} \quad (4-2)$$

$$\eta = 2\zeta \quad (4-3)$$

The equipment used in this study is shown schematically in Figure 4-5. (When using the position feedback law, the accelerometer signal was integrated twice before sampling.) A typical transfer function appears in Figure 4-6.

4.1.4 Experimental Results

The results of the damping tests for various feedback gains appear in Tables 4-3 through 4-9. The entries in the matrix are the effective loss factor of a structure with a given viscoelastic layer and constraining layer. All active control tests were performed at two different levels of control effort. For controllers using proportional control, the peak to peak control effort at resonance was adjusted until the desired level was reached.

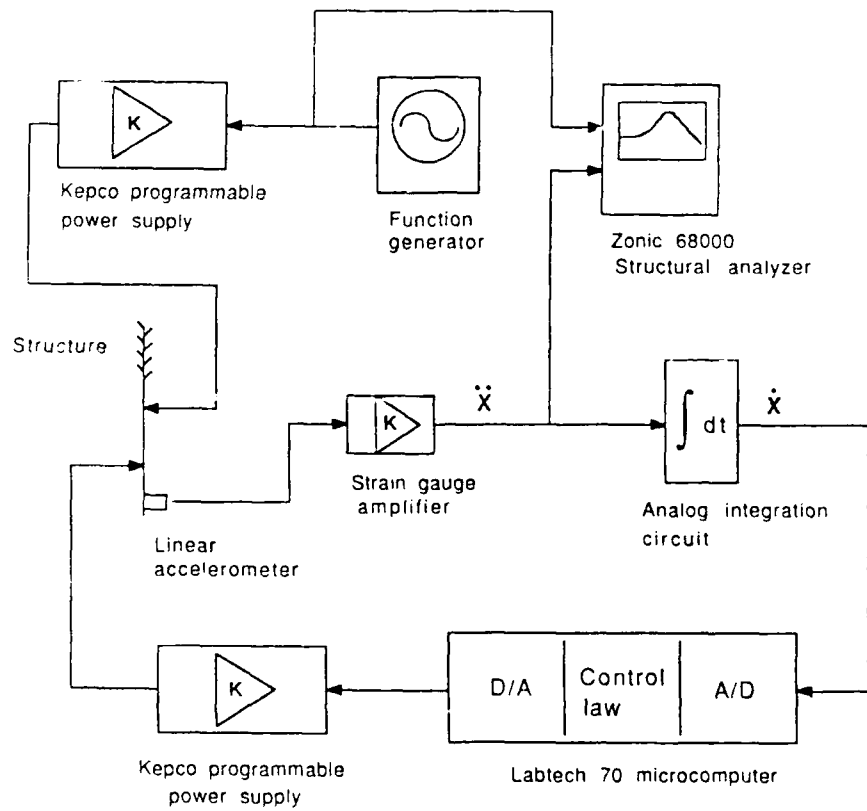


Figure 4-5. Instrumentation used in constrained layer damper tests.

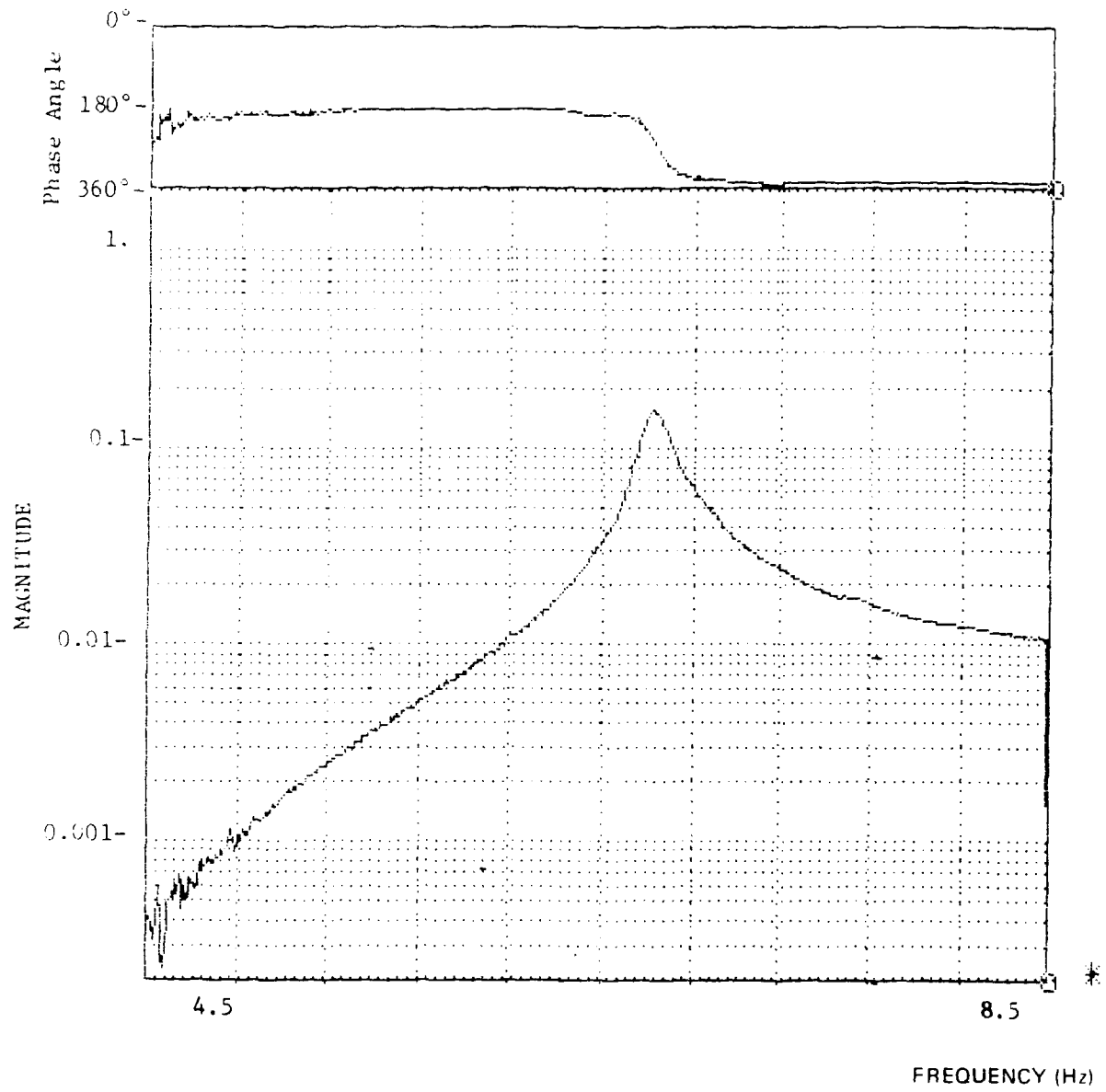


Figure 4-6. Typical transfer function between beam excitation voltage and tip acceleration.

Table 4-3. Constrained layer damper test results, uncontrolled.

Constraining layer thickness	VEM thickness		
	0	$1.27 \times 10^{-4} \text{m}$	$2.54 \times 10^{-4} \text{m}$
$52 \times 10^{-6} \text{m}$	0.0068	0.0075	0.0110
$110 \times 10^{-6} \text{m}$	0.0099	0.0094	0.0126

Off-resonance responses, therefore, experienced proportionally less control effort. The position feedback control law was not applicable for structures without a viscoelastic layer. A damper which used a 2.54×10^{-5} aluminum constraining layer and 2.54×10^{-4} shear layer had a loss factor $\eta = 0.0176$.

The results of the passive tests show dampers with thicker viscoelastic layers and stiffer (i.e. thicker) constraining layers added the most damping. The damper of 2.54×10^{-5} m viscoelastic and 110×10^{-6} m PVF₂ consistently added the most damping to the structure for all the control laws. The experiments using the switching control demonstrated the largest increase in damping for all damper configurations. The proportional control using position feedback was consistently the least effective control law. These results demonstrate that the maximum increase in damping due to active means is achieved by doing work on the system boundary and not by augmenting the amount of energy dissipated by the loss modulus of the viscoelastic layer. Although the baseline damping of the structure is increased with all of the feedback control laws tested, the most effective use of the PVF₂ actuator is to do work directly on the structure.

4.2 Shear Strain in the Viscoelastic Layer

In addition to the experiments described above, an analysis of the stresses induced in the viscoelastic layer of a constrained layer damper was performed. The active constrained layer damper and a passive design using a steel constraining layer were analyzed. The purpose of this analysis was to compare the magnitude of the stresses developed in the active and passive designs and thereby obtain an estimate of their relative effectiveness. A simply supported beam displaced in its first mode was studied. Two different

Table 4-4. Constrained layer damper test results, position feedback, 350 V p-p.

Constraining layer thickness	VEM thickness		
	0	$1.27 \times 10^{-4} \text{ m}$	$2.54 \times 10^{-4} \text{ m}$
$52 \times 10^{-6} \text{ m}$	—	0.0097	0.0144*
$110 \times 10^{-6} \text{ m}$	—	0.0094	0.0155

* 300 V p-p

Table 4-5. Constrained layer damper test results, velocity feedback, 350 V p-p.

Constraining layer thickness	VEM thickness		
	0	$1.27 \times 10^{-4} \text{ m}$	$2.54 \times 10^{-4} \text{ m}$
$52 \times 10^{-6} \text{ m}$	0.0098	0.0110	0.0183
$110 \times 10^{-6} \text{ m}$	0.0129 **	—	0.0189

** 300 V p-p

Table 4-6. Constrained layer damper test results, switching control, 350 V p-p.

Constraining layer thickness	VEM thickness		
	0	$1.27 \times 10^{-4} \text{ m}$	$2.54 \times 10^{-4} \text{ m}$
$52 \times 10^{-6} \text{ m}$	0.0098	0.0126	0.0184†
$110 \times 10^{-6} \text{ m}$	—	—	0.0192

† 300 V p-p

Table 4-7. Constrained layer damper test results, velocity feedback, 500 V p-p.

Constraining layer thickness	VEM thickness		
	0	$1.27 \times 10^{-4} \text{ m}$	$2.54 \times 10^{-4} \text{ m}$
$52 \times 10^{-6} \text{ m}$	0.0120	0.0170	0.0191
$110 \times 10^{-6} \text{ m}$	—	0.0181	0.0196

Table 4-8. Constrained layer damper test results, switching control, 500 V p-p.

Constraining layer thickness	VEM thickness		
	0	$1.27 \times 10^{-4} \text{ m}$	$2.54 \times 10^{-4} \text{ m}$
$52 \times 10^{-6} \text{ m}$	0.0142	0.0163	0.0193
$110 \times 10^{-6} \text{ m}$	0.0178†	0.0191†	0.0223

† 600 V p-p

Table 4-9. Constrained layer damper test results, position feedback, 700 V p-p.

Constraining layer thickness	VEM thickness		
	0	$1.27 \times 10^{-4} \text{ m}$	$2.54 \times 10^{-4} \text{ m}$
$52 \times 10^{-6} \text{ m}$	—	0.0104	0.0178
$110 \times 10^{-6} \text{ m}$	—	0.0122	0.0184

Table 4-10. Simulation parameters used in shear stress analysis for pinned- pinned beam.

Constraining layer material	Steel	PVF ₂
Constraining layer thickness (m)	1.1×10^{-4}	1.1×10^{-4}
Constraining layer modulus (Nm ⁻²)	2.1×10^{11}	2.0×10^9
Beam length (m)	0.292	0.292
Beam width (m)	0.0127	0.0127
Beam thickness	3.81×10^{-4}	3.81×10^{-4}
VEM modulus (Nm ⁻²)	2.1×10^5	2.1×10^5
VEM loss factor	0.6	0.6
VEM thickness (m)	2.54×10^{-4}	2.54×10^{-4}
Control voltage	—	1000
Midspan deflection (m)	0.0127	0.0127

configurations were analyzed, the first configuration had the constraining layer free at both ends. In the second configuration, the constraining layer was terminated such that there was no shear stress in the viscoelastic layer at one end and no tensile stress in the constraining layer at the other end. This is the constraining layer termination used on the experimental beams. It was assumed that the addition of the damping layers did not significantly alter the mode shape. The values of the parameters used in the simulations appear in Table 4-10. The stresses were calculated by solving Eq. (3-26). The mode shape of the first mode of an undamped, simply supported beam was used. It is given in Eq. (4-4). The variables W and X have been nondimensionalized using the relationships given in Table 2-3.

$$W = \sin(X\pi) \quad (4 - 4)$$

A midspan deflection of 0.0127 m and a control amplitude of 1000 volts were used.

The shear stress distributions for two ACLAD designs and analogous passive constrained layer dampers using a steel constraining layer are plotted in Figures 4-7 and 4-8.

The rate of energy dissipation per unit volume in a constrained layer damper is proportional to the square of the shear strain rate across the viscoelastic layer. For a given modal frequency the strain rate is proportional to the strain and therefore proportional to the shear stress which is plotted. The more shear stress a given constraining layer

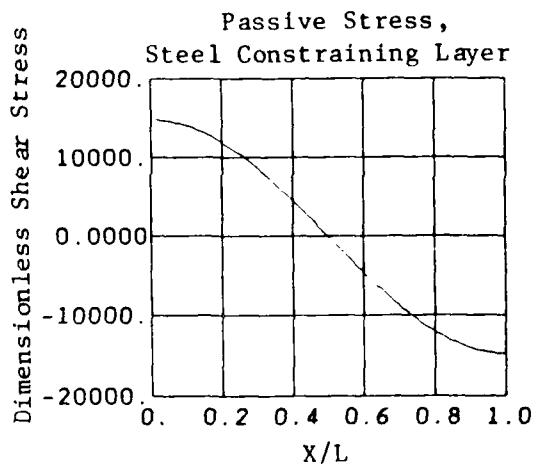
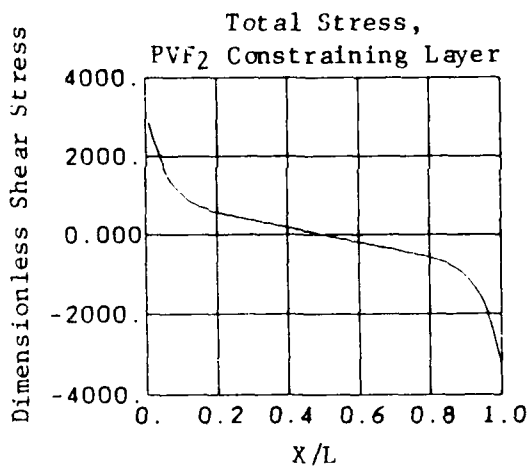
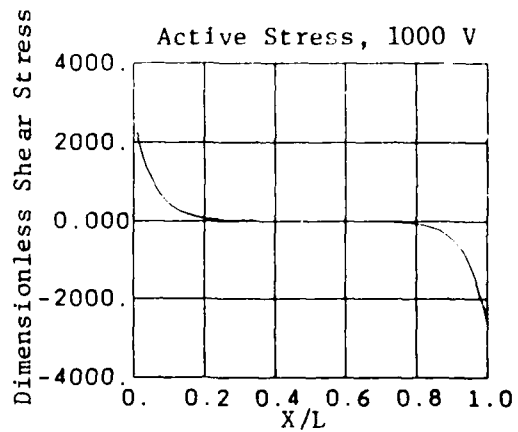
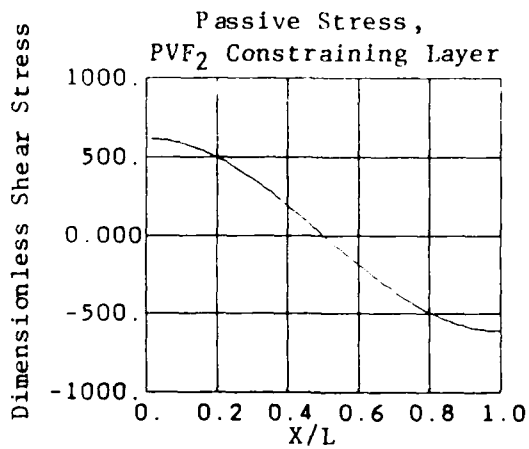


Figure 4-7. Shear stress distribution in the viscoelastic layer of an active constrained layer damper with constraining layer free at both ends.

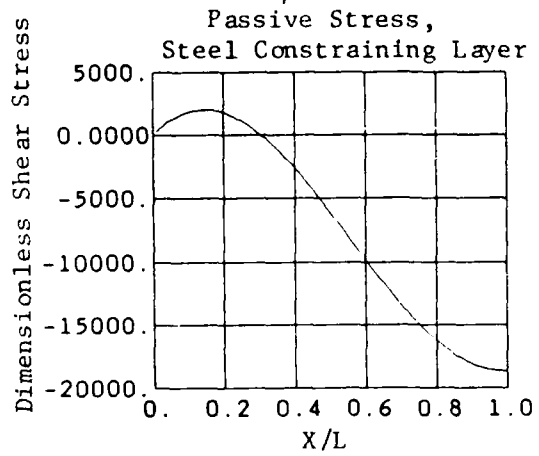
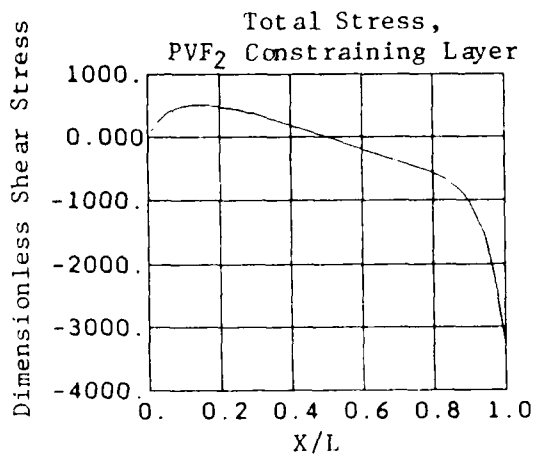
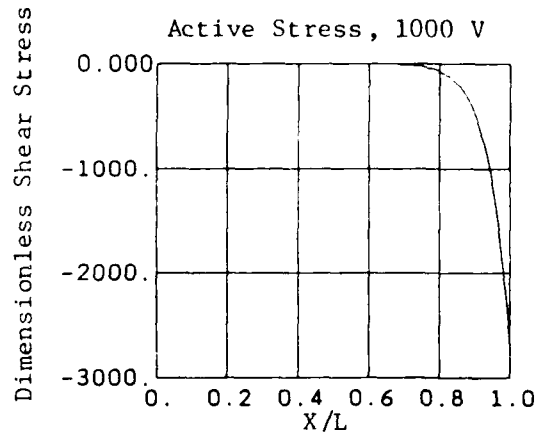
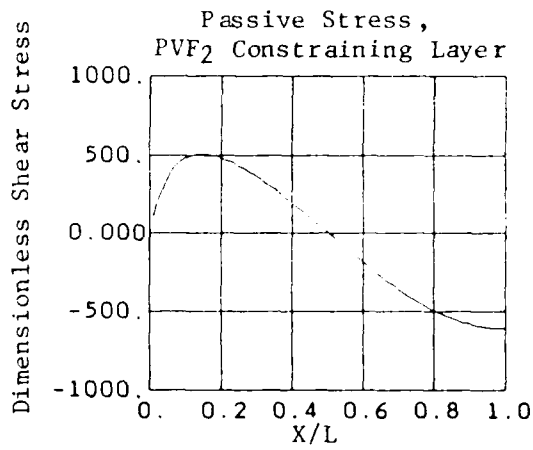


Figure 4-8. Shear stress distribution in the viscoelastic layer of an active constrained layer damper with constraining layer clamped at one end.

can cause in the damping layer, the more damping it will add. Thus Figures 4-7 and 4-8 can be used to evaluate the relative effectiveness of the constrained layer dampers. It is obvious from these figures that the passive dampers which use a steel constraining layer are much more effective at inducing shear in the viscoelastic layer than are the designs which use PVF₂. The reason for this is the superior stiffness of steel over PVF₂. Although the active component in the PVF₂ response is dominant, and has a peak value on the order of 20% of the peak value of the steel design, its low stiffness severely limits the overall effectiveness.

Section 5

Derivation of the Control Law for the PVF₂ Film Actuators

5.1 Introduction

In this section of the report the equations of motion for a cantilever beam with a tip mass will be derived where the end of the beam is rigidly fixed to a freely rotating cylindrical base. Hamilton's principle will be used to derive the equations and the direct method will be used as a check. The Lyapunov stability criteria will then be used to derive a control law for the PVF₂ actuators.

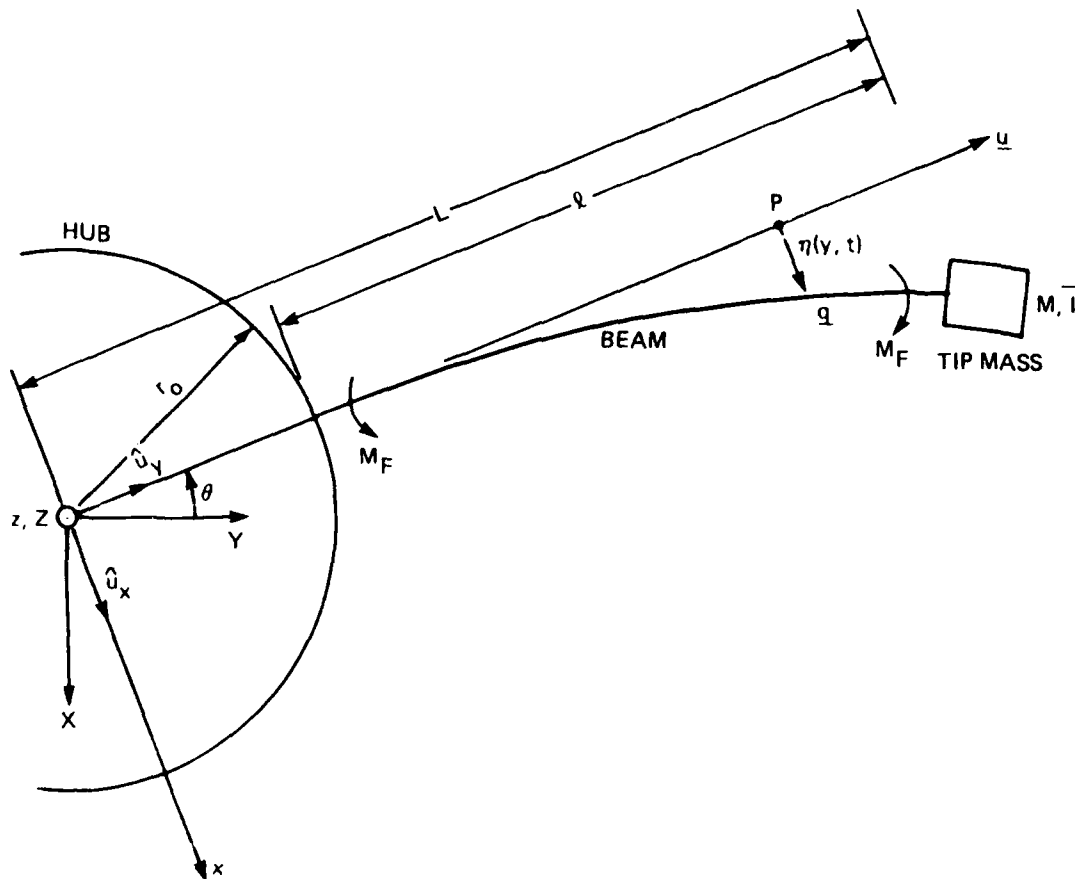
5.2 Hamilton's Principle

Figure 5-1 is a plan view of the cantilever and hub. An inertial reference frame, designated as the XYZ frame, is attached at the hub pivot. A rotating reference frame, designated as the xyz frame, is fixed to the hub and oriented such that the y axis coincides with the connection point of the cantilever. The angle of rotation of the xyz frame is given as ϕ . The elastic deformation of the cantilever, $\eta(y,t)$, is measured perpendicular from any arbitrary point p on the y-axis of the rotating xyz frame to point q on the cantilever. $\eta(y,t)$ and ϕ together constitute a complete set of generalized coordinates that completely specify the configuration of the system at any instant in time. No geometric constraint relations exist between ϕ and $\eta(y,t)$ (ϕ can be arbitrarily varied through any angle while keeping $\eta(y,t)$ fixed, and vice versa); therefore, the chosen coordinates are independent and represent the number of independent degrees of freedom of the system. The tip mass and inertia are designated as M and \bar{I} .

Hamilton's principle is stated as follows:

$$\int_{t_1}^{t_2} (\delta L + \Xi_i \delta \xi_i) dt = 0 \quad (5-1)$$

where $L = T^* - V$ is the Lagrangian; $T^* = T_b^* + T_M^* + T_h^*$ is the total kinetic energy;



- EI = beam stiffness
- T_0 = hub torque
- ϕ = hub angle
- M_f = moment due to film
- r_0 = hub radius
- l = length of beam
- m = mass per unit length
- M = tip mass
- I = tip inertia
- $\eta(y, t)$ = deflection of beam measured from xyz coordinate system

Figure 5-1. Cantilever and hub.

T_b^* is the kinetic energy of the beam; T_M^* is the kinetic energy of the tip mass; T_h^* is the kinetic energy of the hub; V is the the elastic strain energy stored in the cantilever and the work of conservative forces; and Ξ_i is the nonconservative generalized forces not accounted for in V .

The analysis begins by first locating point q in inertial space. From figure 5-1 this is given by:

$$\vec{R}_q = y\hat{u}_y + \eta\hat{u}_x \quad (5-2)$$

This displacement vector is then differentiated with respect to time to get the velocity of point q in inertial space.

$$\vec{V}_q = \frac{d\vec{R}_q}{dt} = y \frac{d\hat{u}_y}{dt} + \dot{\eta}\hat{u}_x + \eta \frac{d\hat{u}_x}{dt} \quad (5-3)$$

From definitions given in dynamics, the derivative with respect to time of a unit vector contained within a rotating frame of reference is equal to the cross product of the angular velocity of that frame in inertial space and the unit vector. The angular velocity of the xyz frame in inertial space is given as:

$$\vec{\Omega}_{xyz} = \dot{\phi}\hat{u}_z \quad (5-4)$$

(note that the unit vectors in the z direction for both the inertial frame and rotating frame are equal, i.e. $\hat{u}_z = \hat{u}_z$); therefore, we evaluate the time derivatives of the unit vectors as follows:

$$\frac{d\hat{u}_y}{dt} = \vec{\Omega}_{xyz} \times \hat{u}_y = \dot{\phi}(\hat{u}_z \times \hat{u}_y) = -\dot{\phi}\hat{u}_x \quad (5-5)$$

$$\frac{d\hat{u}_x}{dt} = \vec{\Omega}_{xyz} \times \hat{u}_x = \dot{\phi}(\hat{u}_z \times \hat{u}_x) = \dot{\phi}\hat{u}_y \quad (5-6)$$

$$\vec{V}_q = (\dot{\eta} - y\dot{\phi})\hat{u}_x + \eta\dot{\phi}\hat{u}_y \quad (5-7)$$

The velocity of the tip mass is found from Eq. (5-7) by substituting in $y=L$ and evaluating η at L .

$$\vec{V}_M = [(\dot{\eta} - L\dot{\phi})\hat{u}_x + \eta\dot{\phi}\hat{u}_y]_{y=L} \quad (5-8)$$

The angular velocity in inertial space of the tip mass is

$$\vec{\omega}_M = \left(\dot{\phi} - \frac{\partial^2 \eta}{\partial y \partial t}\right)_{y=L} \hat{u}_z \quad (5-9)$$

The angular velocity of the hub in inertial space is

$$\vec{\omega}_h = \dot{\phi}\hat{u}_z \quad (5-10)$$

Next, the kinetic energies of the system are evaluated. For the beam:

$$T_b^* = \frac{1}{2} m \int_{r_0}^L \vec{V}_q \cdot \vec{V}_q dy \quad (5-11)$$

where the rotational inertia of the beam has been neglected and m =mass/ unit length.

Carrying through the algebra gives the following expression for the kinetic energy of the beam:

$$T_b^* = \frac{m}{6}(L^3 - r_0^3)\dot{\phi}^2 + \frac{m}{2} \int_{r_0}^L (\dot{\eta}^2 - 2y\dot{\phi}\dot{\eta} + \eta^2\dot{\phi}^2) dy \quad (5-12)$$

The kinetic energy of the tip mass is given as follows:

$$T_M^* = \frac{1}{2} M \vec{V}_M \cdot \vec{V}_M + \frac{1}{2} \bar{I} \vec{\omega}_M \cdot \vec{\omega}_M \quad (5-13)$$

where M =tip mass, and \bar{I} =tip inertial about the c.g. of the mass. Substituting (5-8) and (5-9) into (5-13) and reducing gives:

$$T_M^* = \frac{1}{2} M [\dot{\eta}^2 - 2\dot{\eta}\dot{\phi}L + L^2\dot{\phi}^2 + \eta^2\dot{\phi}^2]_{y=L} + \frac{1}{2} \bar{I} (\dot{\phi}^2 - 2\dot{\phi} \frac{\partial^2 \eta}{\partial y \partial t} + (\frac{\partial^2 \eta}{\partial y \partial t})^2)_{y=L} \quad (5-14)$$

The kinetic energy of the hub is

$$T_h^* = \frac{1}{2} I_h \dot{\phi}^2 \quad (5-15)$$

where I_h =inertia of hub.

Next, an expression for the potential energy of the cantilever is derived. We begin with the definition of strain energy assuming that only the normal ϵ_{yy} strains are present, i.e., there are no shear strains as in Timoshenko beam theory. Other than the strain energy, no other conservative forces do work on the system. Therefore, the total potential is given as

$$V = \frac{1}{2} \int_{V_b} E_b \epsilon_{yy_b} dV_b + \frac{1}{2} \int_{V_f} E_f \epsilon_{yy_f} dV_f \quad (5-16)$$

where

$$\epsilon_{yy_b} = \frac{\partial v_b}{\partial y} \quad (5-17)$$

$$\epsilon_{yy_f} = \frac{\partial v_f}{\partial y} + \epsilon_0 \quad (5-18)$$

E_b = Youngs Modulus of beam

E_f = Youngs Modulus of film.

Note that an initial prescribed prestrain ϵ_0 (prescribed stresses and strains are not subject to variation) has been added to the elastic strain of the film. It is assumed in Eq. (5-18) that the total strain of the film is a linear combination of the elastic strain caused by bending and the strain induced by the piezoelectric effect.

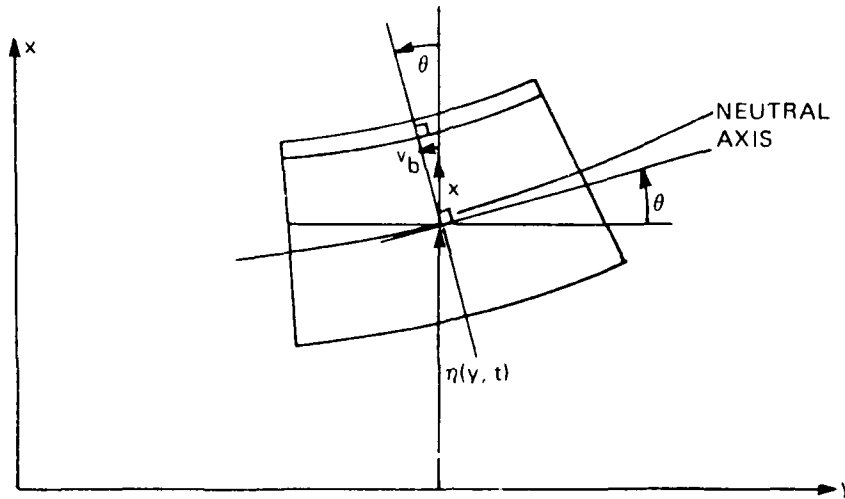


Figure 5-2. Deflection of differential beam element.

The next assumption is that cross-sectional planes remain plane as the cantilever deforms (see Figure 5-2). This assumption gives the following geometric relation for the axial displacement, v , in the y direction:

$$v_b = v_f = -x\theta(y) \quad (5-19)$$

The previous assumption of no shear relates the angular rotation of the planes, $\theta(y)$, to the equation for the deflection curve of the neutral axis of the beam, $\eta(y, t)$, viz.

$$\tan \theta = \frac{\partial \eta}{\partial y} \quad (5-20)$$

assuming small rotations gives:

$$\tan \theta \sim \theta \quad (5-21)$$

Substituting displacement assumptions (5-19), (5-20), (5-21) into the normal strains for the beam and film, (5-17) and (5-17), gives:

$$\epsilon_{yy_b} = -x \frac{\partial \theta}{\partial y} = -x \frac{\partial^2 \eta}{\partial y^2} \quad (5-22)$$

$$\epsilon_{yy_f} = -x \frac{\partial^2 \eta}{\partial y^2} + \epsilon_0 \quad (5-23)$$

Substituting (5-22) and (5-23) into (5-16) gives the following expression for the strain energy:

$$V = \frac{1}{2} \int_{V_b} E_b x^2 \left(\frac{\partial^2 \eta}{\partial y^2} \right)^2 dV_b + \frac{1}{2} \int_{V_f} E_f \left(-x \frac{\partial^2 \eta}{\partial y^2} + \epsilon_0 \right)^2 dV_f \quad (5-24)$$

With expressions for T^* and an expression for V , the Lagrangian is evaluated then both $\eta(y, t)$ and ϕ are varied. Integration by parts follows, both in time and in space, until the independent variational variables are free from extraneous derivatives. During the integration by parts, the geometric boundary conditions are observed at $y = r_0$: $\eta(0, t) = 0$ and $\frac{\partial \eta}{\partial y} |_{y=r_0} = 0$, such that $\delta \eta(0, t) = 0$ and $\frac{\partial \delta \eta}{\partial y} |_{y=r_0} = 0$, and the restriction on Hamilton's principle, namely $\delta t_1 = 0$ and $\delta t_2 = 0$.

At the free end of the beam at $y=L$, note that both the angle $\frac{\partial \eta}{\partial y} |_{y=L}$ and displacement, $\eta(L, t)$ are free to vary; consequently, Hamilton's principle provides the boundary conditions at $y=L$ in the form of force and moment equilibrium between the tip mass and reactions in the beam. After collecting terms, the algebraic expressions multiplying each independent variational variable are equated to zero thus providing two equations of motion: one for the beam from the $\delta \eta(y, t)$ term, and one for the beam and hub combination from the $\delta \phi$ term.

The variations on the kinetic energy are straightforward; however, the potential energy term requires some explanation.

Varying the potential energy term, Eq. (5-24) gives:

$$\delta V = \int_{r_0}^L (E_b I_b \frac{\partial^2 \eta}{\partial y^2} \frac{\partial^2}{\partial y^2} (\delta \eta)) dy + \int_{V_f} E_f (-x \frac{\partial^2 \eta}{\partial y^2} + \epsilon_0) (-x \frac{\partial^2}{\partial y^2} (\delta \eta)) dV_f \quad (5-25)$$

where

$$I_b = \int_{A_b} x^2 dA = \text{area moment of inertia of beam about neutral axis} \quad (5-26)$$

and

$$\delta \epsilon_0 = 0 \quad (\text{prescribed prestrain}) \quad (5-27)$$

Define

$$\sigma_0 = E_f \epsilon_0 = \text{prestress due to film} \quad (5-28)$$

$$M_f = \int_{A_f} \sigma_0 x dA = \text{moment induced by film} \quad (5-29)$$

$$I_f = \int_{A_f} x^2 dA = \text{area moment of film about neutral axis} \quad (5-30)$$

$$EI = E_b I_b + E_f I_f = \text{composite stiffness} \quad (5-31)$$

Note that the area moments of inertia above are computed about the neutral axis of the composite beam. To find the neutral axis, the following formula may be employed at any section of the beam:

$$\int_A \sigma_{yy} dA = 0 \quad (5-32)$$

This equation simply states that the sum of the normal stresses over a cross section of the beam is zero. This condition must be true to preserve equilibrium because no external surface tractions are applied normal to the cross section of the beam at the boundaries, $y = L$ and $y = 0$.*

Substituting definitions (5-28), (5-29), (5-30), and (5-31) into (5-25) gives the following expression for the variation of the potential energy.

$$\delta V = \int_{r_0}^L EI \frac{\partial^2 \eta}{\partial y^2} \frac{\partial^2}{\partial y^2} (\delta \eta) dy - \int_{r_0}^L M_f \frac{\partial^2}{\partial y^2} (\delta \eta) dy \quad (5-33)$$

The next step is to determine the work done by those forces not accounted for in the potential energy expression (5-24). From the definition of the external work done by generalized forces:

$$\delta W = \sum_{i=1}^n \Xi_i \delta \xi \quad (5-34)$$

Varying the angular displacement of the hub gives the work done by the torque acting about the z-axis of the hub, viz.

$$\delta W = T_0 \delta \phi \quad (5-35)$$

The work due to the film was already accounted for in the expression for V , Eq. (5-24) and therefore is not included.

Carrying through with the algebra the following system of equations is derived:

$$\begin{aligned} \delta \eta(y, t) \quad \rightarrow \\ m \ddot{\eta} + EI \frac{\partial^4 \eta}{\partial y^4} - m \eta \dot{\phi}^2 - m y \ddot{\phi} = \frac{\partial^2 M_f}{\partial y^2} \end{aligned} \quad (5-36)$$

$$\begin{aligned} \delta \eta(L, t) \quad \rightarrow \\ EI \frac{\partial^3 \eta}{\partial y^3} - M \ddot{\eta} + M \ddot{\phi} L + M \eta \dot{\phi}^2 = \frac{\partial M_f}{\partial y} \end{aligned} \quad (5-37)$$

$$\begin{aligned} \frac{\partial}{\partial y} (\delta \eta(L, t)) \quad \rightarrow \\ - \bar{I} (\ddot{\phi} - \frac{\partial^3 \eta}{\partial t^2 \partial y}) + EI \frac{\partial^2 \eta}{\partial y^2} = M_f \end{aligned} \quad (5-38)$$

* Because the bending stiffness of the film is small compared to that of the beam, the composite stiffness can be accurately approximated by neglecting $E_f I_f$. With this approximation, the neutral axis is easily evaluated at the midplane of the beam.

$\delta\phi \rightarrow$

$$\begin{aligned} & \left(\frac{m}{3}(L^3 - r_0^3) + I_h\right)\ddot{\phi} + \int_{r_0}^L m(2\eta\dot{\eta}\dot{\phi} + \eta^2\ddot{\phi} - y\ddot{\eta})dy \\ & (ML\ddot{\eta} - ML^2\ddot{\phi} - 2\eta\dot{\eta}\dot{\phi}M - (M\eta^2 + \bar{I})\ddot{\phi} + \\ & \bar{I}\frac{\partial^3\eta}{\partial t^2\partial y})_{y=L} = T_0 \end{aligned} \quad (5-39)$$

The next step is to linearize the above equations by neglecting the following nonlinear products: $\ddot{\phi}\eta^2$; $\dot{\eta}\eta\dot{\phi}$; $\eta\dot{\phi}^2$; and η^2 .

The linearized PDE for the beam is

$$m\ddot{\eta} + EI\frac{\partial^4\eta}{\partial y^4} - m\eta\ddot{\phi} = \frac{\partial^2 M_f}{\partial y^2} \quad (5-40)$$

The linearized boundary conditions at $y=L$ are

$$EI\frac{\partial^3\eta}{\partial y^3} - M\ddot{\eta} + M\ddot{\phi}L = \frac{\partial M_f}{\partial y} \quad (5-41)$$

$$-\bar{I}(\ddot{\phi} - \frac{\partial^3\eta}{\partial t^2\partial y}) + EI\frac{\partial^2\eta}{\partial y^2} = M_f \quad (5-42)$$

The linearized equation for the beam and hub is

$$\left(\frac{m}{3}(L^3 - r_0^3) + I_h + ML^2 + \bar{I}\right)\ddot{\phi} - \int_{r_0}^L m\eta\ddot{\eta}dy - (ML\ddot{\eta} + \bar{I}\frac{\partial^3\eta}{\partial t^2\partial y})_{y=L} = T_0 \quad (5-43)$$

Before proceeding with the Lyapunov analysis, the equations of motion will be nondimensionalized by substituting the following definitions:

$$\begin{aligned} w &= \frac{\eta}{\ell} \\ Y &= \frac{(y - r_0)}{\ell} \\ \zeta &= \frac{r_0}{\ell} \\ \tau &= t\sqrt{\frac{EI}{m\ell^4}} \\ M_f &= \frac{M_f\ell}{EI} \\ T_0 &= \frac{T_0\ell}{EI} \end{aligned}$$

$$\begin{aligned}
M &= \frac{M}{m\ell} \\
I &= \frac{I}{m\ell^3} \\
I_h &= \frac{I_h}{m\ell^3} \\
I_t &= \left[\frac{1}{3} + \zeta(\zeta + 1) + I_h + I + M(\zeta + 1)^2 \right]
\end{aligned}$$

The equations in nondimensional form become:

Beam

$$\frac{\partial^2 w}{\partial \tau^2} + \frac{\partial^4 w}{\partial Y^4} - (Y + \zeta) \frac{\partial^2 \phi}{\partial \tau^2} = \frac{\partial^2 M_f}{\partial Y^2} \quad (5-44)$$

Hub

$$I_t \frac{\partial^2 \phi}{\partial \tau^2} - \int_0^1 (Y + \zeta) \frac{\partial^2 w}{\partial \tau^2} dY - M(1 + \zeta) \frac{\partial^2 w}{\partial \tau^2} - I \frac{\partial^3 w}{\partial Y \partial \tau^2} = T_0 \quad (5-45)$$

The natural boundary conditions at $Y=1$ are

$$\frac{\partial^3 w}{\partial Y^3} - M \frac{\partial^2 w}{\partial \tau^2} + M(1 + \zeta) \frac{\partial^2 \phi}{\partial \tau^2} = \frac{\partial M_f}{\partial Y} \quad (5-46)$$

$$I \left[\frac{\partial^3 w}{\partial \tau^2 \partial Y} - \frac{\partial^2 \phi}{\partial \tau^2} \right] + \frac{\partial^2 w}{\partial Y^2} = M_f \quad (5-47)$$

It is apparent from Eq. (5-44) to Eq. (5-47) that coupling exists between the lateral beam deflection and hub motion as given by w and ϕ , respectively. In general, when the PVF₂ film is used as an actuator it induces a spatially varying strain field in the beam and the "control effort" appears as a Laplacian on the right hand side of Eq. (5-44). This form of the control input may be exploited to yield a number of different manifestations of load input to the structure. In the absence of hub motion, $\phi(\tau)=0$, the system described by Eq. (5-44) reduces to the form described in References [3] and [21] which develop design criteria for spatially "shaping" the induced strain field to allow effective inputs of forces, moments, et cetera.

For the case considered here in which the applied moment is uniformly distributed along the beam the Laplacian of the moment distribution is identically zero. The result is that the applied moment only appears as a natural boundary condition described by Eq. (5-47). Here the result of the applied moment is to create a lateral deflection as given by the beam curvature term in Eq. (5-47) as well as inducing both lateral deflection

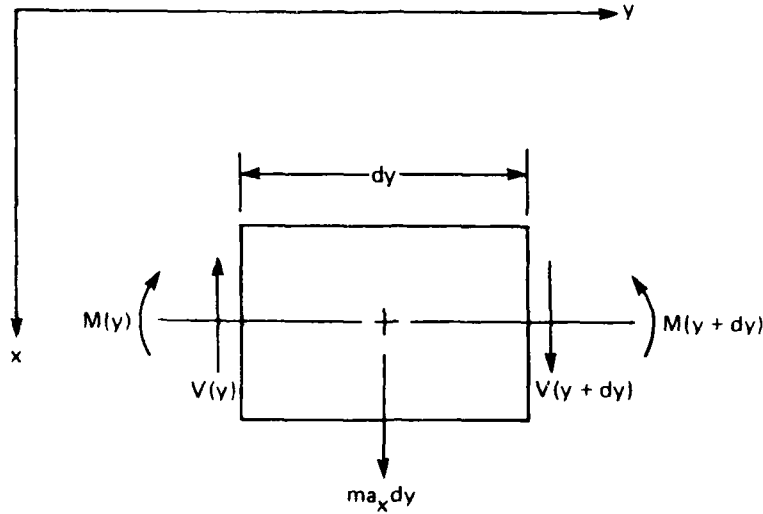


Figure 5-3. Force balance on differential element at point q.

dynamics and hub motion through an inertial coupling term.* The transient dynamics of the structure are therefore driven by both the time varying moment M_f and the inertia of the structure subject to the natural and geometric boundary conditions outlined earlier. The steady state deflection of the cantilevered beam is uniquely determined solely by the applied moment distribution and is totally independent of the steady state hub angle, ϕ .

5.3 Direct Method

In this section, the equations of motion previously derived using Hamilton's principle will be verified using the direct method of analysis.

First, the acceleration of point q on the beam is determined by differentiating with respect to time the expression for \vec{V}_q . Recalling that the unit vectors must also be differentiated, the following expression for acceleration results:

$$\vec{a}_q = (-y\ddot{\phi} + \ddot{\eta} - \eta\dot{\phi}^2)\hat{u}_x + (\eta\ddot{\phi} - y\dot{\phi}^2 + 2\dot{\eta}\dot{\phi})\hat{u}_y \quad (5 - 48)$$

With this expression for acceleration, $\vec{F} = m\vec{a}_q$ is applied to a differential element at point q (see Figure 5-3).**

$$\downarrow + \sum F_x = ma_x dy \quad (5 - 49)$$

*Note: It is assumed that there is no external hub torque as represented by T_0 .

**The downarrow indicates forces are positive along the x axis as shown in Figure 5-3.

$$\frac{\partial V}{\partial y} = m(\ddot{\eta} - y\ddot{\phi} - \eta\dot{\phi}^2) \quad (5-50)$$

Summing moments (clockwise positive) about the left hand end of the differential element relates the shear force in the beam to the moment (The inertial force acting at the c.g. of the differential element and the rotational inertial of the element have been neglected):

$$\sum M = 0 = \frac{\partial M(y)}{\partial y} - V \quad (5-51)$$

$$\frac{\partial M(y)}{\partial y} = V \quad (5-52)$$

substituting Eq. (5-52) into Eq. (5-50) gives:

$$\frac{\partial^2 M}{\partial y^2} = m(\ddot{\eta} - y\ddot{\phi} - \eta\dot{\phi}^2) \quad (5-53)$$

$$M(y) = -EI \frac{\partial^2 \eta}{\partial x^2} + M_f \quad (5-54)$$

$$\frac{\partial^2}{\partial y^2} [EI \frac{\partial^2 \eta}{\partial y^2}] + m\ddot{\eta} - my\ddot{\phi} - m\eta\dot{\phi}^2 = \frac{\partial^2 M_f}{\partial y^2} \quad (5-55)$$

Eq. (5-55) matches exactly with the previously derived result Eq. (5-36).

The second equation of motion is found by summing moments about the z-axis of the hub (see Figure 5-4). Summing moments (counterclockwise positive) about the z-axis gives (In this case it is necessary to define positive moments with respect to the coordinate system chosen because of the presence of inertial forces):

$$(T_0 + M_f - M_f)\hat{u}_z = \int_{r_0}^L \vec{R}_q \times m\vec{a}_q dy + \bar{I}(\ddot{\phi} - \frac{\partial^3 \eta}{\partial t^2 \partial y})_{y=L} \hat{u}_z + I_h \ddot{\phi} \hat{u}_z + (\vec{R}_M \times M\vec{a}_M)_{y=L} \quad (5-56)$$

where

$$\vec{R}_q = y\hat{u}_y + \eta\hat{u}_x \quad (5-57)$$

and

$$\vec{R}_M = \vec{R}_q (y=L) \quad (5-58)$$

Eq. (5-57) and Eq. (5-58) are substituted into Eq. (5-56) giving

$$\begin{aligned} T_0 \hat{u}_z = & \int_{r_0}^L (y\hat{u}_y + \eta\hat{u}_x) \times [(\ddot{\eta} - y\ddot{\phi} - \eta\dot{\phi}^2)\hat{u}_x + (\eta\ddot{\phi} - y\dot{\phi}^2 + 2\dot{\eta}\dot{\phi})\hat{u}_y] m dy \\ & + I_h \ddot{\phi} \hat{u}_z + \bar{I}(\ddot{\phi} - \frac{\partial^3 \eta}{\partial t^2 \partial y})_{y=L} \hat{u}_z + (L\hat{u}_y + \eta\hat{u}_x)_{y=L} \times [(\ddot{\eta} - L\ddot{\phi} - \eta\dot{\phi}^2)_{y=L} \hat{u}_x + \\ & (\eta\ddot{\phi} - L\dot{\phi}^2 + 2\dot{\eta}\dot{\phi})_{y=L} \hat{u}_y] M \end{aligned} \quad (5-59)$$

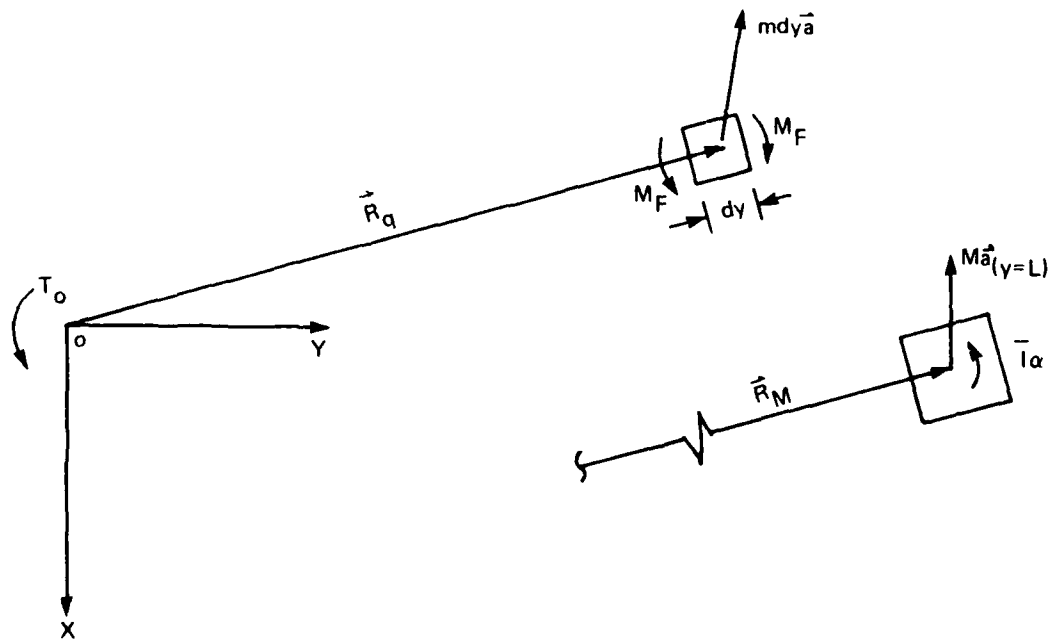


Figure 5-4. Summing moments about z-axis of hub.

Carrying out the cross products gives:

$$\begin{aligned}
 T_0 &= \int_{r_0}^L (y^2 \ddot{\phi} - y \ddot{\eta} + \eta^2 \ddot{\phi} + 2\eta \dot{\eta} \dot{\phi}) m \, dy + (I_h + \bar{I} + ML^2) \ddot{\phi} + \\
 &\quad M(\eta^2 \ddot{\phi} + 2\eta \dot{\eta} \dot{\phi} - L \ddot{\eta})_{y=L} - \bar{I} \frac{\partial^3 \eta}{\partial t^2 \partial y} \\
 &= \left[\int_{r_0}^L y^2 m \, dy + I_h + ML^2 + \bar{I} \right] \ddot{\phi} - (ML \ddot{\eta} + \bar{I} \frac{\partial^3 \eta}{\partial t^2 \partial y})_{y=L} - \\
 &\quad \int_{r_0}^L y \ddot{\eta} m \, dy \tag{5-60}
 \end{aligned}$$

Eq. (5-60) for the hub and beam combination matches with the previously derived result, Eq. (5-39). The boundary conditions can also be derived from force and moment balances at the end of the beam. Now that the equations of motion have been confirmed, the next step is to use the Lyapunov stability criteria to generate a control law.

5.4 Lyapunov Stability Criteria

The nondimensionalized equations are used in the following Lyapunov energy functional:

$$\begin{aligned}
 F &= \frac{1}{2} \int_0^1 \left[\left(\frac{\partial^2 w}{\partial Y^2} \right)^2 + \left(\frac{\partial w}{\partial \tau} - (Y + \zeta) \frac{\partial \phi}{\partial \tau} \right)^2 \right] dY + \frac{1}{2} I_h \left(\frac{\partial \phi}{\partial \tau} \right)^2 + \\
 &\quad \frac{1}{2} M \left(\frac{\partial w}{\partial \tau} - (1 + \zeta) \frac{\partial \phi}{\partial \tau} \right)_{Y=1}^2 + \frac{1}{2} \left(\frac{\partial \phi}{\partial \tau} - \frac{\partial^2 w}{\partial Y \partial \tau} \right)_{Y=1}^2 \tag{5-61}
 \end{aligned}$$

The first term represents the nondimensionalized strain energy; the second term represents the nondimensionalized kinetic energy of the beam; the third term is the nondimensionalized kinetic energy of the hub; and the fourth and fifth terms are the kinetic energy of the tip mass. This energy functional is differentiated with respect to time, giving an expression representing the power in the system, then minimized through the terms multiplied by the moment due to the film, M_f , and hub torque, T_0 . Differentiating

and integrating the first term by parts twice gives:

$$\begin{aligned}
 \dot{F} = & \frac{\partial^2 w}{\partial Y^2} \frac{\partial^2 w}{\partial Y \partial \tau} \Big|_{Y=1} - \frac{\partial^3 w}{\partial Y^3} \frac{\partial w}{\partial \tau} \Big|_{Y=1} + \int_0^1 \left(\frac{\partial^4 w}{\partial Y^4} + \frac{\partial^2 w}{\partial \tau^2} \right) \frac{\partial w}{\partial \tau} dY + \\
 & \frac{\partial \phi}{\partial \tau} \frac{\partial^2 \phi}{\partial \tau^2} (l_h + M(1 + \zeta)^2 + l + \int_0^1 (Y + \zeta)^2 dY) - \\
 & \int_0^1 \frac{\partial w}{\partial \tau} (Y + \zeta) \frac{\partial^2 \phi}{\partial \tau^2} dY - \int_0^1 (Y + \zeta) \frac{\partial^2 w}{\partial \tau^2} \frac{\partial \phi}{\partial \tau} dY + \\
 & M \left(\frac{\partial^2 w}{\partial \tau^2} - (1 + \zeta) \frac{\partial^2 \phi}{\partial \tau^2} \right) \frac{\partial w}{\partial \tau} \Big|_{Y=1} - l \frac{\partial^2 w}{\partial Y \partial \tau} \left(\frac{\partial^2 \phi}{\partial \tau^2} - \frac{\partial^3 w}{\partial Y \partial \tau^2} \right) \Big|_{Y=1} - \\
 & \left(M(1 + \zeta) \frac{\partial^2 w}{\partial \tau^2} + l \frac{\partial^3 w}{\partial Y \partial \tau^2} \right) \Big|_{Y=1} \frac{\partial \phi}{\partial \tau} \quad (5-62)
 \end{aligned}$$

where

$$w = \frac{\partial w}{\partial \tau} = 0 \text{ at } y = 0. \quad (5-63)$$

The boundary terms derived from Hamilton's principle, Eq. (5-46) and Eq. (5-47) can be substituted into the first two terms of Eq. (5-62). The equation of motion for the cantilever, Eq. (5-44) is substituted into the third integral term, and the equation of motion for the beam and hub, Eq. (5-45) is substituted into the fourth term. Carrying out the substitutions and simplifying gives:

$$\dot{F} = M_f \frac{\partial^2 w}{\partial Y \partial \tau} \Big|_{Y=1} - \frac{\partial M_f}{\partial Y} \frac{\partial w}{\partial \tau} \Big|_{Y=1} + \int_0^1 \frac{\partial^2 M_f}{\partial Y^2} \frac{\partial w}{\partial \tau} dY + \frac{\partial \phi}{\partial \tau} (T_0) \quad (5-64)$$

Because the film distribution is uniform in Y , M_f does not vary with length, therefore, $\frac{\partial M_f}{\partial Y}$ and $\frac{\partial^2 M_f}{\partial Y^2}$ are zero. Retaining the nonzero control terms gives:

$$\dot{F} = M_f \frac{\partial^2 w}{\partial Y \partial \tau} \Big|_{Y=1} + \frac{\partial \phi}{\partial \tau} (T_0) \quad (5-65)$$

The above terms are to be minimized.

5.4.1 Extension of Analysis to Include All Beams

To extend the analysis to include the three remaining beams, the configuration of all four beams can be specified using the generalized coordinates $w_i(Y, \tau)$, where $i=1,2$ for the two beams on the positive and negative y -axis, and $w_i(X, \tau)$ for $i=1,2$ for the two beams on the positive and negative x -axis. Similarly with the single beam w_i (note: w_i refers to all beams) is measured perpendicular from the rotating coordinate frame to a point on the i 'th beam. *It is important to note that each w_i is completely independent*

meaning that the configurations of each beam can be arbitrarily specified independent of the configurations of the other beams, and therefore, independently varied. This is primarily due to the fact that the hub geometric boundary conditions require that $w_i(0, \tau) = \frac{\partial w_i}{\partial Y} \Big|_{Y=0} = \frac{\partial w_i}{\partial X} \Big|_{X=0} = 0$. Hence, the only coupling that exists between individual beam components is again the result of the hub transient dynamics caused by inertial effects. Because ϕ and w_i are independent generalized coordinates, variations in these parameters will produce four independent partial differential equations, together with boundary conditions, all of which are coupled through the hub coordinate ϕ .

Because the kinetic energy and potential energy terms of each beam are identical in form to the single beam case, the mathematical operations involved for the multiple beam case are simply those of the single beam case repeated four times. The resulting beam equations will be identical in form to the single beam equation differing only by the subscript added to $w(Y, \tau)$ and $w(X, \tau)$ needed to distinguish between the beams. The hub equation for the multiple beam case is expanded to include the terms needed to account for the additional inertial torques created by the other three beams. The final form of this equation is identical to the single beam case with the exception that those terms relating to the inertial torques of the beam and tip mass are repeated four times. These four sets of terms are divided into two subsets which differ by the spacial derivatives, X or Y , with the elements of each subset differing by the subscript on $w(Y, \tau)$ and $w(X, \tau)$. As previously stated, the potential energy and kinetic energy terms of the beams and tip masses are all identical in form to the single beam case. Therefore, including these additional energy terms in the Lyapunov functional results in a functional with four sets of energy terms, related to potential and kinetic energy of the beams and kinetic energy of the tip masses, summed together where each set has identical form, viz.

$$\begin{aligned}
 F = & \sum_{i=1}^2 \left\{ \frac{1}{2} \int_0^1 \left[\left(\frac{\partial^2 w_i}{\partial Y^2} \right)^2 + \left(\frac{\partial w_i}{\partial \tau} - (Y + \zeta) \frac{\partial \phi}{\partial \tau} \right)^2 \right] dY + \right. \\
 & \left. \frac{1}{2} \int_0^1 \left[\left(\frac{\partial^2 w_i}{\partial X^2} \right)^2 + \left(\frac{\partial w_i}{\partial \tau} - (X + \zeta) \frac{\partial \phi}{\partial \tau} \right)^2 \right] dX \right\} + \\
 & \sum_{i=1}^2 \left\{ \frac{1}{2} M \left(\frac{\partial w_i}{\partial \tau} - (1 + \zeta) \frac{\partial \phi}{\partial \tau} \right)_{Y=+1}^2 + \frac{1}{2} M \left(\frac{\partial w_i}{\partial \tau} - (1 + \zeta) \frac{\partial \phi}{\partial \tau} \right)_{X=+1}^2 + \right. \\
 & \left. \frac{1}{2} I \left(\frac{\partial \phi}{\partial \tau} - \frac{\partial^2 w_i}{\partial Y \partial \tau} \right)_{Y=+1}^2 + \frac{1}{2} I \left(\frac{\partial \phi}{\partial \tau} - \frac{\partial^2 w_i}{\partial X \partial \tau} \right)_{X=+1}^2 \right\} + \frac{1}{2} I_h \left(\frac{\partial \phi}{\partial \tau} \right)^2 \quad (5-66)
 \end{aligned}$$

Note that the kinetic energy term of the hub is unchanged. The mathematical operations performed on the multiple beam functional are the same as those for the single beam functional repeated four times, once for each beam. Therefore, the results

for the multiple beam case are as follows:

$$\dot{F} = \sum_{i=1}^2 M_{f_i} \frac{\partial^2 w_i}{\partial Y \partial \tau} \Big|_{Y=\pm 1} + \sum_{i=1}^2 M_{f_i} \frac{\partial^2 w_i}{\partial X \partial \tau} \Big|_{X=\pm 1} + \frac{\partial \phi}{\partial \tau} (T_0) \quad (5-67)$$

The term $\frac{\partial^2 w_i}{\partial Y \partial \tau} \Big|_{Y=\pm 1}$ ($\frac{\partial^2 w_i}{\partial X \partial \tau} \Big|_{X=\pm 1}$) is the angular rotation of the i 'th beam at end $Y = \pm 1$ ($X = \pm 1$) measured with respect to the rotating frame of reference. M_{f_i} is the moment applied to the i 'th beam by the i 'th film actuator. Note that because there is independent control over each individual film, meaning that the sign of M_{f_i} can be positive or negative, the sign of the above terms can be independently specified to be negative if the sign of $\frac{\partial^2 w_i}{\partial Y \partial \tau} \Big|_{Y=\pm 1}$ ($\frac{\partial^2 w_i}{\partial X \partial \tau} \Big|_{X=\pm 1}$) is known. The reason the terms are additive is because each beam represents a separate elastic continuum governed by independent differential equations with independent forcing terms on the right hand side. Therefore, the configurations of these beams can be independently controlled by M_{f_i} .

The control law is formulated as follows:

$$V(t)_i = -\text{sgn}\left(\frac{\partial^2 w_i}{\partial Y \partial \tau}\right)_{Y=\pm 1} V_{\max_i} \quad (5-68)$$

$$V(t)_i = -\text{sgn}\left(\frac{\partial^2 w_i}{\partial X \partial \tau}\right)_{X=\pm 1} V_{\max_i} \quad (5-69)$$

where, $i=1,2$, and $V(t)_i$ is the control voltage. It is positive if the angular velocity of the i 'th cantilever end is negative, and vice versa. V_{\max_i} is the maximum applied voltage. The angular rotation of the beam tip relative to the rotating frame is the difference between the angular velocity of the beam tip and the hub in inertial space. In computing these partial derivatives, a sign convention is adopted which is consistent with the right hand rule associated with an inertial reference frame. Adopting the sign convention of Figure 5-5, the hub motion is positive with all partial derivatives representing negative rotations, for example:

$$\vec{\omega}_{\text{tip}_1} = \left(\dot{\phi} - \frac{\partial^2 w_1}{\partial Y \partial \tau} \Big|_{Y=1}\right) \hat{u}_z \quad (5-70)$$

$$\frac{\partial^2 w_1}{\partial Y \partial \tau} \Big|_{Y=1} = (\vec{\omega}_{\text{hub}} - \vec{\omega}_{\text{tip}_1}) \quad (5-71)$$

The general control law becomes:

$$V(t)_i = -\text{sgn}(\vec{\omega}_{\text{hub}} - \vec{\omega}_{\text{tip}_i}) V_{\max_i} \quad (5-72)$$

where, $i=1,\dots,4$ for all four beams.

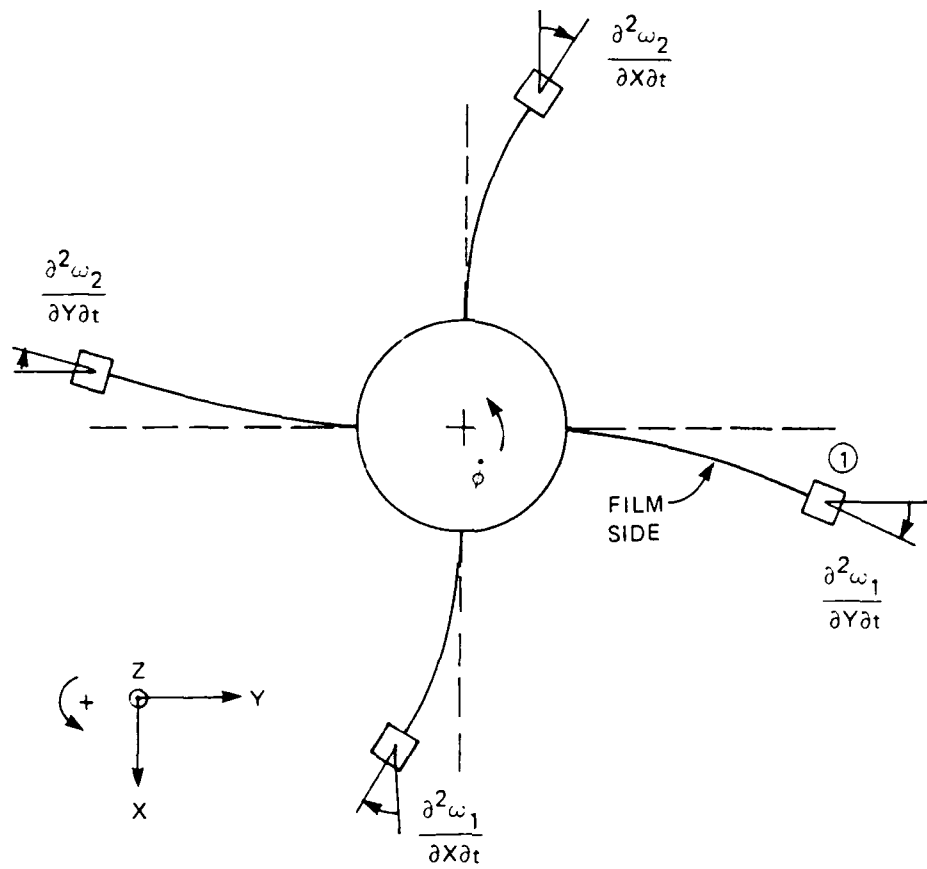


Figure 5-5. Sign convention of angular rates.

Figure 5-5 shows the situation where $\vec{\omega}_{\text{hub}} > \vec{\omega}_{\text{tip}}$ resulting in a negative voltage applied to the film. Negative voltage on the film causes it to expand creating a moment acting to restore the beam to its original undeformed shape. Similarly, if the angular velocity of the tip was greater than that of the hub, the curvature of the beam would be opposite to that shown, and the voltage would be positive causing the film to contract.

Essentially, the control algorithm senses the deformation of the beam from the relative angular velocity of the two ends, then applies maximum voltage so that the motion is opposed. With this control law, rigid body motion of the cantilever is of no consequence because relative motion is used. Also, the coupling of beam motion through the hub is of no consequence because the control law always works against beam motion regardless of where the disturbance originated. Although energy is transferred from one beam to another via the hub, the control law always acts to damp out motion, thereby reducing the total energy within the system.

5.5 Constraints Associated with the Use of Angular Accelerometers

The Lyapunov control law derived in this analysis is based on angular rate measurements at both the tip of the beam and the hub. However, in practice the use of angular accelerometers is limited to measurements involving only the second mode and higher. The angular accelerometers do not have the sensitivity to give accurate measurements of the small angular accelerations associated with the first bending mode. To remedy this problem linear accelerometers were used to sense the rate of deflection of the beam for the first bending mode. Theoretically, the control law does not allow the use of hub and tip linear velocity as measurements of beam deflection because the choice of applying either a positive moment or negative moment is determined by the rate of change of the curvature at the end of the beam. However, for the first mode, positive or negative curvature is directly related to the sign (+ or -) of the deflection at the beam end. Because this directional sense is not lost, it is permissible to substitute linear velocities in place of angular velocities for the first mode.

Section 6

Application of the PVF₂-Film Actuators to the Full-Scale Experiment

6.1 Introduction

The full-scale experiment required a PVF₂ film actuator to be bonded to each of the four cantilever arms of the AFAL structure. In turn, each actuator was to be connected to a controllable Kepco high-voltage power source. The dimensions of the cantilevers were each 4 ft. × 0.5 ft.

Previously (see Sections 2, 3, and 4) technology had been developed to bond PVF₂ to sub-scale experiment structures. It was expected that this technology would be adequate to the task of attaching the film actuators to the much larger full-scale experiment aluminium cantilever arms. In actuality, new problems arose which required further technology development to ensure successful long term bonding of the film to the structure, and reliable bonding of the high voltage connector to the outer metalized surface of the PVF₂ film.

6.2 Background

Four PVF₂ films were to be bonded to the four cantilever beams with no ripples or bubbles to be introduced by the procedure. The glue thickness was to be minimized so that the elasticity and damping properties of the film were negligible, and to ensure a reliable, long-term bond.

Numerous previous experiments were carried out with PVF₂ film and small $\frac{1}{2}$ in × 6 in subscale beams of feeler gauge stock material. The bonding process for these beams is considerably simplified by the small surface area to be covered. The glue can be quickly spread to a uniform thickness before becoming tacky and unworkable. Also, the relative stiffness of the film, because of its small size, is greater thus improving the handling qualities. The small area of the film also assures uniformity which means that no one

side is longer than the other. For these reasons, the bonding process for the small scale experiments proved to be easy by comparison to the difficulty encountered in bonding the PVF₂ film to the full-scale experiment structure. Furthermore, if mistakes were made with the small scale specimens it was a simple matter to start over because of the readily available stock of these items which was on hand. In the case of the full scale structure, several different techniques and a variety of adhesive types were experimented with before a satisfactory combination was found.

6.3 General Procedure

The general procedure was to first thoroughly clean one side of each cantilever arm structure with acetone and Kim-Wipes and then to apply a thin uniform layer of epoxy adhesive to that side. The cantilever was considered clean when no dirt or discoloration appeared on the paper towels. The side of the film to be bonded was also lightly cleaned with acetone then placed on the cantilever such that no ripples or bubbles were present. "Lightly cleaned" means that very little pressure was applied to the film with the Kim-Wipe to avoid damage to the film. When the adhesive dried, excess film was trimmed off with a razor blade. The exposed surface of the film was next coated with an additional layer of silver conductive paint for improved conductivity. A thin brass strip was then glued with silver conductive epoxy to the base of the cantilever to serve as the connection point for the power supply lead.

6.3.1 Bonding of the PVF₂ Film

Six films were purchased for the experiment: four for the experiment arms, and two spares. The films were 52 μ m in thickness and had aluminum metalization on both sides. The 52 μ m thickness was chosen as a result of discussions with the Penwalt Corporation (the manufacturer of the film). It was expected that this thickness would have the best handling qualities. In retrospect, it would have been better to have the film metalized on one side only for three principal reasons. First, the adhesive does not actually bond to the film but to the metalization on the film. Consequently, the ultimate peel strength of the bond is determined not by the adhesive but by the strength of the bond between the metalization and film; this bond strength is low. Second, the film has a positive and negative side to it which determines whether the film contracts or expands in the presence of an electrical field (in other words, if the film were placed in an electric field and it contracted, turning it over would cause it to expand). Differentiating between the positive and negative sides with metalization on both is difficult. This point is important because for consistency it is desirable that all films either contract or expand given a positive or negative voltage, respectively. Metalization on one side only ensures that all

films are bonded to the cantilever consistently with either the positive or negative side exposed. Finally, when the film is trimmed with a blade short circuits often develop between the two metalized faces. These shorts generally go away after the first proof test with voltages in the range of 100 volts. Also, the gap between the two faces limits the amount of voltage that can be applied without arcing. This voltage is in the range of 400 volts. Preventing arcs or short circuits whenever possible is important to prevent localized damage to the film caused by excessive heat.

The dimensions of the film were specified to be slightly oversize at $6\frac{1}{2}$ in \times 4ft with the excess to be trimmed after bonding. The extra $\frac{1}{2}$ in was necessary so that complete coverage of the cantilever would be obtained easily on the first attempt to place the film, and any excess adhesive squeezed out along the edges would not easily contaminate the top surface of the film. The last point is important because a rubber brayer was used when the film was placed on the structure to press out trapped air. If adhesive were on the exposed surface, the film would stick to the brayer causing the film to be pulled up from the cantilever. Removing adhesive from the metalized film surface requires the use of acetone and Kim-Wipes. However, the rubbing pressure required to remove the adhesive will also completely remove the metalization.

6.3.2 Selection of Adhesive

Perhaps the most important phase of bonding the films to the cantilever was the selection of an appropriate adhesive. Ideally, a two part epoxy adhesive should be used with low viscosity and a relatively long pot life (about 30 minutes). Pot life is an important factor because once the adhesive becomes tacky the spreading qualities are lost, making it difficult to spread and maintain an even layer.

Several adhesives were tried on test samples. The results are described below.

- (1) ARMSTRONG C-7. This adhesive proved to be the most satisfactory because of its handling qualities (20 to 30 minute pot life) and high bond strength. Although it did not become necessary, if the adhesive were to have become excessively tacky during spreading, it could be thinned with Cell-O-Solve thinner, thus temporarily extending the working time. Single edge razor blades proved to be the simplest and perhaps best tool for spreading the adhesive. The small size of the razor and straight edge allowed for easy handling and spreading of the adhesive.
- (2) 3M 2216 TRANSLUCENT. This adhesive had the longest pot life and lowest viscosity making it the easiest to work with. However, the bond strength was significantly weaker than Armstrong C-7. For this reason the adhesive was considered unacceptable.
- (3) 3M 2158 GRAY. This adhesive had very high strength but proved to be difficult

to spread thinly. The filler (gray material within the adhesive) caused the surface of the adhesive to mat giving it an unacceptable, uneven surface texture for the PVF₂ film.

- (4) VERSILOK ACRYLIC STRUCTURAL ADHESIVE. The Versilok is a two part adhesive where the two components (a thick paste and a liquid) are applied individually to each surface (one component on one surface, the other component on the other surface). The two parts can remain separate indefinitely until pressed together. The advantage of this method is that the thick component of the adhesive has unlimited working time allowing for the adhesive to be spread and worked as long as necessary. This adhesive was not chosen primarily because the liquid component was highly toxic and the bond did not appear to fully cure.
- (5) PERMABOND 501 (SHAFT LOCK GRADE). Permabond is an anaerobic adhesive used to bond gears to shafts eliminating the need for shaft keys. However, in this application the adhesive failed to bond.

Cyano-acrylate adhesives such as Eastman 910 were not considered because these adhesives allowed for only one attempt at correctly placing the film. It had to be right the first time. Once the film contacts the adhesive, there is little chance of repositioning it without damage.

6.3.3 Development and Testing of Application Techniques

In conjunction with testing of the adhesives, different application procedures were also tried using Armstrong C-7. The first was to liquify the adhesive using methyl ethyl ketone (MEK) and paint it on with a brush. The MEK would rapidly evaporate leaving the uncured adhesive. However, this technique failed to provide a satisfactorily even coating, and the small amount of adhesive deposited was impossible to spread or work with. In an attempt to obtain a more even coating a spray gun was used powered by an aerosol propellant (these spray guns are inexpensive and found in most paint stores). This technique did not improve the previous results using the brush.

From experience with previous full scale experiments, a razor blade appeared to be the simplest, cheapest, and perhaps most effective tool for spreading the adhesive. Because of the sharp edge of the razor, a very thin and uniform layer of adhesive was achieved. The general procedure was to mix equal parts of the C-7 for a total amount of about one ounce. Using a spatula, a strip of adhesive (less than one ounce) was spread across the width of the beam at one end. Using the razor, the adhesive is drawn over the entire length of the beam with the excess adhesive pushed off the edges and ends. It is best to start at one side of the beam with the razor slightly overhanging the edge and work toward the other edge each time overlapping the previous work. At all

times the razor should remain in firm contact with the beam, and the motion should be continuous without pause until the end of the beam is reached. The spreading procedure can be repeated, if necessary, to further smooth the adhesive. However, repeated spreading action over the same surface will ultimately cause the adhesive to become excessively tacky resulting in an unacceptable, matted surface. If this were to occur, a few drops of Cell-O-Solve thinner can be placed on the surface with an eyedropper liquefying the adhesive and thereby temporarily extending the working life. After spreading, the cantilever surface should appear to have a thin transparent film with no streaks or buildup.

Having selected the Armstrong C-7 adhesive and the method of application, a preferred technique evolved for applying the film. In this technique, one end of the film was secured with tape to the end of the cantilever, and the other end secured with tape to a thin metal strip about 3 x 7 inches. This strip was held taught about 2 inches above the surface of the cantilever. Starting from the end of the film secured to the cantilever the film was pressed into place with a rubber brayer. Trapped bubbles were also squeezed out by pressing with the thumbs and using a rolling motion. It is advisable to use latex surgical gloves when handling the film to prevent oil from the hands contaminating the metalized surface. After the film was gradually worked into place, any remaining bubbles were pressed out by hand. Minimizing the number of trapped bubbles is important because at high voltages arcing can occur across the air gap formed by the bubbles. Also, maintaining tension in the film during placement is important to remove wrinkles. The wrinkles are a result of differences in the length of the film introduced during the manufacturing process of the film as it is wound onto rolls. Uneven tension in the film as it is rolled stretches one side longer than the other. This difference in length causes excessive bubbles and ripples in the film during gluing if it is not held under some pre-tension.

Once the adhesive cured (24 hrs), the films were trimmed with razor blades along the edges and at the ends to allow room for the attachment of the N₂ jet hoses, sensor wiring, the angle irons at the cantilever base, and the end fitting for the N₂ jets. The aluminized coating was then spray painted with a silver conductive coating of about 1½ to 2 mil thickness for improved conductivity. This last process was subcontracted because of its specialized nature which requires the use of unique spray equipment to achieve the uniform paint thickness desired.

6.4 Proof Testing of Actuators

Once the films were spray painted, the cantilevers were attached to the hub for preliminary checkout using the Kepco power supplies. Brass strips of feeler gauge stock were cut to size (approximately ¼ in. x 5 in.) to serve as electrical leads. These leads were cleaned with acetone then attached to the films using TraCon silver conductive

epoxy. The leads of the high voltage cable from the Kepco were directly attached to each strip and the back side of the cantilever using the conductive epoxy. The use of a conductive epoxy was necessary to ensure a secure bond with low resistance, and most importantly to avoid potential damage to the film and spray coating which would likely be the case with soldering.

Before applying voltage to the films all, high voltage cables were checked for continuity and short circuits. A 1 kilo-ohm, 5 watt resistor was also placed in series with the Kepco to ensure that if a short circuit developed the Kepco would not be subjected to excessively high current loads. The PVF₂ actuators were then "proof" tested with voltages as high as 1000V. This testing removed any short circuits between the front and back surfaces at the edges of the film. However, for the highest voltages used (900-1000 V), additional short circuits continued to appear after the initial group of shorts were removed. To avoid these additional short circuits, the control voltage to the PVF₂ actuators was limited to approximately ± 500 V. Once this preliminary checkout was completed, all high voltage cables were connected and secured with electrical tape.

Section 7

Full-Scale Distributed Parameter Actuator Testing and Results

7.1 Summary

This section describes the distributed parameter actuator damping tests performed on the AFAL structure and discusses the results. Transfer function measurements from random excitation tests were chosen to determine the damping introduced by the PVF₂ actuators. Two excitation sources were evaluated: (1) one of the proof-mass actuators (PMAs), and (2) the air-bearing table torque motor. Due to the nonlinearities of the PMA, the torque motor excitation resulted in less contamination of the transfer function measurements. For low-level torque inputs, the PVF₂ actuators doubled the damping of the scissors mode and provided a 33% increase in damping for the twist mode of vibration.

7.2 Testing methods

In the course of this and a related AFAL/CSDL investigation (the RCS/Linear Discrete Actuator study), it became apparent that the PVF₂ actuators were not appropriate for vibration control during a slewing maneuver. The flexible mode vibrational energy remaining in the structure after the slewing maneuver deceleration phase was too large for the low authority PVF₂ actuators to remove in a short time period. The more powerful discrete linear actuators used in the related study removed the flexible mode energy in less than ten seconds after the deceleration phase of a maneuver. The PVF₂ actuators were estimated to require one to two minutes to damp similar vibrations, too long for a rapid re-targeting maneuver. The PVF₂ actuators (and any other low authority actuator) were more appropriate for vibration control during long-term fine pointing tests or low-level disturbance rejection tasks.

Two testing methods were considered as candidate techniques to provide a measure

of the damping effectiveness of the PVF₂ actuators. The methods were free-decay testing, and bandlimited random-excitation transfer function measurements. Free-decay tests provide decay time and rate-of-decay from a prescribed set of initial conditions as the measures of damping. Transfer function measurements provide information to calculate the equivalent viscous damping factor of a resonance. By comparing the damping factors for the controlled and uncontrolled resonances, one can determine the amount of damping added by the PVF₂ actuators.

The nonlinear control law described by Eq. (5-72) was used for the PVF₂ actuators, modified to use linear velocity instead of angular velocity because of the angular accelerometer constraints discussed in Section 5.5. Tests were performed using the AFAL structure with the structure floating on the air-bearing table. The nonlinear control law caused the damping effect of the PVF₂ actuators to vary inversely with the amplitude of the vibrations; the actuators were more effective for low-level vibrations and less effective for larger vibrations.

Using the free-decay test method, a set of initial conditions is imposed on the structure and the resulting free decay is observed. The effective damping in a nonlinear system can be determined by examining the slope of the decay envelope or 'rate of decay' for a single mode of vibration. However, determining the effective damping is very difficult if more than one mode of vibration is present. To make accurate comparisons between different test runs, one must repeatably prescribe the initial conditions for the structure. Re-creating the initial conditions of a previous run is generally difficult to do experimentally if the structure is even moderately complex, as in the case of the AFAL structure.

The equivalent viscous damping of a resonance can be determined from a transfer function of the structure. The transfer function is generally taken from a force or torque input to a sensor output (e.g., acceleration, velocity, or displacement). Transfer function measurements using bandlimited-random-noise excitation require that the statistics of the excitation and the response of the structure are relatively 'steady-state'. The excitation noise is bandlimited to the frequency range of interest (a narrow band around the resonant frequency of interest, for example). After the excitation is applied to the structure, a short time is allowed for startup transients to decay. A spectrum analyzer is then used to sample the data and perform the FFTs required to calculate a transfer function. Many measurements may be averaged to reduce the effects of disturbances and provide more reliable data. The desired excitation statistics can be repeatably produced, so transfer function measurements for different test runs can be compared easily.

However, transfer functions provide only an 'averaged' view of the behavior of the system over the sampling period of the FFT (or the entire sampling period, if many individual transfer functions are averaged). Since the nonlinear control law will cause amplitude dependent damping, the transfer function damping results will depend on the

vibration amplitude and hence on the amplitude of the excitation to the structure. By performing transfer function tests using several levels of excitation, the nonlinearity of the damping effects can be characterized.

The transfer function testing method was chosen over the free-decay method because transfer function test results are much more repeatable and are less affected by transient disturbances. Also, transfer function tests can easily resolve multiple closely spaced modes in a single test, unlike free-decay tests. Transfer function tests were performed with a range of excitation amplitudes to determine the nonlinearity of the damping from the PVF₂ actuators.

7.3 Evaluation of Excitation Sources

Two actuators were considered as excitation sources for the transfer function testing: one of the PMAs and the air-bearing table torque motor. These linear actuators were used in the RCS/Linear Discrete Actuator study. The PMA applied a force at the tip of one flexible arm. This might, for example, represent a disturbance force applied to a solar panel or an antenna of a satellite. By contrast, the torque motor applied a torque to the hub of the structure, which might represent a disturbance from machinery mounted on the main structure of a satellite. Because the PVF₂ actuators had a very low control authority, the excitation source had to provide low-level inputs to the structure to avoid overpowering the PVF₂ actuator capability.

The PMA excited both symmetric and anti-symmetric modes of the structure and provided a low-level force input to the structure (a summary of the structural modes is given in Appendix A). The vibrations were largest on the arm on which the excitation PMA was mounted and were much smaller on the other three arms. Vibrational energy flowing from one arm to another passed through the hub, which filtered much of the energy because of its mass.

The three arms with lower-level vibrations provided good conditions to test the PVF₂ actuators. However, the PMA was characterized by significant nonlinearities between its input (current) and output (force). The PMA was nonlinear with respect to both position (along its stroke) and current amplitude. Since the transfer function measurements were calculated from the PMA commanded current input to the accelerometer output, the PMA nonlinearities appeared to be within the structure. These nonlinearities greatly reduced the quality of the transfer function measurements. The coherence (a measure of the causality and the noise levels in a system) was very low, and the transfer function magnitudes were not smooth. Very low excitation levels were used in an attempt to operate the PMA in a linear region, but the nonlinearities still resulted in unacceptable transfer function measurements.

The air-bearing table torque motor provided low-level excitation to the structure but

excited only the anti-symmetric modes of the AFAL structure. The torque motor excited all four arms equally, so no one arm was preferred to demonstrate the effectiveness of the PVF₂ actuators. The torque motor displayed a higher control authority on the twist mode (the second anti-symmetric mode) than the scissors mode (the first anti-symmetric mode) because the twist mode involved more hub motion.

The minimum excitation level using the torque motor was limited by the stiction of the air-bearing table. The stiction force was larger than the running friction force and resulted in a larger minimum input torque to the structure. Also, as the vibration level of the structure decreased, the stiction caused the table to appear to have a larger friction force than the running friction force. The damping of the structure (especially the twist mode) increased as the vibration amplitude decreased.

The torque motor was very linear between commanded torque (as input) and torque output. As a consequence, the transfer functions measurements made using the torque motor were much higher quality than those obtained using the PMA. The coherence was high, approximately unity for the entire analysis range, except for anti-resonances. Consequently, the torque motor was chosen as the excitation source for the transfer function testing because much higher quality measurements could be obtained.

7.4 Test Configuration

A schematic of the test configuration used for the distributed parameter actuator damping tests is shown in Figure 7-1. The sensors used for the PVF₂ actuator tests were the Contraves hub angle readout and the four linear accelerometers, one at the tip of each arm. The four PVF₂ actuators were used to damp vibrations of the structure while the air-bearing table torque motor provided the excitation (or disturbance) to the AFAL structure.

The MicroVAX computer received digitized sensor readings through an analog-to-digital interface board, and the air-bearing table control electronics. A modified version of the control law described by Eq. (5-72) (but using linear velocity instead of angular velocity) was implemented by integrating the linear accelerometer readings, and differentiating the hub angle readings to determine the linear velocities at each end of the arms. The voltage commands for the PVF₂ actuators were converted to analog signals which were amplified by four Kepco BOP 1000M power supplies (one required for each actuator) and then applied to the actuators. *

The MicroVAX controller generated the bandlimited noise which excited the structure. The bandlimit was chosen to excite only those modes composed of the first bending mode of the arms of the structure so that the linear accelerometers could be

*A description of the MicroVAX control computer and its interface to the AFAL structure is given in Appendix B.

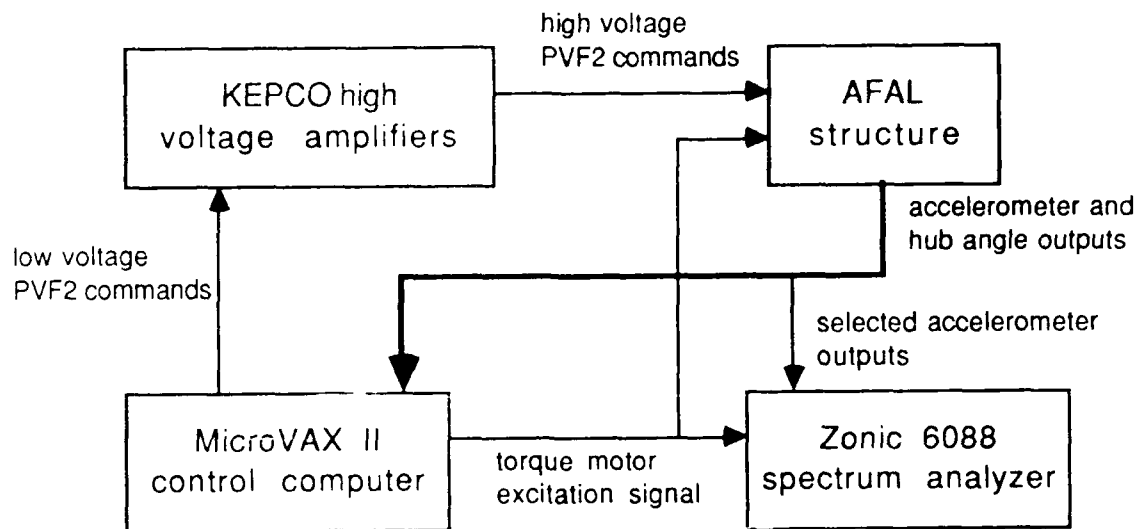


Figure 7-1. Schematic of the experimental facility configuration used for the PVF₂ actuator tests.

used instead of angular accelerometers. The structural modes of interest were clustered near 0.4 to 0.8 Hz, while the next higher frequency cluster of modes occurred near 6.4 Hz.

Digitally generated white noise was bandlimited by a low pass filter with four poles at 2.2 Hz. The bandlimited noise was converted to an analog signal and applied to the torque motor of the air bearing table to excite the structure.

A Zonic model 6088 four-channel spectrum analyzer was used to collect data and perform the FFT operations required to calculate the transfer functions. The bandlimited noise and three tip accelerometer signals were used as input to the spectrum analyzer. This configuration resulted in three transfer functions per test run. The remaining accelerometer could not be used because of the channel limit. The hub angle sensor could not be used because its output was available only as a digital signal and not available in analog form. The multiple degree-of-freedom (MDOF) estimation routine incorporated in Zonic MODAL (a modal analysis program) was used to estimate the damping of the modes for each test run.

7.4.1 High Voltage EMI and Safety Concerns

The use of high voltage signals (± 500 V) on the large AFAL structure raised several concerns relative to electro-magnetic interference. The PVF₂ actuators were actually a large unshielded antenna which could contaminate accelerometer signals with crosstalk

noise. Another concern was arcing between faces of the PVF₂ actuators which caused damage to the PVF₂ film and reduced the effectiveness of the actuators. Personnel safety was also a concern because of the size of the AFAL structure and the large motions through which it could travel.

The accelerometer signal lines ran parallel to the PVF₂ actuators and the high voltage lines carrying the command signals for nearly 35 feet. It was anticipated that the high voltage (± 500 V) actuator command signals would cause noise problems on the accelerometer signals. To reduce the contamination of the accelerometer signals, proper shielding practice was followed whenever possible. All signals (both high and low voltage) were transmitted with shielded, twisted-pair conductors. The unshielded lead length for connections at accelerometers was kept to a minimum. Separate high- and low-power ground paths were provided.

Attention to shielding virtually eliminated crosstalk between the high voltage leads and the accelerometer signal leads. No additional signal conditioning (e.g., common-mode rejection amplifiers, etc.) was needed for the accelerometer signals.

The PVF₂ film used in the actuators had a breakdown voltage of 1500-2000 volts. However, arcing across the faces of the film occurred at much lower voltages. Some arcing across the faces of the PVF₂ actuators at the edges occurred at low voltages (100-200 V) when voltage was first applied. Cutting and trimming the PVF₂ film resulted in small filaments of the plating on the faces of the PVF₂ film partially bridging the gap across the film at the cut edge. The low voltage arcing was caused by these filaments being burned away. The arcing caused no damage to the film, and up to 1000 volts DC was applied to the actuators to 'clean' the edges and prevent further arcing of this type.

After the initial cleaning of the PVF₂ film, occasional arcing occurred at higher voltages (500-1000 V) and was evident in the interior of the actuator as well as at the edges. This type of arcing did damage the PVF₂ film. In one case, the arcing under a signal lead contact resulted in a small hole. The silver paint was heated and flowed into the hole, making contact with the back face of the PVF₂ thus shorting the actuator. The arcing occurred most often when the applied voltage was switched suddenly, but also occurred when a DC voltage was applied.

The Kepco high voltage amplifiers displayed large voltage overshoots to step inputs because of the reactive impedance of the PVF₂ actuators. Resistors were placed in series with the capacitance of the PVF₂ actuators to limit the current output from the Kepco amplifiers and to improve their voltage regulation. These steps greatly reduced the arcing which occurred when the applied voltage was switched.

One possible cause of the arcing with a DC voltage was inherent defects in the PVF₂ film. The high voltage arcing appeared to occur more often at the start of a test after the PVF₂ actuators had been inactive for several days, so the defects may be

related to aging of the PVF₂ film or to straining of the PVF₂ during slewing tests on the experiment structure. Another cause may be air bubbles in the adhesive layer between the PVF₂ film and the aluminum arms. A voltage limit of +500 volts was eventually accepted to reduce the high voltage arcing.

The safety risk was reduced by insuring that only the outer faces of the PVF₂ actuators were at the high voltage potential. The rest of the structure (arms, hub, air-bearing table, etc.) was grounded. The Kepco high voltage amplifiers were powered from a switched outlet strip which allowed all four amplifiers to be disabled at once. Notices were posted during tests to inform personnel entering the area that a test was in progress and that high voltage potentials were present on the structure.

7.5 Experimental Results and Analysis

The PVF₂ distributed actuator damping tests were performed in pairs. A baseline test was performed using a chosen level of structural excitation with the PVF₂ actuators turned off (i.e., the voltage limit was set to zero). The baseline test provided a measure of the passive damping in the structure at the specified excitation level. Changes in the baseline damping were attributed to nonlinear damping in the air-bearing table (primarily stiction and friction). The second test of the pair used the same excitation level but with the PVF₂ actuators activated. Using this procedure, the change in damping between the two tests was attributed solely to the PVF₂ actuators.

Table 7-1 shows the excitation torque used, the passive and active loss factors η , and the difference between the active and passive loss factors. The active loss factor is the equivalent linear damping observed in the system with the PVF₂ damper activated. The difference in loss factors is the equivalent linear damping added by the PVF₂ damper. Results are presented for the two anti-symmetric modes in the frequency range of interest.

Three excitation levels were used for the PVF₂ actuator tests. The excitation values shown in Table 7-1 were the average power spectrum levels of the commanded torque over the frequency range of 0.01 to 2.60 Hz. For the highest level of excitation, the PVF₂ actuators were overpowered by the excitation as indicated by the small added damping. At the lowest level of excitation, the nonlinear damping of the air-bearing table dominated the damping of the twist mode. Nonetheless, significant damping was added by the PVF₂ actuators.

Only one active voltage limit was used for the PVF₂ actuators, viz. 500 V, during the damping tests. Higher voltages were not used in order to reduce arcing across the PVF₂ film and consequent damage to the film. Lower voltage limits (100-200 V) were used during preliminary tests, but the low authority nature of the PVF₂ actuators required a higher voltage level to produce significant damping. The damping added by

Table 7-1. PVF₂ distributed actuator damping results.

Excitation (lb·ft) ²	Mode	Freq. (Hz)	Loss factor, η		Change in loss factor
			0 volts	500 volts	
0.150	scissors	0.34	0.0056	1.01	0.0045
	twist	0.77	0.0179	2.36	0.0057
0.018	scissors	0.35	0.0087	1.45	0.0058
	twist	0.78	0.0370	0.0504	0.0134
0.004	scissors	0.35	0.0087	0.0176	0.0089
	twist	0.79	0.0916	0.1245	0.0329

the PVF₂ actuators increased as the excitation level decreased. The damping values achieved were similar to values achieved in the scaled beam and single arm experiments described in Sections 2 and 4.

The PVF₂ actuators should be equally effective for both modes because the shape of a displaced arm is very similar for each mode, but they seemed to be more effective for the twist mode. This is a direct consequence of the nonlinear switching control law. The PVF₂ actuators simply exerted the most effort on the highest amplitude mode. More damping was added to the twist mode because it was excited more by the torque motor and, consequently, displayed the largest amplitude.

Figures 7-2 through 7-4 show representative transfer function magnitudes for each excitation level tested. In general, the twist mode received the most active damping, but the scissors mode displayed the most reduction in amplitude with a much smaller increase in damping. One reason for the larger reduction in amplitude is that the baseline damping for the scissors mode was very small. The added active damping nearly doubled the damping of the scissors mode in each case. Another reason is that the torque motor excited the scissors mode less than the twist mode, therefore, less disturbance energy needed to be dissipated to produce a given reduction in vibration amplitude.

The transfer function plots also demonstrate how the non-linear damping in the air-bearing table dominated the twist mode damping for the lowest excitation level. The scissors mode transfer function amplitude was independent of the excitation level, which corresponds to a linear system. In contrast, the twist mode transfer function changed with the excitation level which indicated a non-linearity for the twist mode. Nonetheless, the PVF₂ actuators provided a noticeable reduction in peak transfer function magnitudes

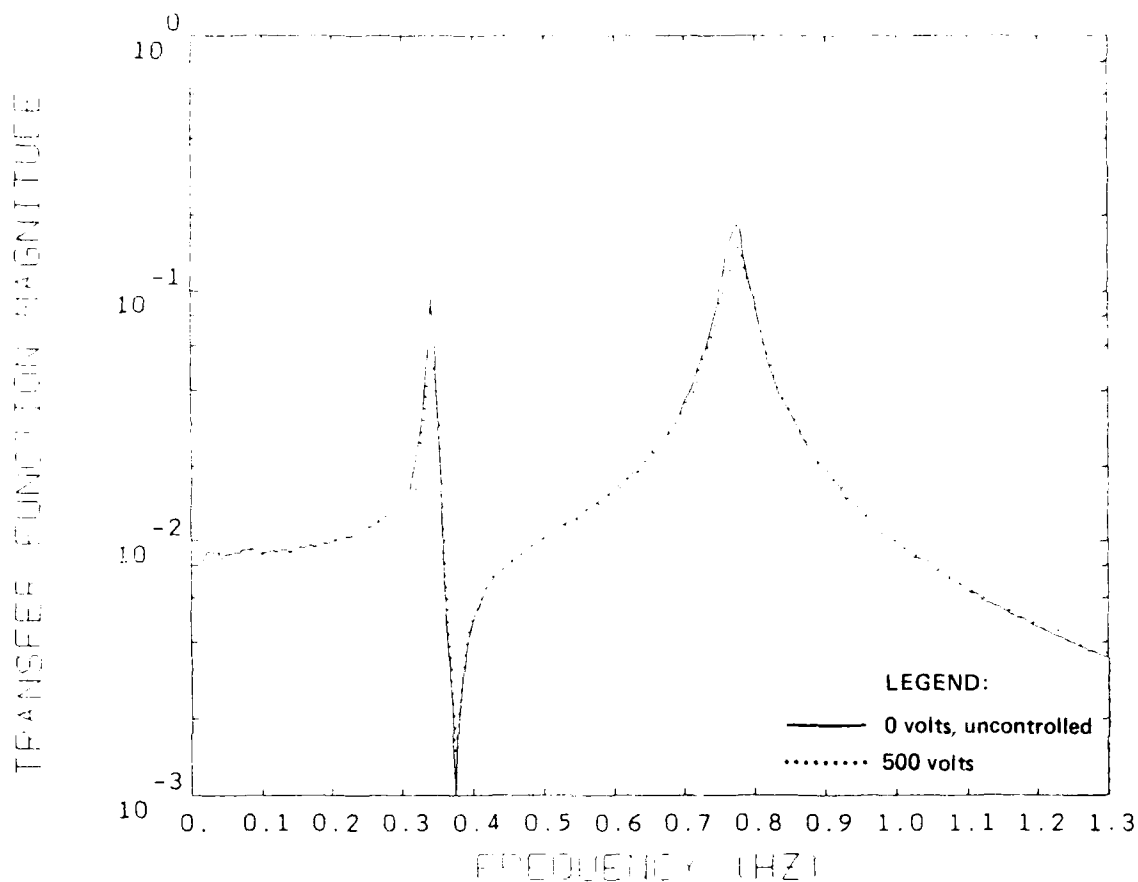


Figure 7-2. Transfer function magnitudes using 0.150 (lb-ft)^2 excitation.

for each excitation level.

The experiments demonstrated that low authority actuators are not well-suited to remove energy from large transient disturbances in a short time period. The actuators are limited in the amount of energy they can remove, so many cycles of vibration may be needed to damp such vibrations. This was the reason the PVF₂ actuators were not used in combination with the thrusters on the AFAL structure. The PVF₂ actuators could not significantly reduce the large flexible mode vibrations during the short duration of a slewing test.

The steady-state effectiveness of low authority actuators (such as the PVF₂ actuators) for vibration control depends on the relative amounts of disturbance or excitation energy input to the system, the energy dissipated by passive damping, and the energy dissipated by active damping. If a large disturbance is present, the energy removed

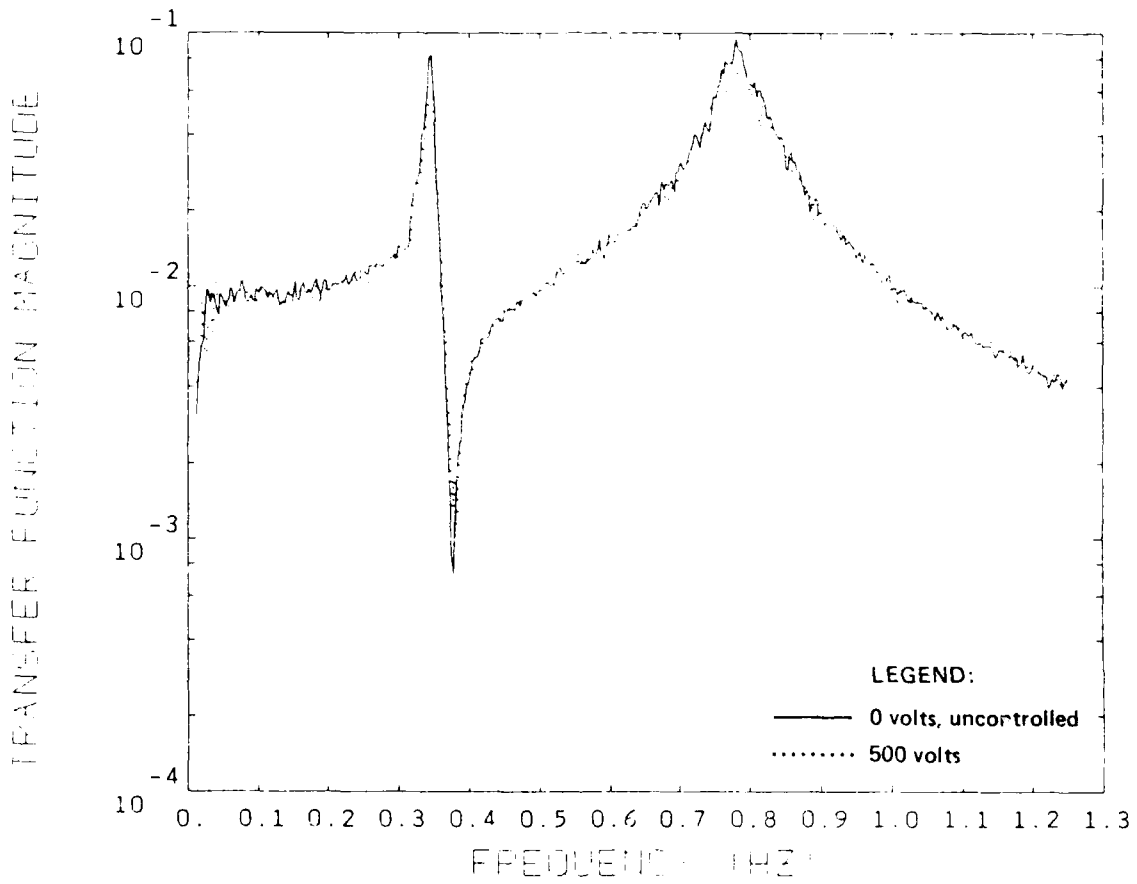


Figure 7-3. Transfer function magnitudes using 0.018 (lb-ft)^2 excitation.

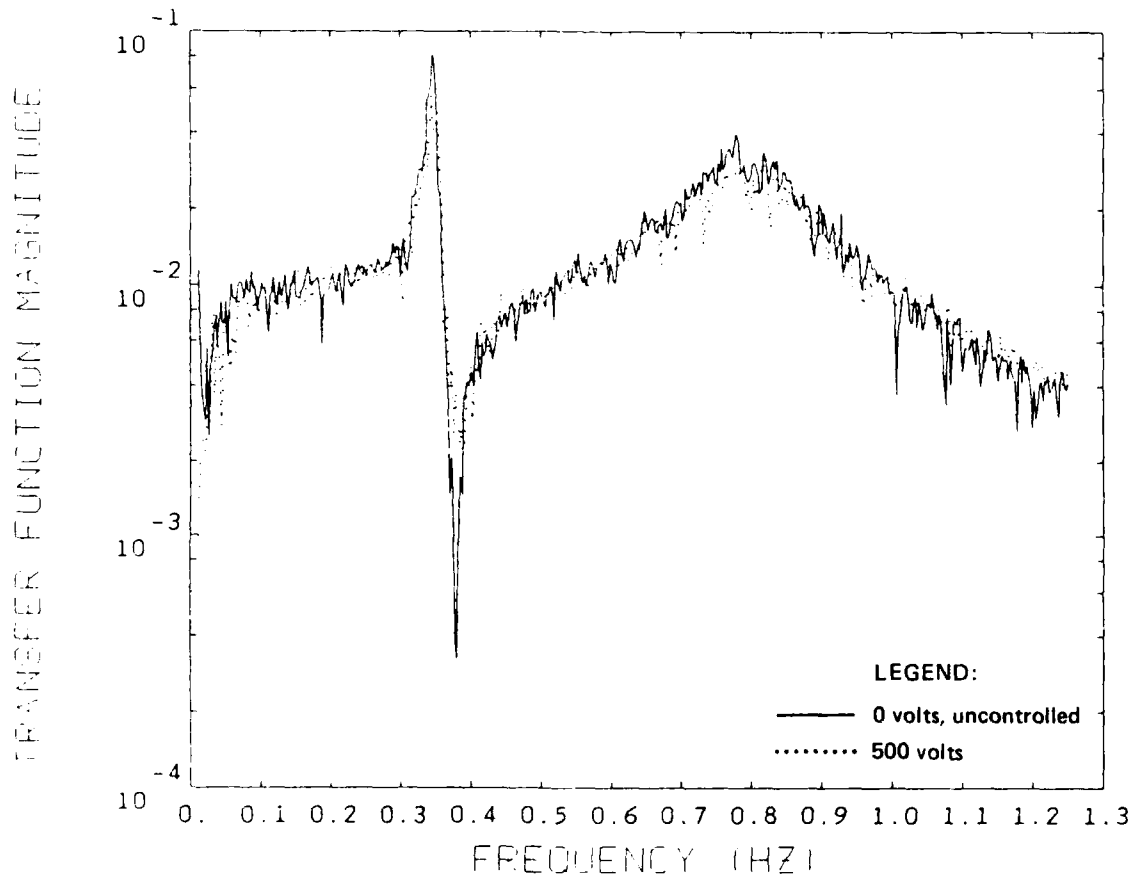


Figure 7-4. Transfer function magnitudes using 0.004 (lb-ft)^2 excitation.

from the structure by a low authority actuator will be negligible. Similarly, if the energy removed by passive damping is large, the added damping from a low authority actuator will again be negligible. The passive damping energy can be large if either the system loss factor is large or the amplitude of vibration is large. Therefore, low authority actuators will perform best when used in systems that have low disturbance forces and small loss factors. Possible applications include long-term fine pointing tasks or, more generally, low-level disturbance rejection in very lightly damped structures.

Section 8

Summary and Conclusions

8.1 Summary of the Results

8.1.1 Scaled Experiments and Theory

8.1.1.1 Lyapunov Damper

An active vibration damper which uses a distributed piezoelectric actuator bonded directly to a structure, and 'bang-bang' feedback control (Lyapunov control) to damp transverse vibrations was experimentally tested on two different beams. One was a steel cantilever beam with a 6.7 gram tip mass. This was a dynamically scaled model of one arm of the AFAL structure. The second was an aluminum cantilever beam with a 2.04 kg tip mass; this was actually one of the arms of the full-scale AFAL structure.

Free vibration tests of the first mode of the steel beam were conducted by displacing the tip 2 cm, and releasing it. A beam without active control had a settling time of over 2 minutes. Free decay tests using the Lyapunov control algorithm and a control amplitude of 500 volts decreased the settling time to 8 seconds. Similar first mode tests were performed on the aluminum beam. The initial condition for these tests was a tip displacement of 16.7 cm. Without active control the beam vibrations had a decay time of over 400 seconds. Using Lyapunov control with a control amplitude of 400 volts reduced the settling time to 126 seconds.

The active Lyapunov damping demonstrated in this study is nonlinear. If it were applied to a structure which had no internal damping, the tip displacement would decay linearly in time. This indicates a changing system loss factor. Using moderate feedback voltages, the effective loss factor of the closed loop system increased dramatically as the vibration level decreased. The passive loss factor of the steel beam was $\eta = 0.002$ for small amplitude tip displacements. Using the Lyapunov damper with an amplitude of 100 volts increased the loss factor to $\eta_{100} = 0.046$ at a tip displacement of 0.5 mm. Active damping with a 500 volt control amplitude increased the loss factor to

$\eta_{500} = 0.375$ at the same displacement amplitude.

The passive loss factor at small tip displacements of the aluminum beam was $\eta = 0.0019$. Lyapunov control with an amplitude of 100 volts increased the system loss factor to $\eta_{100} = 0.030$ at a tip displacement amplitude of 1.7 cm. Active damping with a control amplitude of 400 volts increased the loss factor to $\eta_{400} = 0.080$.

The experimental results from the small-scale and full-scale tests were compared to nondimensional simulation results. Overall the experimental results match those predicted by the simulation. For large amplitude vibrations, unmodelled damping (such as air drag) caused higher damping than predicted by the simulation, especially for the full-scale beam. For small amplitude vibrations, the damping observed in the experimental tests approached the values predicted by the simulation.

Even though the small beam was dynamically scaled from the larger beam, the damping results could not be directly scaled. This was because the PVF₂ damper could not be dynamically scaled exactly because of experimental constraints (e.g., the PVF₂ film was not available in the appropriate thickness, and the large control voltages needed could not be generated easily). Nevertheless, the good correlation achieved between the experimental and simulation results validated the scaling parameters chosen, and allowed scaling laws to be used to predict the performance of other PVF₂ damper/beam combinations.

The Lyapunov damper was also demonstrated to be very effective on the second and third bending modes of the aluminum beam. The initial conditions for these tests were established by using the film actuator to excite the beam at the desired modal frequency. The Lyapunov control algorithm used on the first mode tests was also used for these tests. For the second mode of the aluminum beam, the initial condition was an angular acceleration at the tip of 56.5 rad s^{-2} . The Lyapunov control decreased the settling time from a free decay of 41 seconds to a controlled settling time of 7.4 seconds using a control amplitude of 400 volts. The initial condition for the third mode tests was an angular acceleration of 127 rad s^{-2} at the tip. For the third mode the settling time was reduced from 20.5 seconds to 3.8 seconds using a control amplitude of 400 volts.

These experimental results verify that the Lyapunov damping is most effective for smaller vibration levels. This is because the nonlinear damping dissipates an increasing percentage of the system energy as the vibration amplitude decreases. This type of active damping may be most effective as a method of keeping resonant vibrations from building up due to the potentially high levels of damping that can be achieved for low level vibrations.

8.1.1.2 Active Constrained Layer Damper

A constrained layer damper which uses the PVF₂ actuator as an active constraining layer was modelled and experimentally tested on a dynamically scaled model of one arm of the AFAL experiment structure. The general system consisting of a base structure, viscoelastic layer, and active constraining layer was modelled resulting in a sixth order partial differential equation governing the transverse motions of the beam. The specific case of an active constrained layer damper applied to a cantilevered beam with tip mass and rotary inertia was addressed.

This model revealed that there are two ways the active constraining layer affects the beam. The first is by contributing to the shear strain in the viscoelastic material (VEM) layer. As a result, it is possible to actively modulate the amount of energy dissipated. Since the amount of energy dissipated by the VEM is proportional to the strain, this mechanism is expected to be most effective for large amplitudes.

In addition to internal dissipation, the active control appears as work at the system boundary. With the constraining layer fixed to the tip mass and left free at the root, the active portion of the stress in the constraining layer appears as a boundary moment which can do work on the system. This result is similar to that found by Bailey [3] and is the basis of the Lyapunov control algorithm. In the limit, as the VEM becomes perfectly rigid and the loss modulus goes to zero, the model of the active constrained layer damper and the Lyapunov controller are identical. If the VEM has finite storage and loss moduli, the system will be affected by both the active dissipation and the boundary work.

The active constrained layer damper was tested experimentally with three different feedback control laws: (i) a proportional control law which fed back tip displacement to maximize the shear and shear rate across the VEM (within the constraints of a linear control law); (ii) a Lyapunov-based switching control law which fed back tip velocity to maximize the boundary work; and (iii) a proportional control law which fed back tip velocity as a linear version of the Lyapunov-based switching control law. The results of these tests show that dampers with thicker viscoelastic layers and stiffer (i.e. thicker) constraining layers add the most damping. A damper consisting of a 2.54×10^{-5} m thick VEM layer and a 110×10^{-6} m thick PVF₂ constraining layer consistently added the most damping to the structure for all the control laws. The experiments using the switching control law demonstrated the largest increase in damping for all damper configurations. The proportional control using position feedback was consistently the least effective control law. These results demonstrate that the maximum increase in damping due to active means for a damper using an active PVF₂ constraining layer and a viscoelastic damping layer is achieved by doing work on the system boundary and not by augmenting the shear losses in the viscoelastic layer.

An analysis of the stresses induced in the viscoelastic layer of both an active and

passive constrained layer damper showed that a passive design which used a steel constraining layer greatly outperformed the damper with the active PVF₂ constraining layer. This was because of the significant difference in the stiffness of the two constraining layers.

8.1.2 Full-Scale Experiment Verification Study

The analysis and control algorithm development was extended to focus on the full-scale experiment. A detailed model of the full-scale AFAL test structure was developed followed by the derivation of control laws for the PVF₂ film actuators. The actuators damp out flexural motion of the cantilevers measured relative to a coordinate frame fixed to the hub.

The key result of the analysis was that the film actuator exerts independent control in the governing equation for the flexural motion of the cantilever to which it is bonded. Although coupling of beam motion occurs through the hub, this coupling is a result only of inertia forces produced by beam and hub motion. These forces can be produced by a given set of initial conditions, external disturbances, or the motion of a beam induced by control action of the film. The stress field induced by the film is contained within the elastic continuum of that beam; it is not transmitted through the hub. For this reason, four identical but independent control laws were derived, one for each beam. The control laws require information only about the motion of the beam each is controlling. Essentially, the algorithm senses whether the net curvature of the beam is increasing or decreasing by differencing the angular rate of the free end and the fixed end, then the control law applies maximum voltage to the film such that the motion is opposed.

A key issue in technology development for the PVF₂ actuators concerns the method of attachment of the film actuator to the structure it is intended to control. This operation turned out to be much more difficult for components of the full-scale structure than for the small test specimens. A number of adhesives and different bonding techniques were tested before a satisfactory result was achieved. The successful procedure is summarized next.

The PVF₂ film actuators were bonded to each of the four AFAL test structure cantilever arms using Armstrong C-7 adhesive. This adhesive was chosen because of its relatively long pot life and good spreading qualities. The film was aligned before spreading a thin uniform layer of adhesive on the beam. Starting at one end of the beam, the film was pressed into place removing as much trapped air as possible. After the adhesive cured, the excess film was trimmed, and the exposed metalized surface of the film was spray painted with a layer of silver paint for improved conductivity.

The development effort produced several incidental findings including the following: The PVF₂ film (when used as an actuator) should be metalized on only one side if the

structure to which it is to be attached can provide the ground electrode. The surface of the film without metalization can be bonded directly to the surface of the cantilever thereby maximizing the bond strength. Also, metalization on only one side ensures that the PVF₂ actuators will all have the same polarity, i.e., a positive voltage applied to all films will cause all films to either contract or expand. While consistency in polarity is not an essential requirement for the application of the control law, it is a matter of convenience. Finally, it is noted that short circuits can develop between the two metalized faces of the film when it is cut. Generally, these shorts are removed with the first application of voltage.

A PVF₂ damper with four elements (one on each arm) was demonstrated on the full-scale AFAL structure using a Lyapunov-based control algorithm characterized by a nonlinear switching control law. Low-level, bandlimited random noise was input to the air-bearing table torque motor to excite the structure to perform transfer function identification tests. The loss factor achieved for each test was determined from the transfer function measurements. The active damping increased with decreasing vibration amplitude as a consequence of the nonlinear control.

Tests to identify transfer functions were performed using a range of excitation levels to determine the amplitude dependency of the loss factor. For the highest level of excitation, the loss factor for the first anti-symmetric flexible mode was increased from $\eta = 0.0056$ to $\eta = 0.0101$ using a voltage limit of ± 500 volts. The loss factor for the second anti-symmetric flexible mode increased from $\eta = 0.0179$ to $\eta = 0.0236$. With the same voltage limit but for the lowest level of excitation, the loss factor for the first mode was increased from $\eta = 0.0087$ to $\eta = 0.0176$ and the second mode loss factor increased from $\eta = 0.0916$ to $\eta = 0.1245$. The PVF₂ damper should be equally effective for both modes because the deformed shape of the beams for each mode was similar. However, the second anti-symmetric mode was excited the most by the torque motor and hence was damped by higher control forces from the PVF₂ actuators.

For the lowest level of excitation, the PVF₂ actuators added significant damping to the AFAL structure. The active damping added to the second anti-symmetric mode was large (an increase in η of 0.0329) but the corresponding reduction in resonant amplitude was small because of the large passive damping ($\eta = 0.0916$) associated with this mode at low vibration levels. The large passive damping was primarily due to nonlinear forces (friction and/or stiction) in the air-bearing table. The damping added to the first anti-symmetric mode was smaller (an increase in η of 0.0089) but resulted in a larger decrease in vibration amplitude because the baseline damping was very small ($\eta = 0.0087$).

8.2 Conclusions

This study has generally advanced technology development for PVF₂ film actuators and, in particular, their use for active structural vibration damping. The concept of using the piezoelectric characteristics of PVF₂ film to impart a distributed strain field to a structure to effect active control is relatively new. Early research indicated significant promise for this application but development was almost nonexistent. This situation warranted the investigation reported herein. During the investigation, it became apparent that many of the results were generally applicable to low-authority actuators, and not just PVF₂ film actuators.

Specific conclusions from the study are given in below.

8.2.1 Value of Small-scale Tests

The PVF₂ actuators were developed initially using scaled models of an arm of the AFAL structure, progressing to a single full-scale arm of the structure, and finally to the entire structure. The small-scale tests were much faster and less costly to perform than full-scale tests. This approach allowed the researchers to perform many more tests and to gain experience with the PVF₂ film. As a result, many of the basic techniques needed to assemble PVF₂ actuators and to provide high voltage command signals were developed early in the program.

Additional benefits of the small-scale testing included the ease of actuator assembly, and valid scaling of results to the full-scale experiment. Novel damper configurations could easily be fabricated and tested using the small-scale models. Because the smaller test specimens were dynamically scaled from the AFAL structure, the modelling and analysis performed for the small structures could be legitimately scaled to the larger structures. For example, a full-scale version of the PVF₂ constrained layer damper was not implemented because the scaled-model results indicated that the tests would not be worthwhile.

8.2.2 Performance of the PVF₂ Actuators

Tests of several active vibration damper configurations which used PVF₂ film as a distributed-parameter actuator were very positive. A simple PVF₂ actuator with a nonlinear control law provided a factor of forty or more increase in damping for low-level vibrations, increasing as the vibration amplitude decreased. The relative increase in damping from the PVF₂ actuator was very large because the passive damping of the structure was very small ($\eta = 0.002$).

Tests of an alternative damper configuration which used the PVF₂ film as the con-

straining layer of a constrained layer damper were less successful. Experiments showed that most of the energy dissipation was performed by the boundary control effects of the damper (similar to the simple damper configuration). The viscoelastic layer did not contribute significant damping because the PVF₂ film was not stiff enough to act as a good constraining layer. It is conjectured that a constrained layer damper using a much stiffer constraining layer (perhaps steel foil) and with PVF₂ film embedded in the viscoelastic layer may produce a large passive damping which could be actively modulated with the PVF₂ film.

The four segment active damper applied to the full-scale AFAL structure provided damping increases similar to those achieved in the small-scale tests. The PVF₂ actuators were extremely low authority actuators, providing on the order of 8×10^3 lb-ft of bending moment at a control voltage of 500 volts (less than the disturbance friction in the air-bearing table), yet were able to provide a significant increase in damping for low amplitude vibrations. When two modes were controlled simultaneously, the mode with the highest amplitude (as observed by the sensors) received the most active damping due to the nonlinear switching control law.

8.2.3 General Observations Concerning Low Authority Actuators

The experiments demonstrated that low authority actuators (including the PVF₂ film) are not well-suited to remove the energy imparted by large transient disturbances (e.g., slewing or docking maneuvers) in a short time period. The actuators are inherently limited in the amount of energy they can remove during each cycle of vibration. Hence, many cycles may be needed to damp such vibrations.

The steady-state effectiveness of low authority actuators for vibration control depends on the relative amounts of disturbance (or excitation) energy input to the system, the energy dissipated by means of passive damping, and the energy dissipated by active damping. If a large disturbance is present, the energy removed from the structure by a low authority actuator will be negligible. Similarly, if the energy removed by passive damping is large, the added damping from a low authority actuator will again be negligible. The passive damping energy can be large if either the system loss factor is large or the vibration amplitude is large. Therefore, low authority actuators will perform best when used in systems that have low disturbance forces and small loss factors. Possible uses for low authority actuators include damping of the flexible appendages of spacecraft with long-term fine pointing requirements and, more generally, low-level disturbance rejection in very lightly damped structures.

8.3 Recommendations

Additional research is needed to further develop distributed-parameter control design and analysis tools, and to perform validation experiments with distributed-parameter sensors and actuators. The study did not explore applications such as the spatial shaping of an actuator to affect (or ignore) particular modes. Similarly, a sensor could be shaped to sense (or reject) specific modes. One example might be to develop a sensor to measure bending vibrations of a beam in the presence of torsional vibrations.

Finally, further study is needed on the more general applicability of low authority actuators and the choice of appropriate control laws. Low authority actuators tend to be lightweight and to require only small amounts of power, and may prove to be the best tradeoff for long-term low-level disturbance rejection and damping applications. Such actuators may complement higher authority actuators by damping vibrations which are within the deadband or noise floor of the more powerful actuators. Also, nonlinear control laws (such as the Lyapunov-based control laws used in the study) provide more damping than similar linear control laws by using the full actuator authority during the greater part of the damping cycle.

References

- [1] M.G. Kelley, W. Podgorski, and J.E. Hubbard Jr., "Mechanical Design of a Flexible Spacecraft Test Modal for Active Vibration Control," AIAA preprint no. AIAA-84-1048-CP, presented at the 25th Structural dynamics Conference, Palm Springs, CA, 1984.
- [2] M.A. Floyd, "Single-Step Control of Large Space Structures," PhD Thesis, Massachusetts Institute of Technology, April 1984.
- [3] T. Bailey, "Distributed Parameter Active Vibration Control of a Cantilevered Beam Using a Distributed Parameter Actuator," MS/BS Thesis, Massachusetts Institute of Technology, September 1984.
- [4] J.E. Hubbard Jr., C.W. Lowe, "The Active Vibration Control of a Cantilever Beam Using PVF₂ in a Simulated Space Environment", Technical Report CSDL-R-1821, The Charles Stark Draper Laboratory, Inc., Cambridge, MA, December, 1985.
- [5] T.C. Henderson, J.R. and Canavin, "Damping Augmentations for Large Space Structures," Ninth AIAA/ASME Structures and Materials Conference, Paper No. 78-490, Bethesda, MD, April 1976.
- [6] J.S. Gibson, "An Analysis of Optimal Model Regulation: Convergence and Stability," Siam Journal of Control and Optimization, vol. 19, No. 5, pp. 686-707, September, 1981.
- [7] L. Meirovitch and H. Baul, "Nonlinear Control of an Experimental Beam by IMSC," AIAA preprint no. 83-0855.
- [8] M.J. Balas, "Active Control of Flexible Systems," Journal of Optimization Theory and Applications, vol. 25, no. 3; pp. 415-436, 1978.
- [9] S.S. Gates, "Member Dampers for Vibration Suppression of Large Space Structures," MS thesis, Massachusetts Institute of Technology, September 1979
- [10] "Passive and Active Suppression of Vibration Response on Precision Structures, State-of-the-Art Assessment," Technical Analysis, Technical Report CSDL-R-1138, Vol. 2, The Charles Stark Draper Laboratory, Inc., Cambridge MA, 1978

- [11] M.J. Balas, "Finite-Dimensional Controllers for Linear Distributed Parameter Systems: Exponential Stability Using Residual Mode Filters," to be presented at the Fourth IFAC Symposium on Control of Distributed Parameter Systems, Pasadena, CA, June 30 - July 2, 1985.
- [12] R.E. Kalman and J.E. Bartram, "Control System Analysis and Design via the 'Second' Method of Lyapunov," ASME Journal of Basic Engineering, pp. 371-400, 1960.
- [13] P.K.C. Wang, "Stability Analysis of Elastic and Aeroelastic Systems via Lyapunov's Direct Method," Journal of Franklin Institute, Vol. 281, No. 1 pp. 51-72, January 1966.
- [14] M. Slemrod, "An Application of Maximal Dissipative Sets in Control Theory," Journal of Mathematical Analysis and Applications, 46(2), May 1974, pp. 369-387.
- [15] "Kynar Piezo Film," Product information from the Pennwalt Corp., King of Prussia, PA 1983
- [16] D. Ross, E.E. Unger, and E.M. Kerwin Jr., "Damping of Plate Flexural Vibrations by Means of Viscoelastic Laminae," ASME, Structural Damping, pp. 49-87, 1959
- [17] E.M. Kerwin Jr., "Macromechanism of Damping in Composite Structures," ASTM, 1965
- [18] D.J. Mead and S. Markus, "The Forced Vibration of a Three-Layer, Damped Sandwich Beam with Arbitrary Boundary Conditions," Journal of Sound and Vibration 10, pp. 163-175
- [19] E.E. Ungar, "Damping Tapes for Vibration Control," Product Engineering, January 1960, pp.57-62
- [20] Course Notes, "Vibration Damping Short Course," The University of Dayton, Dayton Ohio, June 20, 1983, p. 4.4-11
- [21] S.E. Burke and J.E. Hubbard Jr., "Distributed Actuator Control Design for Flexible Beams", to appear in Automatica, September 1988.
- [22] Nicolet Scientific Corporation, "Instruction Manual for Model 660B Dual-Channel FFT Analyzer, Rev. 2, 550, 1981
- [23] J.M. Plump and J.E. Hubbard Jr., "Modelling of an Active Constrained Layer Damper," to be presented at The 12th International Congress on Acoustics, July 30th 1986, Toronto, Canada.

- [24] J.M. Plump, "An Experimental and Theoretical Analysis of Active Vibration Damping of a Cantilever Beam using a Distributed Actuator," MS Thesis, Massachusetts Institute of Technology, May 1986.
- [25] R.W. Trudell, R.C. Curley and L.C. Rogers, "Passive Damping in Large Precision Space Structures," AIAA paper no. 80-0667, 1980

Appendix A

Modal Model of the AFAL Structure.

This appendix presents the mode shapes and frequencies determined by a NASTRAN-generated model of the modified AFAL structure. The proof-mass actuators (PMAs) at the tip of each arm were locked in their center positions for the PVF₂ actuator tests, so modal information is included only for the PMA-locked configuration. Table A-1 shows the modal frequencies for the first nine structural modes. Modes 2 to 5 were related to the first bending modes of the flexible appendages, while modes 6 to 9 were related to the second bending modes. Figure A-1 illustrates the respective mode shapes determined by NASTRAN.

Table A-1. Vibrational mode frequencies with PMAs locked.

Mode #	Frequency (Hz)	Description
1	0.0	rigid body rotation
2	0.382	1 st bending, primary arms, symmetric
3	0.396	1 st bending, all arms, anti-symmetric, scissors mode
4	0.411	1 st bending, secondary arms, symmetric
5	0.981	1 st bending, all arms, anti-symmetric, twist mode
6	5.827	2 nd bending, primary arms, symmetric
7	5.875	2 nd bending, all arms, anti-symmetric
8	5.984	2 nd bending, secondary arms, symmetric
9	6.110	2 nd bending, all arms, anti-symmetric

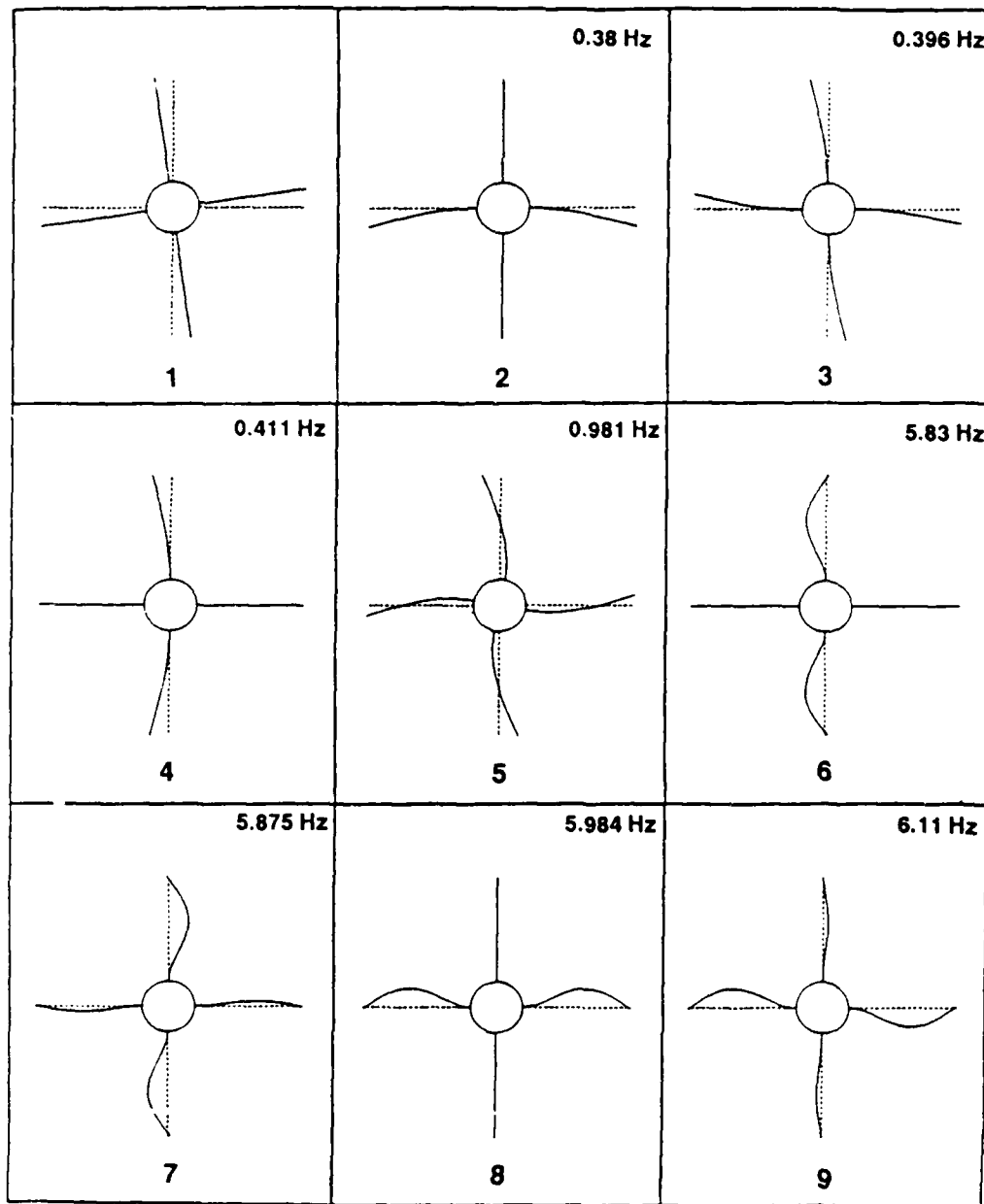


Figure A-1. AFAL structure mode shapes.

Appendix B

MicroVAX II Control Computer Configuration

Figure B-1 shows the configuration of the MicroVAX II control computer and how it was interfaced to the AFAL test structure. The MicroVAX received analog sensor inputs via a Data Translation model 3382 analog-to-digital converter. Analog command outputs were generated using a Data Translation model 3366 digital-to-analog converter. Digital outputs for the thruster commands were provided by a DEC DRV11-J parallel interface board. The DRV11-J also provided digital communication with the Contraves air-bearing table electronics which supplied the hub angle readout. A Codar M-timer timer board was used to generate sample interval and control delay interrupts. The timer board interrupted the MicroVAX through the Q-bus, and interrupted the A/D and D/A converters directly to start conversion sweeps at the appropriate times.

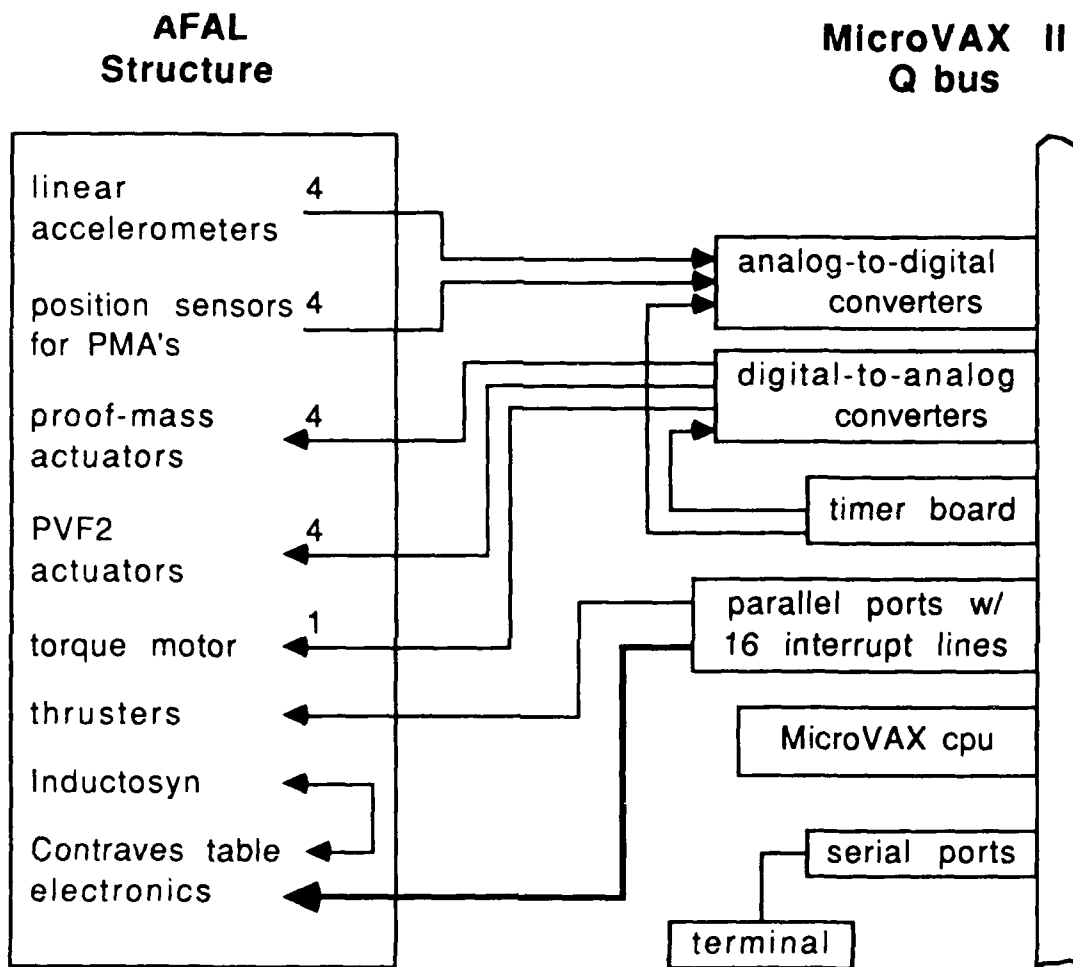


Figure B-1. MicroVAX II computer system configuration.